

# **INFRARED CELESTIAL BACKGROUNDS STUDIES: Volume I. Summary of Project Goals and Accomplishments**

**Russell G. Walker  
Martin Cohen**

**Vanguard Research, Inc.  
5321 Scotts Valley Drive, Suite 204  
Scotts Valley, CA 95066**

**10 September 1998**

**Final Report**

**APPROVED FOR PUBLIC RELEASE; DISTRIBUTION IS UNLIMITED.**

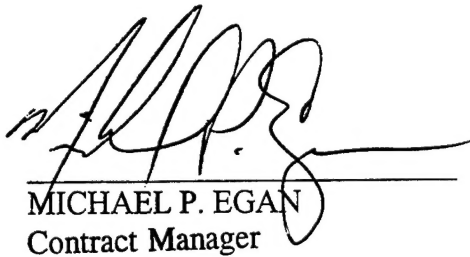


**AIR FORCE RESEARCH LABORATORY  
Space Vehicles Directorate  
29 Randolph Rd  
AIR FORCE MATERIEL COMMAND  
Hanscom AFB, MA 01731-3010**

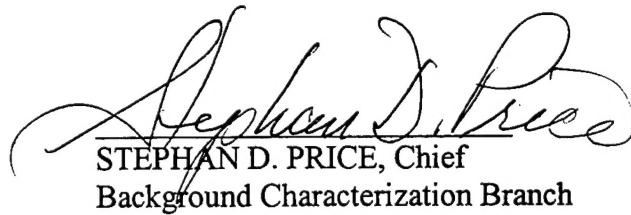
---

19990823 053

" This technical report has been reviewed and is approved for publication."



MICHAEL P. EGAN  
Contract Manager



STEPHAN D. PRICE, Chief  
Background Characterization Branch

This report has been reviewed by the ESC Public Affairs Office (PA) and is releasable to the National Technical Information Service (NTIS).

Qualified requestors may obtain additional copies from the Defense Technical Information Center (DTIC). All others should apply to the National Technical Information Service (NTIS).

If your address has changed, if you wish to be removed from the mailing list, or if the addressee is no longer employed by your organization, please notify PL/IM, 29 Randolph Road, Hanscom AFB, MA. 01731-3010. This will assist us in maintaining a current mailing list.

Do not return copies of this report unless contractual obligations or notices on a specific document require that it be returned.

REPORT DOCUMENTATION PAGE			Form Approved OMB No. 0704-0188	
Public reporting burden for this collection of information is estimated to average 1 hour per response, including the time for reviewing instructions, searching existing data sources, gathering and maintaining the data needed, and completing and reviewing the collection of information. Send comments regarding this burden estimate or any other aspect of this collection of information, including suggestions for reducing this burden, to Washington Headquarters Services, Directorate for Information Operations and Reports, 1215 Jefferson Davis Highway, Suite 1204, Arlington, VA 22202-4302, and to the Office of Management and Budget, Paperwork Reduction Project (0704-0188), Washington, DC 20503.				
1. AGENCY USE ONLY (Leave blank)		2. REPORT DATE September 10, 1998		3. REPORT TYPE AND DATES COVERED Final Report April 16, 1992 – July 15, 1998
4. TITLE AND SUBTITLE Infrared Celestial Backgrounds Studies, ESD Contract No. F19628-92-C-0090 Volume 1. Summary of Project Goals and Accomplishments			5. FUNDING NUMBERS C F19628-92-C-0090 PE 63215C PR 3054 TA 01 WU AS	
6. AUTHORS Russell G. Walker and Martin Cohen				
7. PERFORMING ORGANIZATION NAME(S) AND ADDRESS(ES)  Vanguard Research, Inc. 5321 Scotts Valley Drive, Suite 204 Scotts Valley, CA 95066			8. PERFORMING ORGANIZATION REPORT NUMBER  VRISV-98-01	
9. SPONSORING/MONITORING AGENCY NAME(S) AND ADDRESS(ES)  Electronic Systems Division/PKR Air Force Systems Command, USAF Hanscom AFB, MA 01731-5320			10. SPONSORING/MONITORING AGENCY REPORT NUMBER  AFRL-VS-HA-TR-98-0104 (I)	
11. SUPPLEMENTARY NOTES				
12a. DISTRIBUTION/AVAILABILITY STATEMENT  Approved for public release; distribution unlimited			12b. DISTRIBUTION CODE	
13. ABSTRACT (Maximum 200 words)  The purpose of this program was to extend and improve the present capability to predict celestial phenomenology pertinent to the design and successful operation of space based surveillance systems using the ultraviolet, optical, and infrared spectral regions. We pursued this goal through analysis and application of existing datasets and, in particular, by analysis of new satellite measurements that became available during the course of the project. Our work was concentrated in four major areas: 1) extension of an existing analytical model of the infrared point source sky (SKY), 2) development of a set of absolutely calibrated spectral stellar irradiance standards for the infrared, 3) analysis of new celestial data obtained by satellite, and 4) support of the infrared celestial measurements taken by the Midcourse Space Experiment (MSX) satellite.  Volume 1 summarizes the work performed under the contract, and includes reprints of the major papers published during the contractual period. Volume 2 presents the final release of an all-sky network of 422 stars with absolutely calibrated stellar spectra in the 1.2 to 35 $\mu$ m region. Volume 2 also contains reprints of the complete series of published papers documenting the spectral calibration process and assumptions.				
14. SUBJECT TERMS Infrared calibration, celestial backgrounds, sky model			15. NUMBER OF PAGES 87 – Volume 1	
			16. PRICE CODE	
17. SECURITY CLASSIFICATION OF REPORT  UNCLASSIFIED	18. SECURITY CLASSIFICATION OF THIS PAGE  UNCLASSIFIED	19. SECURITY CLASSIFICATION OF ABSTRACT  UNCLASSIFIED	20. LIMITATION OF ABSTRACT  UL	

## Table of Contents, Volume 1

<b>1. Introduction .....</b>	<b>1</b>
<b>2. Model Extension.....</b>	<b>1</b>
<b>3. Infrared Celestial Calibration Standards.....</b>	<b>3</b>
<b>4. Data Analysis .....</b>	<b>8</b>
<b>5. Support of MSX Activities.....</b>	<b>11</b>
<b>6. Vanguard/Jamieson Scientists and Engineers who Contributed to this Research.....</b>	<b>14</b>
<b>7. Appendix A. Sky Model Extension Papers .....</b>	<b>15</b>
<b>8. Appendix B. Data Analysis Papers.....</b>	<b>48</b>



## 1. Introduction

The purpose of this program was to extend and improve the present capability to predict celestial phenomenology pertinent to the design and successful operation of spaced based surveillance systems using the ultraviolet, optical, and infrared spectral regions. We pursued this goal through analysis and application of existing datasets and, in particular, by analysis of new satellite measurements that became available during the course of the project. Our work was concentrated in four major areas: 1) extension of an existing analytical model of the infrared point source sky (SKY), 2) development of a set of absolutely calibrated spectral stellar irradiance standards for the infrared, 3) analysis of new celestial data obtained by satellite, and 4) support of the infrared celestial measurements taken by the Midcourse Space Experiment (MSX) satellite.

## 2. Model Extension

Our primary objectives in the extension of the point source sky model were: (1) a detailed comparison of the Model's predictions with existing sky maps of surface brightness to sharpen our definition of problems inherent in the current geometry and spectral library; (2) to enhance and validate the performance of the current Sky Model in the near-infrared by making specific elements of its geometry even more realistic; (3) to extend this improved version of the Model into the visible and UV domain by modifying the geometry and perhaps the source content of the model sky, extrapolating the spectral range of the spectral library embedded in the code, and extensively comparing our new Model with existing UV-visible point source databases; and (4) to improve the model's spatial capabilities in regions of high source density and spectral capabilities in currently little-observed wavelength regions by incorporation of the results of ISO and MSX measurements. Some highlights concerning the model extension are:

A. Broadening the Wavelength Range over which the Model can Handle Arbitrary Filters -  
This was pursued through the vehicle of Kurucz grids of emergent spectra from model atmosphere calculations. It proved possible to represent many of the normal stellar types in this fashion. However, these models poorly mimic cool (K and M) giants because of shortcomings of the TiO and CN line lists used in the optical, use of somewhat dated line strengths for CO in the near-infrared, and the absence of SiO and water vapor in the band systems of the infrared. The intent was then to depend, as for the assembly of the SKY Version 3 synthetic spectral library, on stitching together observed spectra that cover the regions in which the absent, or poorly modeled, molecular lines occur. Indeed, the calibration effort under this contract sufficed to provide observed 1.2-35  $\mu\text{m}$  spectra for K0 to M2.5 giants. But later type giants (SKY still needs M3,4,5,6,7 giants) have never come within the purview of our calibration work and their complete observed spectra are still lacking. Similar problems have arisen with cool (K and M) dwarfs. State-of-the-art model atmospheres are still cutting edge science as theoreticians work to incorporate the more than 300 million lines of water recently compiled for models in the infrared and to represent the microphysics (the equation of state) realistically. Consequently, reliance was again placed on observed spectra of K and M dwarfs, which are slated to appear soon (a new

synthetic library by Pickles is awaited) in 1998, but have not yet been forthcoming. Thus "dual-wavelength" capability is still not available outside the range of SKY3 (2.0-35  $\mu$ m).

**B. Improving the Geometry of the Molecular Ring** - This was addressed partially under this contract during a visit to DENIS Headquarters at Observatoire de Paris-Meudon in summer of 1996. At this time, the original circular molecular ring of all previous versions of SKY was replaced by an elliptical ring. DENIS star counts sufficed to indicate the general correctness of the dimensions and orientation of an ellipse originally posited by Simonson III and Mader in 1973. While DENIS data have been useful, different data are essential to sculpt the details of the dense ansae of the new ring because it must clearly be non-uniformly dense to mimic the  $l^{\text{II}} = 27^{\circ}$  (tangent to the ring) "face of the Bar" direction. Therefore, some effort went into analysis of TMGS K-counts at longitudes from  $7^{\circ}$  to  $31^{\circ}$ . While this yielded some information, it has so far proved impossible to choose a single set of parameters that characterizes the non-uniformity adequately and will match all these directions simultaneously to  $K < 10$ . Recent new NICMOS3 array images in JHK (also from the Tenerife group) have illustrated and outlined the extreme variations in extinction that typify the tangential direction to the ring in the first quadrant. It was then clear that SPIRIT-III counts in Band A would be essential to model the ring because of the substantially reduced effects of extinction in the mid-infrared.

**C. Enhancing the Fidelity of Predictions at Deeper Magnitude Levels** - This goal, also not yet fully attained, was to seek and model ever deeper observed counts. These have been forthcoming in the past year through two collaborations resulting from a PhD thesis in Milan, Italy (Paolo Saracco) and another from NOAO (Pat Hall). It transpires that one needs to adjust the space densities of some elements in SKY from counts at the faintest magnitudes. By itself, this is an ill-posed problem. But the Milan group has also provided B-V and B-K histograms from a series of deep images at high Galactic latitudes. From these it is clear that the problem lies with the M-dwarfs and, in keeping with the HST deep counts, could be resolved by significantly reducing the space densities of M-dwarfs. The fundamental set of absolute magnitudes (MV) in SKY5 has also been reworked and, from this, new sets for MB and MK developed, maintaining consistency with integrations over whatever categories are represented in the as yet incomplete new library of spectra.

During the period of the contract, SKY Versions 1, 3, and 4 were published and/or developed. The latest version currently in use for which full documentation of the changes has appeared in the literature is Version 4.2. Version 5 of SKY remains in the developmental phase. In short, there is still much to do. But fairly widespread testing of SKY5 at a variety of latitudes and wavelengths suggests that its fidelity exceeds that of SKY4. The remaining problems are still; to reevaluate absolute magnitudes (MV) in light of newly released Hipparcos data; to revisit the space densities; to finalize the geometry of the ring; and to complete the spectral library.

The results of our infrared sky model work have been published in the peer-reviewed scientific literature. These papers are summarized in the following paragraphs and reprinted in Volume 2, Appendix G.

*A Model of the 2-35  $\mu$ m Point Source Infrared Sky* (Cohen, M., 1993, *Astronomical Journal*, Vol. 105, Number 5, pages 1860-1879). The original sky model of Wainscoat *et al.* (*Astrophys. J. Supp.*, 83, 111, 1992) was extended to make source count predictions for any filter lying wholly within the

range 2.0 to 35.0  $\mu\text{m}$ . This extension was supported by the development of a library of complete 2-35  $\mu\text{m}$  low resolution spectra for 87 categories of Galactic objects and four types of extragalactic sources that are imbedded in the model. This library is based upon the "spectral template" technique whereby existing observed spectral fragments are combined into complete spectra. The previous model comprised several broadband filters (J, H, K, [2.4], IRAS 12 and 25  $\mu\text{m}$ ) and had the capacity to operate continuously only from 7.67-22.74  $\mu\text{m}$ . This version performs identically to the old at 2.2, 12, and 25  $\mu\text{m}$ . In addition it accommodates all filters that lie within the 2-35  $\mu\text{m}$  range, with consistency between tables of broadband absolute magnitudes and those derived by integration of the actual filter/system response over the real spectra. The new model has also been modified to yield estimates of the surface brightness due to unresolved point sources within a specified area, as a function of threshold sensitivity.

*Powerful Model for the Point Source Sky: Far-Ultraviolet and Enhanced Midinfrared Performance* (Cohen, M., 1994, *Astronomical Journal*, Vol. 107, Number 2, pages 582-593). The original sky model of Wainscoat *et al.* (*Astrophys. J. Supp.*, 83, 111, 1992) was further developed. The already detailed and realistic representation of the Galaxy, with disk, spiral arms, local spur, molecular ring, bulge, and spheroid components, was improved, guided by CO surveys of local molecular clouds, and by inclusion of a component to represent Gould's Belt. This newest model was very well validated by IRAS source counts. The wavelength range was extended into the far-ultraviolet, and predicted star counts were compared to those from the Apollo 16 "S201" experiment at 1400Å and the TD1 satellite survey at 1565Å. The improvement in the geometrical representation of the local spurs and sculpting due to molecular clouds greatly enhanced the fidelity of the model's simulations of the midinfrared sky. The far-ultraviolet performance is very good at high and intermediate latitudes. The performance is also satisfactory in the galactic plane, although the method of treating extinction is still somewhat inadequate.

### 3. Infrared Celestial Calibration Standards

Our objective was to produce a fundamental reference catalog of celestial sources with their absolute spectral irradiances that could be used directly for most infrared calibration purposes. To accomplish this we continued to support the work of the Stellar Atlas panel conceived at AFGL. We studied and resolved the issue of the absolute zero magnitude flux calibration in the infrared; (3) incorporated new data relevant to calibration as they became available from the KAO HIFOGS and UKIRT CGS3 spectrometers, and precision ground-based infrared photometry made with well characterized photometric systems. We developed and applied the concept of stellar "spectral templates" to estimate the spectral flux of stars that have incomplete data; and (5) prepared and issued a series of preliminary versions of the spectral irradiance catalog, each version being more complete in spectral coverage, photometric precision, and number of calibrated stars.

A) Spectral Irradiance Calibration Results - The results of our infrared spectral irradiance calibration have been published in a suite of papers in the peer-reviewed scientific literature. These papers are summarized in the following paragraphs and reprinted in Volume 2, Appendix G.

*Spectral Irradiance Calibration in the Infrared. I. Ground-based and IRAS Broadband Calibrations* (Cohen, M., Walker, R.G., Barlow, M.J., and Deacon, J.R., 1992, *Astronomical Journal*, Vol. 104, Number 4, Pages 1650-1675). We describe an approach to absolute stellar calibration of broad and narrow band infrared filters based upon new models of Vega and Sirius due to Kurucz (1991a) and calculated by him, for the first time, with realistic stellar metallicities and a finely-gridded wavelength scale in the infrared. After normalizing the Vega model so that it matches Hayes' (1985) weighted average of six monochromatic 5556Å measurements we integrate the model through a variety of infrared filters using determinations of filter transmission profiles obtained at their actual operating temperature, and detailed model calculations for terrestrial atmospheric transmission. This provides in-band fluxes for Vega, which we define to be zero magnitude at all wavelengths shortward of 20  $\mu\text{m}$ . We use existing infrared photometry differentially to establish an absolute scale for the new Sirius model. This yields an angular diameter within  $1\sigma$  of the mean determined interferometrically by Hanbury Brown, Davis, and Allen (1974). For practical purposes, Sirius provides the absolute calibration beyond the 20  $\mu\text{m}$  region because of Vega's dust shell. Isophotal wavelengths and monochromatic flux densities for both Vega and Sirius are tabulated. We attempt a comparison of our calibration figures for the IRAS wavebands with the process used to generate the original IRAS absolute calibration. A complete duplication of that process is not currently possible. Preliminary indications are that IRAS is too high by 2, 6, 3, and 12% at 12, 25, 60, and 100  $\mu\text{m}$ , respectively.

*Spectral Irradiance Calibration in the Infrared. II.  $\alpha$  Tau and the Recalibration of the IRAS Low Resolution Spectrometer* (Cohen, M., Walker, R.G., Witteborn, F.C., 1992, *Astronomical Journal*, Vol. 104, Number 5, Pages 2030-2044). We describe a general technique for assembling continuous calibrated infrared spectra over a wide wavelength range. To demonstrate the method we construct an absolutely calibrated 1-35  $\mu\text{m}$  spectrum of  $\alpha$  Tau and independently validate the method using new and carefully designed observations. First we investigate the absolute calibration of the IRAS Low Resolution Spectrometer (LRS) database by comparing this observed spectrum of  $\alpha$  Tau with that assumed in the original LRS calibration scheme. Second, an analysis of asteroidal LRS spectra results in an independent assessment of the calibration problems with the LRS and provides a natural complement to the effort based on  $\alpha$  Tau. Stellar studies define the short wavelength problems well; the cool asteroids characterize the long wavelengths. Third, we make a direct comparison of LRS stellar spectra with independently calibrated long-wavelength ( $\sim 20$   $\mu\text{m}$ ) airborne and ground-based spectra. These three approaches are complementary and have been combined. Neglect of the SiO fundamental band in  $\alpha$  Tau has led to the presence of a specious "emission" feature in all LRS spectra near 8.5  $\mu\text{m}$ , and to an incorrect spectral slope between 8 and  $\sim 12$   $\mu\text{m}$ . We explain the differences between this new LRS recalibration and that due to Volk & Cohen (1989) and discuss why the present set of "correction factors" is more accurate. Recognition of the influence of the SiO fundamental on both the LRS calibration and on the continua of cool normal giant stars also leads to an understanding of the apparent plethora of classes into which these normal stars fall when assigned by the AUTOCLASS (Cheeseman *et al.* 1989) Artificial Intelligence scheme applied to the IRAS LRS Atlas.

*Spectral Irradiance Calibration in the Infrared. III. The Influence of CO and SiO* (Cohen, M., Witteborn, F.C., Carbon, D.F., Augason, G., Wooden, D., Bregman, J., and Goorvitch, D., 1992, *Astronomical Journal*, Vol. 104, Number 5, Pages 2045-2052). We describe first efforts to establish a network of calibrated infrared spectra of "standard stars" suitable for calibration of at least low-



resolution infrared spectrometers using ground-based, airborne, and satellite-borne broadband sensors. The focus of this paper is on the crucial 5-8  $\mu\text{m}$  region, inaccessible from the ground, in K and M giants. In this region the fundamental bands of CO and SiO cause substantial departures from featureless pseudo-continua. These departures are, of course, well-known to stellar atmosphere theorists. However, they are still ignored by many astronomical infrared photometrists and spectroscopists who assume that these bright stars can be represented by blackbodies at their effective temperatures. The purpose of this short paper is to draw the attention of infrared observers in the field to the invalidity of the blackbody assumption in the thermal infrared regime. We achieve this end by observationally demonstrating the importance of these molecular features in cool giant stars in the airborne infrared regime, and illustrating their influence on spectra that are calibrated using blackbody assumptions. To help confirm our identifications of the principal molecular features, we present a synthetic spectrum computed using a model atmosphere with the approximate parameters of  $\alpha$  Tau. This theoretical synthetic spectrum, which contains line opacity only from CO and SiO, reproduces the observed spectrum of  $\alpha$  Tau to within a few percent.

*Spectral Irradiance Calibration in the Infrared. IV. 1.2-35  $\mu\text{m}$  Spectra of Six Standard Stars* (Cohen, M., Witteborn, F.C., Walker, R.G., Bregman, J.D., and Wooden, D.H., 1995, *Astronomical Journal*, Vol. 110, Number 1, Pages 275-289). We present 5 new absolutely calibrated continuous stellar spectra from 1.2 to 35  $\mu\text{m}$ , constructed as far as possible from actual observed spectral fragments taken from the ground, the Kuiper Airborne Observatory (KAO), and the IRAS Low Resolution Spectrometer (LRS). These stars --  $\beta$  Peg,  $\alpha$  Boo,  $\beta$  And,  $\beta$  Gem, and  $\alpha$  Hya -- augment our already created complete absolutely calibrated spectrum for  $\alpha$  Tau. All these spectra have a common calibration pedigree. The wavelength coverage is ideal for calibration of many existing and proposed ground-based, airborne, and satellite sensors. These spectra were the first of our calibration spectra to appear on the AAS CD-ROM series. These six spectra, as well as, the calibrated Kurucz model spectra for Vega and Sirius can be found on the Fifth Volume, AAS CD-ROM Series.

*Spectral Irradiance Calibration in the Infrared. V. The Role of UKIRT and the CGS3 Spectrometer* (Cohen, M. and Davies, J.K., 1995, *Monthly Notices of the Royal Astronomical Society*, Vol. 276, Pages 715-722). We describe, illustrate, and quantify the performance achieved by the combination of CGS3 and UKIRT, with emphasis on the role already played by CGS3 in the field of spectrally continuous, absolute infrared radiance calibration. The focus of this paper is on the reliability and reproducibility of the spectral shapes obtained by CGS3. We offer an electronically available data base of calibration spectra taken with the UKIRT and CGS3 of a variety of infrared-bright cool K and M giants. These highlight the influence of the SiO fundamental absorption on the stellar spectra as effective temperature is varied. The calibration archive has an absolute pedigree traceable directly to Cohen, et al. as presented in the above summarized papers.

*Spectral Irradiance Calibration in the Infrared. VI. 3-35  $\mu\text{m}$  Spectra of Three southern Standards* (Cohen, M., Witteborn, F.C., Bregman, J.D., Wooden, D., Salama, A., and Metcalfe, L., 1996, *Astronomical Journal*, Vol. 112, Number 1, Pages 241-251). We present three new absolutely calibrated continuous stellar spectra from 3 to 35  $\mu\text{m}$ , constructed as far as possible from actual observed spectral fragments taken from the Kuiper Airborne Observatory (KAO), and the IRAS Low Resolution Spectrometer (LRS). These stars --  $\alpha^1$  Cen,  $\alpha$  TrA, and  $\epsilon$  Car -- augment our previous archive of complete absolutely calibrated spectra for northern K and M giants. All these spectra have a

common calibration pedigree. The wavelength coverage is ideal for calibration of many existing and proposed ground-based, airborne, and satellite sensors. KAO and IRAS data in the 15-30  $\mu\text{m}$  range suggest that the spectra of cool giants are close to Rayleigh-Jeans slopes. Our observations of  $\alpha^1$  Cen, absolutely calibrated via our adopted Sirius model, indicate an angular diameter in very good agreement with values in the literature, demonstrating "closure" of the set of spectra within our absolute framework. We compare our observed  $\alpha^1$  Cen spectrum with a published grid of theoretical models from Kurucz, and adopt a plausible theoretical shape, that fits our spectrum, as a secondary reference spectrum in the southern sky. We recommend use of this star when a southern standard brighter than Sirius is needed.

*Spectral Irradiance Calibration in the Infrared. VII. New Composite Spectra, Comparison with Model atmospheres, and Far-Infrared Extrapolations* (Cohen, M., Witteborn, F.C., Carbon, D.F., Davies, J.K., Wooden, D.H., Bregman, J.D., L., 1996, *Astronomical Journal*, Vol. 112, Number 5, Pages 2274-2285). We present five new absolutely calibrated continuous stellar spectra constructed as far as possible from spectral fragments observed from the ground, the Kuiper Airborne Observatory (KAO), and the IRAS Low Resolution Spectrometer. These stars --  $\alpha$  Boo,  $\gamma$  Dra,  $\alpha$  Cet,  $\gamma$  Cru, and  $\mu$  UMa -- augment our six, published, absolutely calibrated spectra of K and early M giants. All spectra have a common calibration pedigree. A revised composite for  $\alpha$  Boo has been constructed from higher quality spectral fragments than our previously published one. The spectrum of  $\gamma$  Dra was created in direct response to the needs of instruments aboard the Infrared Space Observatory (ISO); this star's location near the north ecliptic pole renders it highly visible throughout the mission. We compare all our low-resolution composite spectra with Kurucz model atmospheres and find good agreement in shape, with the obvious exception of the SiO fundamental, still lacking in current grids of model atmospheres. The CO fundamental seems slightly too deep in these models, but this could reflect our use of generic models with solar metal abundances rather than models specific to the metallicities of the individual stars. Angular diameters derived from these spectra and models are in excellent agreement with the best observed diameters. The ratio of our adopted Sirius and Vega models is vindicated by spectral observations. We compare IRAS fluxes predicted from our cool stellar spectra with those observed and conclude that, at 12 and 25  $\mu\text{m}$ , flux densities measured by IRAS should be revised downwards by about 4.1 % and 5.7 %, respectively, for consistency with our absolute calibration. We have provided extrapolated continuum versions of these spectra to 300  $\mu\text{m}$ , in direct support of ISO (PHT and LWS instruments). These spectra are consistent with IRAS flux densities at 60 and 100  $\mu\text{m}$ .

*Spectral Irradiance Calibration in the Infrared. VIII. 5-14  $\mu\text{m}$  Spectroscopy of the Asteroids Ceres, Vesta and Pallas* (Cohen, M., Witteborn, F.C., Roush, T., Bregman, J.D., and Wooden, D.H., 1998, in press, *Astronomical Journal*).<sup>1</sup> We describe our efforts to seek "closure" in our infrared calibration scheme by comparing spectra of asteroids, absolutely calibrated through reference stars, with "Standard Thermal Models" and "Thermophysical Models" for these bodies. Our use of continuous 5-14  $\mu\text{m}$  airborne spectra provides complete sampling of the rise to, and peak of the thermal infrared spectral energy distribution and constrains these models. Such models currently

---

<sup>1</sup> This work was entirely supported by NASA's Airborne Astronomy Program and a subcontract from the University of Florida. It is reported here for the sake of completeness to the set of spectral calibration references, and since it was motivated by the calibration work undertaken for the contract.

support the absolute calibration of ISO-PHOT at far-infrared wavelengths (as far as 300  $\mu\text{m}$ ), and contribute to that of the Mid-Infrared Spectrometer on the "Infrared Telescope in Space" in the 6-12  $\mu\text{m}$  region. The best match to our observed spectra of Ceres and Vesta is a standard thermal model using a beaming factor of unity. We also report the presence of three emissivity features in Ceres which may complicate the traditional model extrapolation to the far-infrared from contemporaneous ground-based N-band photometry. While identification of specific minerals that cause these features is not made, we discuss families of minerals that may be responsible.

*Spectral Irradiance Calibration in the Infrared. IX. Calibrated Stellar Spectra using DIRBE Radiometry (Cohen, M., submitted to the Astronomical Journal).*<sup>2</sup> The absolute calibration of the COBE/DIRBE data in the range 1-25  $\mu\text{m}$  is examined through the in-band fluxes of DIRBE's own set of point source calibration objects. Using the values of DIRBE fluxes expected for Sirius and 10 of our published set of absolutely calibrated K and M giants that are in common with DIRBE's own calibration network, we find consistency with the project's formal basis, namely our published calibrated spectrum of Sirius. This consistency means that one can use the DIRBE radiometry to construct absolutely calibrated "stellar templates" on the assumption that the intrinsic spectral shape of a star of a given spectral class matches the intrinsic spectral shape for the star of the same spectral class among the set of K and M giants, whose spectral shape has been previously defined. This technique is validated using a set of early M giants with well-characterized ground-based photometry, and confirmed with IRAS Low Resolution Spectra.

*Spectral Irradiance Calibration in the Infrared. X. A Radiometric All-Sky Network of Absolutely Calibrated Stellar Spectra (Cohen, M., Walker, R.G., Carter, B., Hammersley, P., Kidger, M., and Noguchi, K., submitted to the Astronomical Journal).* We start from our six absolutely calibrated continuous stellar spectra from 1.2 to 35  $\mu\text{m}$  for K0, K1.5, K3, K5, and M0 giants. These were constructed as far as possible from actual observed spectral fragments taken from the ground, the Kuiper Airborne Observatory (KAO), and the IRAS Low Resolution Spectrometer (LRS), and all have a common calibration pedigree. From these we spawn 422 calibrated "spectral templates" for stars with spectral types in the ranges G9.5-K3.5III and K4.5-M0.5III. We normalize each template by photometry for the individual stars using published, and/or newly secured, near- and mid-infrared photometry obtained through fully characterized, absolutely calibrated, combinations of filter passband, detector radiance response, and mean terrestrial atmospheric transmission. These templates initiate our ongoing effort to provide an all-sky network of absolutely calibrated, spectrally continuous, stellar standards for general infrared usage, all with a common traceable calibration heritage. The wavelength coverage is ideal for calibration of many existing and proposed ground-based, airborne, and satellite sensors. We analyze the statistics of probable uncertainties, in the normalization of these templates to actual photometry, that quantify the confidence with which we can assert that these templates truly represent the individual stars.

---

<sup>2</sup> This work was entirely supported by the NASA ADP Program. It is reported here for the sake of completeness to the set of spectral calibration references, and since it was motivated by the calibration work undertaken for the contract.

The details of Paper X are given in Volume 2 of this Final Report complete with plots of the absolute calibrated spectra for all 422 stars. A preliminary release of the catalog was made on October 5, 1994, when 86 calibrated spectral templates were delivered to AFRL. The full catalog of 422 spectral templates were delivered to AFRL on December 1, 1997, and include revisions to some of the previously released 86 templates. It is available in the form of ASCII files by request to Dr. Michael P. Egan at AFRL/VSBC (egan@pldac.plh.af.mil).

**B) Bright IR Spectral Catalog** - Near the end of the program an effort was initiated to produce a spectral catalog of the brightest infrared point sources. This catalog would contain calibrated spectra (with associated uncertainties) of those sources brighter than zero magnitude at K, [12  $\mu$ m], and [25  $\mu$ m]. The sources of data were the IRAS PSC2 and the Cal Tech Two Micron Sky Survey with its unpublished Southern Extension. These catalogs were searched and 168 stars were found with  $K < 0$ ; 1636 sources for  $[12] < 0$ ; and 6885 sources for  $[25] < 0$ .

It is well known that the brightest infrared sources are not normal stars - their brightness being due to their infrared excess. Many of these objects are in stages of evolution that are characterized by variability of the emitted flux. Thus it is difficult to assemble spectral fragments and photometry that may have been taken at different phases of the light curve. In order to grasp the magnitude of the variability problem we have examined the classification of the extracted 1636 12 $\mu$ m sources. We find that: 535 are listed in the General Catalog of Variable Stars; 160 are listed in the Catalog of Suspected Variables; 105 are carbon stars; and 28 are S stars. IRAS examined the observed fluxes at 12 and 25  $\mu$ m for multiple detections of the same object and found that 920 (56% of 1636) sources had a probability of variability,  $P_v = 99\%$ ; 992 (61%) had  $P_v = 90\%$ ; and 1114 (68%) had  $P_v = 50\%$ . It is clear that handling source variability will be a major task in completing this project.

At the conclusion of the program an input source list had been defined, and we were in the process of searching for and extracting IRAS Low Resolution Spectra for these sources.

#### 4. Data Analysis

At the outset of the program it was assumed that the vast bulk of the data to be analyzed would be that obtained from the MSX. Thus our initial objectives were fourfold: (1) to provide results necessary to extend and refine the sky model through an iterative procedure of testing model predictions against observations, revising the model parameters, and so forth; (2) to provide as many real spectra from the SPIRIT III interferometer as possible for inclusion in the stellar calibration atlas, and the sky model's library, thus improving the model's spectral realism; (3) to extend the database of thermal and physical properties of small bodies (eg: asteroids, comets, natural satellites) in the solar system and to refine thermal emission models pertinent to these bodies; and (4) to determine the magnitude and distribution of zodiacal emission components of high spatial frequency (ex: zodiacal bands, comet debris trails).

For a variety of reasons these goals were only partially achieved. Launch delays slipped the entire data analysis schedule several years. The difficulties of correcting the data for instrumental effects (dark offset, focal plane temperature variations, flat field, etc.) placed high demands on data processing facilities and required several periods of re-processing. Reoccurring failures of the SPIRIT III interferometer resulted in only a few celestial spectra being obtained, and these of



only very bright extended sources (Orion, and the Galactic Center). The bulk of the program resources were expended in acquiring and processing the data; little was left for data analysis. The following is a summary of the status of our MSX data analysis at this time as related to our original set of goals:

A) Sky Model Extension - None of the MSX source counts has had more than a cursory comparison with the predictions of SKY, and these were done in the sense of a quality check on the source extraction processing. Extensions of SKY, as presented in Section 2, and tests of SKY, as presented below in this Section, were based on data sets from sources other than MSX. Analyses of these sets have further validated SKY and produced valuable science. Reprints are included in Volume 1, Appendix B.

a) *The Galactic Far-Ultraviolet Sky as seen by Faust: Modeling and Observations* (Cohen, M., Sasseen, T.P., and Bowyer, S., 1994, *Astrophysical Journal*, Vol. 427, pages 848-856). We have tested the model of the Galactic point source sky extended to the far-ultraviolet by Cohen(1994) against the set of Galactic far-ultraviolet point sources seen by the FAUST experiment. There is excellent agreement between the predicted ( $\log N$ ,  $\log S$ ) and the observed source counts for the range of Galactic directions observed by FAUST.

b) *The Displacement of the Sun from the Galactic Plane Using IRAS and Faust Source Counts* (Cohen, M., 1995, *Astrophysical Journal*, Vol. 444, pages 874-878). SKY is applied to deducing the displacement ( $z_{\odot}$ ) of the Sun from the galactic plane. The IRAS ensemble is best matched by  $z_{\odot} = 15.5 \pm 0.7$  pc north of the plane, a value also favored by shallow K counts. The FAUST data favor a value near  $z_{\odot} = 14.0$  pc. The best fit to all the data suggests a value of  $z_{\odot} = 15.0 \pm 0.5$  pc. There is also a brief discussion of the ratio of halo:disk populations in SKY, with the suggestion that a value around 0.4 times that of SKY version 1 would result in improved predicted counts from the model.

c) *Interpreting Surveys with Models* (Cohen, M., 1997, in *The Impact of Large-Scale Near-IR Sky Surveys*, pages 67-70, Kluwer Academic Publishers). The interpretation of near-infrared surveys using SKY is discussed with the focus on those aspects of the counts from which one can elicit information about Galactic structure.

B) Stellar Calibration Atlas Spectra - No spectral measurements were made by MSX of stars suitable for calibration standards. Well characterized measurements from ground based and airborne observatories, that became available during the contract period, were analyzed and incorporated into composites for the Infrared Celestial Calibration Standards (see Section 3). The results of MSX photometry done in the CB06 "triads" are now the subject of a "global" recalibration of SPIRIT III by the DCATT team. Therefore those data have not yet been incorporated into the photometry pool for normalization of spectral templates.

C) Solar System Small Bodies Database - A great potential exists for enlarging our knowledge data base of small solar system bodies, due to the success with which MSX observed solar system objects, however, to date little or no significant analysis has been accomplished.

The celestial backgrounds experiment, CB09, observed 8 comets and 4 asteroids that are candidates for "burned-out" comet nuclei. Considerable effort was expended developing special image construction and coaddition programs necessary to compensate for the motion of both the solar system objects and the MSX spacecraft during the DCEs. The large field scanned (typically

1° wide by 3.5° long) combined with the good sensitivity of the detectors and a factor of nearly four coadd advantage from the 15 scans allows us to map the dust to great distances from the comet. Some preliminary results for comets Hyakutake, Hale-Bopp, Tabur, and Kopff were presented at a poster session at the 1997 meeting of the Division for Planetary Sciences (DPS) of the American Astronomical Society. A copy of that poster paper, *MSX Observations of Cometary Dust*, is included in Appendix B of this volume.

Comet Temple-Tuttle was observed on a special request from NASA to see if we could set a limit on the dust in the comet's orbit. Their concern was to better predict the magnitude of the up-coming Leonid Meteor showers. We observed Temple-Tuttle on February 2, 1996. The comet was 4.3 AU from the Sun and 4.7 AU from Earth. The expected dust temperature would be about 148 K. We could not detect the comet or its dust trail in any SPIRIT III band, either in a single scan or in the coadds of up to 15 scans. The low grain temperature precluded a meaningful upper limit to the dust production or trail mass.

A computer program, ASTCAT, was written to produce mini-catalogs of solar system objects that were scanned during a celestial backgrounds DCE. Three hundred and twenty two mini-catalogs were produced to cover all of the DCEs. We installed these files on the PL DAF in May, 1998. The catalogs contain 3197 predicted sightings of 1285 known asteroids, and 89 sightings of 35 comets and planets. A preliminary test of the catalogs was made by Egan (private communication) for a region near the galactic plane. He found good positional associations with 27 out of 88 predicted. The faintest detection was that of an asteroid with a flux of  $2.9 \times 10^{-18}$  watts/cm<sup>2</sup> in the SPIRIT III Band A. Based on Egan's sample, we estimate that SPIRIT III will produce at least 1800 valid sightings of 770 asteroids. Of these, at least 130 asteroids will not have been observed by IRAS.

D) Zodiacal Emission Components - The SPIRIT III radiometer, aboard the MSX satellite, has provided us with new and unique observations of the Zodiacal cloud in the four infrared wavebands between 6.8 and 25.1 microns. Zodiacal measurements were obtained on a total of 69 observations over the 10 month cryogen phase of the mission. The observations consisted of long scans ( $\geq 135^\circ$ ) at (nearly) constant ecliptic longitude; about two-thirds of these scans include the north ecliptic pole. In aggregate, the scans cover solar elongations between  $25^\circ$  and  $170^\circ$ , far larger than the IRAS, plus COBE limits of  $64^\circ$  to  $124^\circ$ . Thus, the uniqueness of this data set enables us, for the first time, to systematically probe the dust distribution in the zodiacal cloud, as well as the variation in the structure of the cloud, from the sun to the asteroid belt using data from a single experiment.

However, as with the small bodies analysis, we have done little analysis of the zodiacal emission data. No work has been accomplished on the fine scale structure of the zodiacal cloud, i.e. the zodiacal dust bands. Most of our analysis efforts have been expended on unraveling the component of non-rejected Earth radiance (NRER) that contaminates the near-Sun zodiacal data. Final analysis awaits a definitive solution for the NRER obtained from DCATT characterization experiments. We have performed a preliminary analysis of a single CB01 scan that passes  $26^\circ$  from the Sun. These results were presented as a poster paper, *MSX Observations of the Zodiacal Cloud*, at the 1997 DPS meeting, and are reprinted here in Appendix B of this volume.

The CB09 comet observations that have been fully processed were searched for debris trails. No trails were found for comets Hyakutake, Hale-Bopp, Tabur, and Temple-Tuttle. P/Kopff showed a debris trail as expected from IRAS observations. Comets Spacewatch, IRAS, and

Wirtanen have yet to be processed. None of the asteroids (old comet nuclei) have been processed. Support is being sought from NASA's Planetary Geology program to analyze the comet and debris trail data.

## 5. Support of MSX Activities

A critical element in the analysis of observations made from orbiting spacecraft is an in-depth knowledge of the spacecraft system, and, in particular, the infrared sensor, its design, performance, and ground calibrations. As Co-Investigators on the celestial backgrounds science team of the MSX program our responsibilities included (1) review of MSX preflight tests and on-orbit checkout tests, and assessment of the impact of the test results on the experiments planned; (2) experiment planning and revision of plans supported by limited studies to optimize the scientific data return; (3) certification of Level 3 and higher data products and development of supporting software; (4) preparation of experiment analysis reports; and (5) participation in MSX Co-I and PI Team meetings (as required) and related team efforts. Thus we served as a conduit between the Science Team, and the observations; and afforded timely and intimate access to all the relevant MSX data. The objective of this task was to enable these functions with regard to MSX, and, because we shared common interests with the Europeans involved in the ISO mission, our further objective was to maintain close ties with Europe in general and with ISO scientists in particular. The advantages of a coordinated international approach lay in the avoidance of duplicated efforts and in the sharing of common spectral databases as new ground-based and airborne observations were obtained in support of these and future missions.

We participated in the MSX Co-I and PI Team meetings as required, and maintained a close liaison with ISO, particularly in regards to developing a mutual calibration basis. However, the bulk of our technical effort was expended on the following sub-tasks:

### A). Celestial Backgrounds Experiment Plans

We assumed the lead roles, authoring and revising as needed each of the experiment plans listed below.

a) CB-02 *Celestial High Density Regions* - This experiment was designed to spatially resolve sources and clutter in regions which have a high density of sources. At 40 times the spatial resolution of IRAS, this experiment was designed to enable SPIRIT III to complete sky coverage in areas in which IRAS was confused. Nominally, the area within  $\pm 5^\circ$  of the Galactic plane over the entire  $360^\circ$  in longitude was to be redundantly scanned in all bands except Band B.

b) CB-03 *Deep Galactic Plane Maps* - This experiment was designed to create a data base at high sensitivity in those regions of the sky where discrepancies existed between the current CBSD point source sky models and actual source counts. The high spatial resolution of SPIRIT III observations was used to resolve whether the discrepancies were due to inadequacies of the model or to incompleteness of the present data base.

c) CB-06 *Celestial Radiometric Standards* - The goal of this experiment was to create an extensive fundamental reference catalog of sources to calibrate the absolute responsivity of experimental and operational infrared, optical, and ultraviolet BMDO space-based sensors.

d) *CB-07 Zodiacal Fine Scale Structure* - The objectives of this experiment were to measure the physical and spatial properties of the zodiacal dust bands, cometary debris trails, and possible background enhancements at or near the planetary Lagrangian points.

e) *CB-09 Asteroids, Comets, and Planets* - This experiment was designed to measure the physical, spatial, and temporal IR properties of asteroids, comets, planets and their satellites. The focus was on periodic comets and comets of opportunity, and comet-like asteroids.

#### B). On-Orbit SPIRIT III Characterization

a) *Outline of SPIRIT III On-Orbit Characterization Scheme and Experiment Plans* - During the SPIRIT III testing phase it became evident that a number of the SPIRIT III radiometer and interferometer parameters, such as the point response function, off-axis rejection, flat-field, pointing and alignment, responsivity, and spectral calibration, could not be measured in the laboratory, but would require determination after the telescope was in orbit. As an agent of the MSX Celestial Science Team, we undertook the task of developing a scheme to perform these system characterizations. We defined eleven experiment plans that were subsequently developed for flight by the Space Dynamics Laboratory of Utah State University. These were: DC-08 *SPIRIT III Earthlimb OFVR Characterization*, DC-31 *Small Angle OFVR Characterization*, DC-32 *Lunar OFVR Characterization*, DC-33 *Flat Field Calibration, Mirror Scan Mode*, DC-34 *Flat Field Calibration, Earthlimb Mode*, DC-35 *SPIRIT III Stellar Radiometric Calibration*, DC-37 *Interferometer Wavelength Calibration*, DC-38 *Interferometer Spatial Domain Characterization*, DC-43 *SPIRIT III Source Transfer Experiment*, DC-44 *SPIRIT III Benchmark and Dark Offset Experiment*, and DC-66 *SPIRIT III Sensor Cover Release and First-Light Experiment*. These are archived in the MSX Data Certification and Technology Transfer (DCATT) EP-150200 document series.

b) *DC-29 Support* - The MSX DCATT Experiment Plan DC29, *Pointing and Alignment Experiment* was designed to establish the absolute pointing of the MSX optical bench and the inter-sensor alignments between the optical bench and the SPIRIT III, UVISI, and SBV boresites. To achieve their goals, DC-29 proposed to observe celestial fields containing several stars that were detectable by SPIRIT III and had well known precise celestial coordinates. We were asked to identify those celestial fields that were suitable for their purpose. Our study produced a 43 page report, *Star Fields Recommended for Observation During DC-29, Pointing and Alignment Experiment* by Russell G. Walker and Martin Schlapfer (March 31, 1995). The report contained 11 fields suitable for each of DC29's 3 experiment timelines, the range of applicable dates, and the quaternions required for pointing and orientation of the MSX spacecraft. These fields were successfully used in all DC-29 data collection events.

#### C). Coding of Special Data Processing Software for PL DAF

a) The Diffuse Background File Generator (DBFGEN) was developed to create time ordered scan files of the diffuse background observed by SPIRIT III. The DBFGEN files would be the MSX analog of the IRAS Zodiacal History Files. The software removed point sources from the data stream; spatially coadded the data into low resolution ( $0.25^\circ \times .25^\circ$ ) and high resolution ( $0.25^\circ \times 0.9375'$ ) bins; and reformatted the output into FITS tables. Point source removal was accomplished by the user's choice of either a moving median filter, or by a

constrained least squares cubic spline fit to the background and application of Bloom's Theory of Ordered Statistics. DBFGEN was to be run as a part of the PL DAF pipeline (non-interactive) processing. The software and documentation was delivered to the PL DAF in February, 1994. Due to later changes in the pipeline structure, DBFGEN was not used. It was replaced by a similar algorithm that operated on one of the outputs of the image construction and point source extraction module.

b) To aid the classification of point sources detected by SPIRIT III a program, ASTID, was written to associate each point source detection with naturally occurring known point sources of infrared flux of solar system origin. The intent was that this program would be run interactively on the catalog of point source detections produced on a DCE by DCE basis. The ASTID software code was delivered in February, 1994. As the MSX program progressed ASTID was modified (ASTCAT) to produce DCE-related mini-catalogs of solar system objects that could be readily associated with the final MSX point source catalogs using the identical software as used for other IR catalogs (see discussion of ASTCAT in Section 4, Data Analysis).

#### D). Scheduling MSX Celestial Backgrounds Observations

a) CB-02 *Celestial High Density Regions* - We developed the scheduling code for CB-02 and scheduled 85 data collection events (DCE). Sixty-five were executed successfully, with 5 cancelled and 15 scheduled after loss of cryogen.

b) CB-03 *Deep Galactic Plane Maps* - We developed the scheduling code for CB-03 and scheduled 29 DCEs. Twenty-six were executed successfully, with 3 being cancelled to permit execution of higher priority observations.

c) CB-04 *Areas Missed by Other Experiments* - We developed a special scheduling code to enable the long scans of the missed areas to be executed at times that also satisfied the needs of experiment CB-07. Times were chosen such that the scans sampled the zodiacal cloud over a wide range of solar elongation angles, both that overlapped with IRAS and COBE data and extended the sampled region to the anti-sun direction. Sixty-four DCEs were scheduled and successfully executed.

d) CB-06 *Celestial Radiometric Standards* - We developed intricate scheduling code that linked the observations of three stars within a single DCE. This allowed these stars to be inter-compared with a minimum of lapsed time, alleviating the need for long term radiometric stability. We scheduled a total of 33 "triads", of which 24 were executed successfully and one was cancelled by a higher priority observation.

e) CB-09 *Asteroids, Comets, and Planets* - We developed a code and method of scheduling the observations of these moving targets. The orbital elements of some of the comets of opportunity, such as, Hale-Bopp, Hyakutake, and Tabur, required frequent updating prior to the actual observation. The code also provided the spacecraft scan orientation to optimize detection of debris along the comet's orbit. We scheduled 16 CB-09 DCEs, and successfully observed comets: Hyakutake, Spacewatch, Kopff, Hale-Bopp, Tabur, IRAS, Wirtanen, and Temple-Tuttle; and asteroids: 4015 Wilson-Harrington, 4179 Toutatis, 3200 Phaeton, and 4197 1982TA. One observation was cancelled due to low priority and two were scheduled after loss of cryogen.

## **6. Vanguard/Jamieson Scientists and Engineers who Contributed to this Research**

Dr. Russell G. Walker, Principal Investigator  
Dr. Martin Cohen, Co-Investigator  
Dr. Sumita Jayaraman, Astronomer  
Dr. David Lien, Astronomer  
Martin Schlapfer, Computer Programmer  
Elizabeth Barker, Computer Assistant (Graduate Student)  
Scott Liu, Computer Assistant (Graduate Student)

## **7. Appendix A. Sky Model Extension Papers**



A MODEL OF THE 2–35  $\mu\text{m}$  POINT SOURCE INFRARED SKY

MARTIN COHEN

Jamieson Science &amp; Engineering, Inc., 5321 Scotts Valley Drive, Suite 204, Scotts Valley, California 95066

Electronic mail: cohen@bkyast.berkeley.edu

Received 1992 August 17; revised 1992 December 21

## ABSTRACT

The Point Source Infrared Sky Model of Wainscoat *et al.* [ApJS, 83, 111 (1992)] is extended to make predictions for any filter lying wholly within the range 2.0 to 35.0  $\mu\text{m}$ . The development of a library of complete 2–35  $\mu\text{m}$  low-resolution spectra (with 0.1  $\mu\text{m}$  step size) that represent the 87 categories of Galactic object and four types of extragalactic source implicit in the Model supports this extension. This library is based upon the “spectral template” technique whereby existing spectral fragments for individual sources (from ground-based, airborne, and satellite-borne instruments) are combined into complete spectra. Templates provide a natural way to represent the complete spectral energy distributions of celestial sources for which only infrared photometry and/or partial spectroscopy are available. Consequently, templates bear upon the important general problem of establishing midinfrared calibration sources. The new Model is validated by comparison with broadband  $K$  (2.2  $\mu\text{m}$ ) source counts.

## 1. INTRODUCTION

This paper describes a broader wavelength extension of the Sky Model for the point source infrared sky recently presented by Wainscoat *et al.* (1992: hereafter WCVWS). WCVWS demonstrate that their Model predicts cumulative source counts ( $\log N, \log S$ ) that agree with source counts observed by *IRAS* extremely well (to within better than 0.5 dex in  $\log N$ ) across the entire sky at broadband 12 and 25  $\mu\text{m}$  wavelengths, and well within 0.2 dex for high and intermediate Galactic latitudes. The success of these comparisons essentially vindicates the formalism of the Model code, the geometry of its components, critical selections from the literature of absolute magnitudes, scale heights, and population densities for the many categories of celestial source represented in it.

The Model comprises broadband infrared filters ( $J$ ,  $H$ ,  $K$ , [2.4], and *IRAS* 12 and 25  $\mu\text{m}$ ) and has the capacity to operate continuously for any filter lying entirely within the range of the *IRAS* Low Resolution Spectrometer (LRS), namely 7.67–22.74  $\mu\text{m}$ . It is the purpose of the present paper to extend the validity of the Model to the complete 2.0–35.0  $\mu\text{m}$  range. Section 2 treats infrared “spectral templates” and their relevance to the library from which the Model draws its continuous spectral information. Section 3 describes the construction of templates in detail. As a consequence of the extension in spectral range, some of the absolute magnitude tables used by WCVWS have been revised. These changes are described in Sec. 4. Section 5 compares the new Model’s predictions with observed 2.2  $\mu\text{m}$  point source counts.

The quality of agreement between Model predictions and observations does not imply the uniqueness of this Model. However, its primary function is to predict the statistical appearance of the sky, across its wavelength range of validity, to far fainter flux levels than those of any

existing surveys and in passbands unrelated to current ones. Consequently, the new version of the Sky Model, with its expanded wavelength domain, is capable of providing information of material assistance to the planning of future infrared surveys (ISO, 2MASS, DENIS, SIRTf), and the interpretation of current databases (*IRAS*, *COBE*), because it predicts the expected density of sources at any flux level and in arbitrary passbands across the sky.

## 2. SPECTRAL TEMPLATES

The categories of celestial source represented in the Model include both optically known normal stars and non-stellar objects, and the highly evolved red giants of both carbon- and oxygen-rich sequences that are extremely luminous at midinfrared wavelengths. Each category has an associated complete LRS spectrum. Extension to the 2–35  $\mu\text{m}$  realm, therefore, hinges upon the replacement of the library of LRS spectra by a set of complete 2–35  $\mu\text{m}$  spectra.

Because this library includes an extremely diverse range of objects, the approach favored for the construction of the library is a semiempirical one, based upon the extraction from the literature of fragments of real spectra obtained for a wide variety of infrared sources, by different instruments, and in several spectral regions.

The first step is identification of specific real objects to represent each of the many spectral categories used in the Model. To accommodate natural dispersion in properties, one would like to select at least two sources per celestial category, but this is not always possible for extremely rare categories. Table 1 summarizes the categories of source required by the Model (cf. WCVWS for their definitions); the objects chosen to represent these categories for which at least partial infrared spectral information exists; and the references for the fragments available.



TABLE 1. Model categories of source; individual objects and spectral fragments chosen to represent them.

Category/ Source/LRS?	Total Range ( $\mu\text{m}$ )	References
<u>B0,1 V</u>		
{ $\zeta$ Oph}	1.3-2.6, 2.6-4.0	Strecker (unpublished archive)
$\alpha$ Vir		used photometry, LRS, and blackbody
<u>B2,3 V</u>		
{102 Her*}	1.2-2.5, 2.9-4.0	Bregman & Witteborn (unpublished)
$\alpha$ Eri		used photometry, LRS, and blackbody
<u>B5 V</u>		
$\alpha$ Leo	2.0-5.70	Bregman & Witteborn (unpublished)
$\alpha$ Gru		used photometry, LRS, and blackbody
<u>B8-A0 V</u>		
$\alpha$ CMa	1.2-4.1	Strecker et al. 1979
<u>A2-5 V</u>		
$\alpha$ Gem		used photometry, LRS, and blackbody
$\alpha$ Psa		used photometry, LRS, and blackbody
<u>F0-5 V</u>		
$\alpha$ Aql		used photometry, LRS, and blackbody
$\alpha$ CMi		used photometry, LRS, and blackbody
<u>F8 V</u>		
{ $\theta$ Per}	1.2-2.5, 2.9-4.0	Bregman & Witteborn (unpublished)
$\beta$ Vir		used photometry, LRS, and blackbody
44 Dra		used photometry, LRS, and blackbody
$\beta$ Cap		used photometry, LRS, and blackbody
<u>G0-2 V</u>		
BS 2721		used photometry, LRS, and blackbody
$\alpha$ Cen		used photometry, LRS, and blackbody
<u>G5 V</u>		
$\delta$ Pav		used photometry, LRS, and blackbody
<u>G8-K3 V</u>		
BS 8832	1.2-2.5, 2.9-4.0	Bregman & Witteborn (unpublished)
HR 365		used photometry, LRS, and blackbody
Gliese 324A		used photometry, LRS, and blackbody
<u>K4-5 V</u>		
61 Cyg A		used photometry, LRS, and blackbody
Gliese 365		used photometry, LRS, and blackbody
<u>M0-1 V</u>		
{Gliese 15A}	1.2-2.5, 2.9-4.0	Bregman & Witteborn (unpublished)
Gliese 546		used photometry, LRS, and blackbody
HD 36395		used photometry, LRS, and blackbody
<u>M2-3 V</u>		
Gliese 411	1.3-2.5, 2.9-4, 8-13	Berriman and Reid 1987
<u>M4-5 V</u>		
{Gliese 447*}	2.9-4.0	Berriman and Reid 1987
Gliese 699*	1.3-2.5, 2.9-4.0	Berriman and Reid 1987
Gliese 752A*	1.3-2.5, 2.9-4.0	Berriman and Reid 1987
<u>M-late V</u>		
Gliese 406*	1.3-2.5, 2.9-4, 8-13	Berriman and Reid 1987
Gliese 866*	1.3-2.5, 2.9-4.0	Berriman and Reid 1987
GJ 1111*	1.3-2.5, 2.9-4.0	Berriman and Reid 1987

TABLE 1. (continued)

Category/ Source/LRS?	Total Range ( $\mu\text{m}$ )	References
<u>F8-G2 III</u>		
$\alpha$ Aur	1.2-2.3, 3.0-4.1 4.5-5.6	Bregman (unpublished) used photometry, LRS, and blackbody
$\epsilon$ Leo		
<u>G5 III</u>		
$\alpha$ Aur	1.2-2.3, 3.0-4.1 4.5-5.6	Bregman (unpublished) used photometry, LRS, and blackbody?
$\sigma$ UMa		
<u>G8 III</u>		
$\eta$ Dra		used photometry, LRS, and blackbody
$\kappa$ Cyg	1.2-2.5, 2.9-4.0	Bregman & Witteborn (unpublished)
<u>K0,1 III</u>		
$\beta$ Gem	1.2-4.2, 4.5-5.7	Strecker et al. 1979
$\alpha$ UMa	1.2-4.1, 4.5-5.2	Strecker et al. 1979
$\alpha$ Boo	1.2-4.3	Strecker et al. 1979
<u>K2,3 III</u>		
$\gamma$ 1 And	1.2-2.4, 2.9-4.2, 4.5-5.5	Strecker et al. 1979
<u>K4,5 III</u>		
$\alpha$ Tau	1.2-4.2, 4.5-5.5 3.0-5.6 20.0-35.1	Strecker et al. 1979 Bregman (unpublished) Glaccum 1990
<u>M0 III</u>		
$\mu$ Uma	2.1-2.5, 2.8-4.0	Merrill and Stein 1976a
$\beta$ And	1.2-4.2, 4.5-5.5	Strecker et al. 1979
<u>M1 III</u>		
$\alpha$ Cet	1.3-2.4, 2.9-4.2, 4.5-5.7	Strecker et al. 1979
<u>M2 III</u>		
$\beta$ Peg	1.2-4.2, 4.5-5.7	Strecker et al. 1979
<u>M3 III</u>		
$\delta$ Vir	2.1-2.5, 2.9-4.0	Merrill and Stein 1976a
<u>M4 III</u>		
$\delta$ 2 Lyr	2.9-4.0	Noguchi et al. 1977
$\rho$ Per	2.9-4.0	Noguchi et al. 1977
<u>M5 III</u>		
TU CVn	1.2-2.4, 2.9-5.4 2.0-2.5	Strecker (unpublished) Arnaud et al. 1989
<u>M6 III</u>		
RZ Ari	2.1-2.5, 2.9-4.0	Merrill and Stein 1976a
g Her	1.2-2.6, 2.6-4.0 8-13	Strecker (unpublished) Merrill and Stein 1976a
<u>M7 III</u>		
RX Boo	2.1-2.5, 2.9-4.0 5.1-7.8 15.7-30.1 20.0-35.1	Merrill and Stein 1976a Bregman (unpublished) Forrest, McCarthy, and Houck 1979 Glaccum 1990
<u>YOUNG OB</u>		
$\gamma$ 2 Vel	1.4-2.5, 2.8-4.2, 7.9-13.3	Aitken, Roche, and Allen 1982

TABLE 1. (continued)

Category/ Source/LRS?	Total Range ( $\mu\text{m}$ )	References
$\beta$ Ori	1.2-2.5, 2.9-4.0	Bregman and Witteborn (unpublished)
P Cyg	1.2-2.6, 2.6-4.3	Strecker (unpublished)
<u>A-G I-II</u>		
$\alpha$ Cyg	2.0-5.70	Bregman and Witteborn (unpublished)
$\alpha$ UMi	1.2-4.2, 4.5-5.6	Strecker et al. 1979
$\beta$ Dra	1.2-4.3	Strecker et al. 1979
<u>K-M2 I-II</u>		
$\alpha$ Ori	2.1-2.5, 2.9-4.0, 4.5-13.6 15.9-38.4 20.0-35.1	Puetter et al. 1977 Forrest, McCarthy, and Houck 1979 Glaccum 1990
$\mu$ Cep	2.1-2.5, 2.8-4.0, 4.5-13 15.7-30.1 20.0-35.1	Merrill and Stein 1976a Forrest, McCarthy, and Houck 1979 Glaccum 1990
$\alpha$ Sco	1.2-2.6, 2.6-4.0 4-8 20.0-35.1	Strecker (unpublished) Bregman and Witteborn (unpublished) Glaccum 1990
<u>M3-4 I-II</u>		
$\alpha$ 1 Her	1.2-2.6, 2.6-4.0 5.3-8.0 19.9-35.0	Strecker (unpublished) Cohen (unpublished) Glaccum 1990
[RW Cyg]	2.1-2.5, 2.8-4.0, 8.0-13.0	Merrill and Stein 1976a
<u>AGB M 01</u>		
R Lyr	2.9-4.1	Noguchi et al. 1977
TU CVn	2.0-2.5	Arnaud et al. 1989
<u>AGB M 03</u>		
R Leo	1.2-4.1 8.0-13.0 20.0-35.1	Strecker, Erickson, and Witteborn 1978 Merrill and Stein 1976a Glaccum 1990
<u>AGB M 05</u>		
R Cas	1.2-4.1 2.1-2.5, 2.9-4.0, 4.5-13.6 15.7-30.1 20-35	Strecker, Erickson, and Witteborn 1978 Puetter et al. 1977 Forrest, McCarthy, and Houck 1979 Glaccum 1990
TX Cam	2.1-2.5, 2.9-4.0, 8.0-13.0 3.0-5.6	Merrill and Stein 1976b Bregman (unpublished)
R LMi	5.3-8.0	Cohen (unpublished)
<u>AGB M 07</u>		
RS Cnc	2.1-2.5, 2.8-4.0, 8.0-13	Merrill and Stein 1976a
$\alpha$ Cet	2.1-2.5, 2.9-4.0, 8.0-13.0 4.4-5.4 16.3-29.1	Merrill and Stein 1976a Scargle and Strecker 1979 Glaccum 1990
<u>AGB M 09</u>		
NML Tau	1.2-4.1	Strecker, Erickson, and Witteborn 1978

TABLE 1. (continued)

Category/ Source/LRS?	Total Range ( $\mu\text{m}$ )	References
GL 1141	20.0-35.1 2.1-2.5, 2.9-4.0, 8-12.5	Glaccum 1990 Merrill and Stein 1976b
X Her	15.7-30.0 20.1-35.2	Forrest, McCarthy, and Houck 1979 Glaccum 1990
+70066	1.2-2.4, 2.9-5.6	Strecker (unpublished)
<u>AGB M 11</u>		
+40149	2.1-2.5, 2.9-4.0, 8-12.6	Merrill and Stein 1976b
GL 2241	2.0-2.5, 2.8-4.0, 7.8-13.3 6.4-7.7	Cohen (unpublished) Bregman and Witteborn (unpublished)
CIT 1	2.1-2.5, 2.9-4.0, 8-12.8	Merrill and Stein 1976b
WX Ser	1.4-2.5, 2.9-3.8	Jones et al. 1988
<u>AGB M 13</u>		
+00102	2.1-2.5, 2.9-4.0, 8-12.5	Merrill and Stein 1976b
+10011	2.1-2.5, 2.9-4.0, 8-13.2	Merrill and Stein 1976b
+20326	2.1-2.5, 2.9-4.0, 8-13.3	Merrill and Stein 1976b
GL 1686	2.4-8.0 8.0-13.0	Bregman and Witteborn (unpublished) Merrill and Stein 1976c
<u>AGB M 15</u>		
+40156	2.1-2.5, 2.9-4.0, 8.0-13.1	Merrill and Stein 1976b
<u>AGB M 17</u>		
GL 3022	2.0-2.4, 3.0-4.0, 8.0-13.1	Eiroa et al. 1981
PZ Cas	15.9-38.4	Forrest, McCarthy, and Houck 1979
<u>AGB M 19</u>		
+50137	2.1-2.5, 2.9-4.0, 8.0-13.4	Merrill and Stein 1976b
<u>AGB M 21</u>	used average of AGB M 19 and AGB M 23	
OH 23.1-0.3		used photometry, LRS, and 2 blackbodies
OH 26.2-0.6	1.4-1.8, 2.0-2.5	Jones et al. 1988
<u>AGB M 23</u>		
GL 2885	2.1-2.5, 2.9-4.0, 8.0-13.0 2.4-3.3	Merrill and Stein 1976c Knacke et al. 1985
OH26.5+0.6	2.1-2.5, 2.9-4.0, 4.5-37.5 2.5-3.3	Forrest et al. 1978 Knacke et al. 1985
<u>AGB M 25</u>		
OH 35.6-0.3		used photometry, LRS, and 2 blackbodies
OH 42.3-0.2		used photometry, LRS, and 2 blackbodies
<u>AGB C 01</u>		
Y CVn	1.2-2.4, 2.9-4.1, 4.3-5.6	Goebel et al. 1978

TABLE 1. (continued)

Category/ Source/LRS?	Total Range ( $\mu\text{m}$ )	References
TX Psc	16.5-29.5	Forrest, Houck, and McCarthy 1981
AGB C 03	1.2-2.4, 2.9-4.1	Goebel et al. 1978
UU Aur	1.2-2.4, 2.9-5.5	Strecker (unpublished)
	4.5-7.8	Bregman (unpublished)
V CrB	1.3-2.6, 2.6-4.2	Strecker (unpublished)
	4.4-7.8	Bregman (unpublished)
R Lep	1.2-2.6, 2.6-3.2, 2.9-5.6	Strecker (unpublished)
AGB C 05		
V Cyg	2.1-2.5, 2.9-4.0, 4.5-13.6	Puetter et al. 1977
	16.5-29.5	Forrest, Houck, and McCarthy 1981
	31-110	Goebel and Moseley 1985
S Cep	1.3-2.4, 2.9-4.1, 4.3-5.4	Goebel et al. 1978
	16.5-29.5	Forrest, Houck, and McCarthy 1981
	31-51	Goebel and Moseley 1985
AGB C 07		
V Hya	2.9-4.1	Noguchi et al. 1977
AGB C 09		
T Ara		used photometry, LRS, and 2 blackbodies
V644 Sco		used photometry, LRS, and 2 blackbodies
SZ Sgr		used photometry, LRS, and 2 blackbodies
AGB C 11		
TT Cen		used photometry, LRS, and 2 blackbodies
AGB C 13		used photometry, LRS, and blackbody
AGB C 15		used photometry, LRS, and blackbody
AGB C 17		used photometry, LRS, and blackbody
AGB C 19		
HD 100764		used photometry, LRS, and 2 blackbodies
AGB C 21	taken equal to AGB C 19 template	
AGB C 23	taken equal to AGB C 19 template	
AGB C 25	taken equal to AGB C 19 template	
AGB CI 01		
GL 527	2.1-2.5, 2.9-4.0, 8-12.9	Merrill and Stein 1976b
AGB CI 03		
GL 799	2.0-2.5, 2.8-4.0, 7.8-13.3	Cohen 1984
GL 933	2.1-2.5, 2.9-4.1	Merrill and Stein 1976b
AGB CI 05		
CIT 6/GL 1403	1.2-2.4, 2.9-5.4 2.1-2.5, 2.9-4.0, 7.8-13.4 5.6-7.6 16.5-29.5 16-30, 31-51	Strecker (unpublished) Cohen 1984 Witteborn and Bregman (unpublished) Forrest, Houck, and McCarthy 1981 Goebel and Moseley 1985
CIT 5	2.1-2.5, 2.9-4.0,	

TABLE 1. (continued)

Category/ Source/LRS?	Total Range ( $\mu\text{m}$ )	References
	8-13.1	Merrill and Stein 1976b
	15.8-30	Forrest, Houck, and McCarthy 1981
	31-51	Goebel and Moseley 1985
<u>AGB CI 07</u>		
GL 2232	2.1-2.5, 2.9-4.0, 7.8-13.3	Cohen 1984
GL 2392	2.1-2.5, 2.9-4.0, 7.8-13.3	Cohen 1984
GL 2310	2.1-2.5, 2.9-4.0, 8.0-13.2	Merrill and Stein 1976b
<u>AGB CI 09</u>		
+10216/GL 1381	1.8-2.6, 2.8-5.5	Strecker (unpublished)
	2.0-8.5	Witteborn et al. 1980
	7.8-13.2	Cohen 1984
	15.7-30	Forrest, Houck, and McCarthy 1981
	31-180	Goebel and Moseley 1985
GL 3116	2.1-2.5, 2.9-4.0, 7.8-13.3	Cohen 1984
	15.8-30	Forrest, Houck, and McCarthy 1981
<u>AGB CI 11</u>	used average of AGB CI 11 and 13	
<u>AGB CI 13</u>		
GL 2699	2.1-2.5, 2.9-4.0, 7.8-13.3	Cohen 1984
GL 3099	2.1-2.5, 2.9-4.0, 7.8-13.4	Cohen 1984
<u>AGB CI 15</u>		used photometry, LRS, and blackbody
<u>AGB CI 17</u>		
GL 3068	2.1-2.5, 2.9-3.6, 8-13.4	Jones et al. 1978
	8.0-13.4	Cohen 1984
	15.8-30	Forrest, Houck, and McCarthy 1981
	31-150	Goebel and Moseley 1985
<u>AGB CI 19</u>		used photometry, LRS, and blackbody
<u>AGB CI 21</u>	taken equal to AGB CI 19 template	
<u>AGB CI 23</u>	taken equal to AGB CI 19 template	
<u>AGB CI 25</u>	taken equal to AGB CI 19 template	
<u>AGB CI 27</u>	taken equal to AGB CI 19 template	
<u>AGB CI 29</u>	taken equal to AGB CI 19 template	
<u>AGB CI 31</u>	taken equal to AGB CI 19 template	
<u>X 1E</u>		
S Per	1.2-2.6, 2.6-4.0	Strecker (unpublished)
GL 1992	1.4-1.8, 2.0-2.5	Jones et al. 1988
GL 2019	1.4-1.8, 2.0-2.5	Jones et al. 1988
<u>X 1A</u>		
OH 327.4-0.6	1.4-1.8, 2.0-2.5	Jones et al. 1988
OH 30.7+0.4		used photometry, LRS, and 2 blackbodies
OH 32.0-0.5		used photometry, LRS, and 2 blackbodies
OH 32.8-0.3		used photometry, LRS, and 2 blackbodies
OH 75.3-1.8		used photometry, LRS, and 2 blackbodies

TABLE I. (continued)

Category/ Source/LRS?	Total Range ( $\mu\text{m}$ )	References
<u>X 2</u>		
GL 2136	1.6-2.5, 2.8-4.1, 4.5-13.4 5.3-8.0	Willner et al. 1982 Tielens (unpublished)
<u>X 3</u>		
OH 21.5+0.5		used photometry, LRS, and 2 blackbodies
GL 2403		used photometry, LRS, and 2 blackbodies
<u>X 4</u>		
VY CMa	1.2-2.6, 2.6-4.0 5.2-10.2 15.8-30.3 20.0-35.1	Strecker (unpublished) Cohen et al. 1989 Forrest, McCarthy, and Houck 1979 Glaccum 1990
+10420	7.9-13.2 15.6-38.5 19.9-35.0	Giguere, Woolf, and Webber 1976 Forrest, McCarthy, and Houck 1979 Glaccum 1990
OH 337.9+0.2	1.4-1.8, 2.0-2.5	Jones et al. 1988
<u>X 5</u>		
MWC 300	2.1-2.5, 2.8-4.1	Cohen 1975
OH 127.8-0.0		used photometry, LRS, and 2 blackbodies
<u>PN BLUE</u>		
BD+30 3639	2.1-2.5, 2.9-4.1 5.3-8.1 7.9-13.3	Russell, Soifer, and Merrill 1977 Cohen et al. 1986 Aitken and Roche 1982
M2-56	2.1-2.5, 2.9-4.0 5.4-8.0 8.1-13.5	Eiroa, Hefele, and Zhang-Yu 1983 Cohen (unpublished) Roche and Aitken 1986
GL 618	2.1-2.5, 2.8-4.0, 4.5-13.1	Russell, Soifer, and Willner 1978
<u>PN RED</u>		
NGC 6302	1.9-2.5 3.0-3.8 5.3-7.9 7.4-13.5	Ashley and Hyland 1988 Magazzu and Strazzulla 1989 Cohen et al. 1989 Roche and Aitken 1986
NGC 6572	2.1-2.5, 2.9-4.1, 5-14 1.9-2.4 1.3-3.6 5.3-8.1 8.1-13.3 16.5-29.5	Willner et al. 1979 Isaacman 1984 Witteborn and Bregman (unpublished) Cohen et al. 1986 Aitken and Roche 1982 Forrest, Houck, and McCarthy 1981
NGC 7027*	2.1-2.5, 2.9-4.1, 4.5-13.8 15.7-38.5	Russell, Soifer, and Willner 1977 McCarthy, Forrest, and Houck 1978
IC 418	2.1-2.5, 2.9-4.1, 5-14 2.1-2.5, 2.9-4.1 5.3-8.0 16.6-28.5	Willner et al. 1979 Russell, Soifer, and Merrill 1977 Cohen et al. 1986 Forrest, Houck, and McCarthy 1981
Hb 5	3.0-3.8 8-13	Magazzu and Strazzulla 1989 Aitken and Roche 1982

TABLE 1. (continued)

Category/ Source/LRS?	Total Range ( $\mu\text{m}$ )	References
IC 2621	3.0-3.8 8-13	Magazzu and Strazzulla 1989 Aitken and Roche 1982
He 2-131	3.0-3.8 8-13	Magazzu and Strazzulla 1989 Aitken and Roche 1982
IC 4997		used photometry, LRS, and 2 blackbodies
NGC 7026		used photometry, LRS, and 2 blackbodies
<u>RN BLUE</u>		
HD 44179	1.2-2.6, 2.9-5.5 2.1-2.5, 2.8-4.0, 4.5-13 5.2-12.8	Strecker (unpublished)  Russell, Soifer, and Willner 1978 Cohen et al. 1986
NGC 2023	1.2-2.5, 2.8-3.7, 5.2-8.0, 8.7-12.9	Sellgren et al. 1985
<u>RN RED</u>		
NGC 7023	1.2-2.5, 2.8-4.2, 5.2-8.0, 8.7-11.8	Sellgren et al. 1985
Parsamyan 18	2.1-2.3 3.1-3.8 5.2-8.0	Sellgren 1986 Geballe (unpublished) Witteborn, Bregman, Cohen (unpublished)
<u>HII REG</u>		
GL 2591	2.1-2.5, 2.8-4.1, 4.5-13.4	Willner et al. 1982
W3 IRS5	2.0-2.5, 2.8-4.1, 4.5-13.4	Willner et al. 1982
{M1-78}	2.0-2.5 5.3-8.1 8.2-13.4	Isaacman 1984 Cohen et al. 1986 Aitken and Roche 1982
NGC 7538 IRS1	1.6-2.5, 2.8-4.1, 4.5-13.6	Willner et al. 1982
NGC 7538 IRS9	1.6-2.5, 2.8-4.1, 4.5-13.6	Willner et al. 1982
NGC 2170 IRS3	1.2-2.5, 2.8-4.1, 4.5-13.6	Willner et al. 1982
GL 2059	1.7-2.5, 2.8-4.1, 4.5-13.6	Willner et al. 1982
GL 961	1.7-2.5, 2.8-4.1, 4.5-13.6	Willner et al. 1982
GL 989	2.1-2.5, 2.8-4.1, 4.5-13.5	Willner et al. 1982
S 255 IRS 1	1.7-2.5, 2.8-4.1, 4.5-13.6	Willner et al. 1982
OMC2 IRS3*	1.6-2.5, 2.8-4.1, 4.5-13.5	Willner et al. 1982
GL 2884/S140	1.3-2.5, 2.8-4.1, 4.5-13.5	Willner et al. 1982
<u>T TAURI</u>		
HL Tau	2.1-2.5, 2.9-4.1 5.4-8.1 8.0-13.0	Cohen 1975 Witteborn and Bregman (unpublished) Cohen and Witteborn 1985
RY Tau	2.1-2.5, 2.9-4.1	Cohen 1975



TABLE 1. (continued)

Category/ Source/LRS?	Total Range ( $\mu\text{m}$ )	References
	8.0-13.0	Cohen and Witteborn 1985
GW Ori	2.1-2.5, 2.9-4.1	Cohen 1975
	8.0-12.8	Cohen and Witteborn 1985
R Mon	2.1-2.5, 2.9-4.1	Cohen 1975
	7.8-13.4	Cohen 1980
AB Aur	2.1-2.5, 2.9-4.1	Cohen 1975
	8.0-13.0	Cohen and Witteborn 1985
<u>Galaxies</u>		
M82	1.7-2.5, 2.9-4.1, 5.4-13	Willner et al. 1977
	16.0-30.3, 30-39	Houck, Forrest, and McCarthy 1980
	18.6-18.8, 33.3-.5	Houck et al. 1984
NGC 1068	1.2-2.5, 2.8-4.1, 8.1-13.4	Cutri et al. 1981
	16.5-29.7	Houck, Forrest, and McCarthy 1980
NGC 253	2.9-4.0	Russell, Soifer, and Merrill 1977
	5.3-8.0	Witteborn, Bregman, Cohen (unpublished)

## Notes to TABLE 1

IRAS LRS spectra exist for all sources except those whose names are followed by an asterisk. {} denote sources whose spectra were not used in the creation of the average template for their category.

The second step is acquisition of digital files of these spectral fragments by scanning of the published spectra (or larger scale versions thereof, provided by the authors) or by direct electronic transmission by the original observers. By these means, ~500 fragments representing ~180 separate sources were accumulated. Spectral fragments fall naturally into several classes depending on spectral regime, detector technology, and observing site (ground-based, airborne, or satellite-borne). The natural divisions are: 2-4/5; 5-8; 8-13; 7.7-22.7 (the LRS); 15-30; > 30  $\mu\text{m}$ . To give an impression of the availability of fragments in different regions, Table 2 summarizes the total database of spectral fragments assembled in Table 1 and highlights both the relative scarcity of airborne fragments and their critical importance to the construction of reliable complete spectra.

Next comes combination of fragments into complete spectra with appropriate actions to be taken in the complete absence of data in specific regions, and with corrections to be made for photospheric absorptions that might not have been observed in all sources. These details constitute Sec. 3.

TABLE 2. Breakdown of the database of spectra by wavelength region (in  $\mu\text{m}$ ).

$\lambda\lambda$ 1/2-4/5		5-8	8-13	LRS (7.7-22.7)	15-30	30-50
Number	144	43	71	168	34	22
Site	ground	air	ground	IRAS satellite	air	air

The separate, complete spectra on individual sources in a common category must be corrected for purely interstellar extinction, rendering them intrinsic spectra, then normalized, and finally averaged together, yielding the category's representative template. *One implicitly assumes that every source of a particular category may be well-represented by the average intrinsic template created from the spectra of the individual sources used to construct the average.* In this way, the complete library can be reconstructed.

*Note that templates are relevant to the general problem of absolute calibration for airborne and spaceborne infrared detectors in the mid- and long-wavelength-infrared regime.* The problem is to establish standards, often post facto, for a particular flight series or satellite mission that lie within a specific region of the sky and emit strongly within a specific region in the infrared. While there may exist bright sources with the required positions and wavelength coverage, there often is a complete absence of any continuous spectral information on these same sources even at low resolution. If a source can be classified as belonging to one of the 91 categories of the Sky Model then a unique spectral template can be associated with it. All that is required is to normalize that template to match the best broadband photometry available on the individual source. This provides at least a first approximation to an absolute calibration for the source. The template technique has been applied in this context to normal K and early M giants (Walker & Cohen 1989).

### 3. METHODOLOGY

#### 3.1 Digitization of Spectral Fragments

Unless spectra were transmitted electronically, a digitizing scanner was used and the new file compared with the original image. Any small (a few percent) differences in both coordinate scales were attributed to tilts in the axes relative to the scanning frame, or nonlinearities in the reproduction of the original spectra. The digitized data were rectified to match the original, using a slightly different treatment if the original spectrum possessed strong sharp emission features. An interactive graphics routine was written (in the ANA language) to perform the rectification and to convert all original ordinate scales into  $F_\lambda$  (in  $\text{W cm}^{-2} \mu\text{m}^{-1}$ ) and all abscissae into wavelength (in  $\mu\text{m}$ ).

Some spectra were obtained from original sources in digital form, namely: the absolutely calibrated 1.2–5.5  $\mu\text{m}$  spectra by Strecker *et al.* (1979); and unpublished airborne spectra between  $\sim 16$  and 65  $\mu\text{m}$  of bright sources secured by Dr. W. Glaccum as part of his Ph.D. research (Glaccum 1990) and very kindly made available in advance of publication.

Witteborn (1990) and Bregman (1990) very kindly made available the copious databases at NASA-Ames of ground-based and airborne circular variable filter 1.2–5.5  $\mu\text{m}$  spectra, and many airborne 4–8  $\mu\text{m}$  multiplex spectra. Strecker (1990) kindly supplied his unpublished archive of airborne spectra [from which Strecker *et al.* (1979) was culled] in original form, to be scanned. A critically useful database is provided by the *IRAS* LRS instrument. NASA-Ames has a copy of the Groningen database of  $\sim 171\,000$  point-source-extracted spectra which was crucial in extending ground-based coverage and bridging to longer wavelength data taken from NASA's Kuiper Airborne Observatory (KAO).

#### 3.2 Scaling and Merging of Spectra

Some spectra are published in absolute units; others appear only with relative ordinates but absolute scaling of a fragment was always achieved by direct comparison with photometry from the literature, converted into monochromatic spectral flux densities, and plotted on the spectrum. Thus, fragments can be scaled relative to one another. The ANA routines devised involve preservation of spectral shape and gradients, matching of  $F_\lambda$  levels in adjacent spectral bands, and simultaneous matching of each fragment to the available photometry. Even if photometry is absent in some region, overlapping by, and matching to, adjacent fragments will result in a valid spectral shape. *IRAS* photometry also assisted: the flux densities from the *Point Source Catalog* version 2 (1988: hereafter PSC2) were converted into  $F_v$ , using standard filter bandwidths (cf. *IRAS* Explanatory Supplement 1988, page X-13), color-corrected appropriately for the source under consideration (cf. *IRAS* Explanatory Supplement 1988, page VI-27), then converted into  $F_\lambda$ .

A detailed description of typical splicing routines is given by Cohen *et al.* (1992, hereafter referred to as CWW). After achieving the best matches of fragments to each other and to the photometric points, the final spectrum was represented in regions of overlap by the data judged to have the best signal-to-noise after due consideration of atmospheric transmission. For some sources, existing fragments permitted the immediate creation of a complete spectrum from 2–35  $\mu\text{m}$ . This was then regridded to a uniform wavelength scale, with step size 0.1  $\mu\text{m}$ , by linear interpolation to provide the final spectrum of each such source. This step is coarse for 1–5  $\mu\text{m}$ , degrading the spectral resolution; it is well-matched to 5–8  $\mu\text{m}$  KAO spectra, but oversamples LRS and long wave KAO data. It adequately represents typical features encountered, most of which are broad (e.g., CO and SiO fundamentals and first overtones; silicate and SiC features; ice absorptions; steam bands). Further, 0.1  $\mu\text{m}$  steps avoid severe degradation of the spectra of sources with emission lines.

#### 3.3 Interpolating and Extrapolating Spectra

Many sources lack spectra somewhere between 2 and 35  $\mu\text{m}$ . Typical ground-based near-infrared spectra cover  $\sim 2.0$ –2.5 and  $\sim 2.9$ –4.0  $\mu\text{m}$  with a gap from  $\sim 2.5$ –2.9  $\mu\text{m}$  due to terrestrial absorption by water and CO<sub>2</sub>. Frequently, the entire 4/5–8  $\mu\text{m}$  region is absent because no one has obtained an airborne spectrum and even KAO spectra have a gap due to terrestrial CO<sub>2</sub> band from 4.27–4.47  $\mu\text{m}$  (cf. Strecker *et al.* 1979). The longest wavelength data are scarce because they too depend upon KAO observations. Even if these do exist, they may cover only the 16–30  $\mu\text{m}$  region, again necessitating extrapolation to 35  $\mu\text{m}$ . Given only an *IRAS* LRS spectrum, one must extrapolate longward of 22.7  $\mu\text{m}$ .

The approximation that always involves fewest assumptions about the infrared *continuum* of a source is to use a blackbody for the unobserved piece of spectrum. Below 8.0  $\mu\text{m}$ , on normal stars, I used blackbodies corresponding to the stellar effective temperature [cf. Ridgway *et al.* (1980) for K and M giants]. Extreme AGB stars were represented by a combination of two blackbodies; one matched to broadband photometry and short LRS data, the other such that the sum of both blackbodies matched the longest LRS data and photometry. Highly extreme AGB stars, with the reddest [12]–[25] indices, often lack short wave photometry. For those, I generated [2.2] from the AGB evolutionary models described in the Appendix of WCVWS which supply theoretical approximations to the spectral energy distributions of these highly evolved stars. These spectra are so steep that a combination of photometry, an LRS spectrum, and a single blackbody suffices to represent these sources.

One source may lack fragments but a second source in the same category has complementary fragments. The latter were substituted for the absent fragment of the first source. For example, in the category AGB M 17, where GL 3022 has 2–4, 8–13  $\mu\text{m}$ , and LRS data, X Her has only

a KAO 16–40  $\mu\text{m}$  fragment. Both were combined to create “a complete spectrum” for GL 3022, the better represented source.

In the absence of the longest wave data, the best fitting (cool) blackbody to the LRS and/or 8–13 and/or 16–30  $\mu\text{m}$  fragments were extrapolated, guided by ground-based 18/20/22 and/or *IRAS* 25  $\mu\text{m}$  photometry.

### 3.4 Variable Stars

Many of the categories are intrinsically variable. I attempted to select nearly contemporaneous photometry, or to use the upper envelope of the photometric points at each wavelength. Of course, there are never sufficient spectra to match fragments to photometry at the appropriate phases in the cycles of these (typically Mira) variable stars. Indeed, it is not yet known whether spectra of extreme AGB stars beyond 8  $\mu\text{m}$  vary with light curve phase.

However, it is encouraging that the 8–13  $\mu\text{m}$  spectra observed in the 1970s for such stars substantially overlap much more recent *IRAS* LRS spectra, suggesting this method adequately represents the spectra of many of these stars.

To illustrate the technique, Fig. 1 shows the construction of the entire 2–35  $\mu\text{m}$  spectrum for V Cyg which, though nominally variable, possesses a complete set of fragmentary spectra. CWW describe a more quantitative technique in detail.

### 3.5 Problems with “Normal” Stars

“Normal” stars can pose substantial difficulties in the infrared both for general templating or for the provision of absolute flux calibrators. Even if stars earlier than K have LRS spectra, these fall so fast that signal-to-noise ratios are unacceptable beyond  $\sim 10 \mu\text{m}$ . To provide spectra of the early dwarfs, I utilized the best-fitting blackbody to the LRS spectrum and photometry (often the *IRAS* 12 and 25  $\mu\text{m}$  points constituted the sole photometry beyond 5  $\mu\text{m}$ ). This blackbody could be substituted for the absent spectral fragments both above and below the LRS range, and even for some, or all, of an unacceptably noisy LRS spectrum.

I could not locate a star with an adequate LRS spectrum for some categories. Then I used the closest match by type; e.g.,  $\delta$  Pav (G7 IV) for category “G5 V.”

All LRS spectra were corrected by the function tabulated by Volk & Cohen (1989a). The spectra come directly from the complete Dutch LRS database rather than the incomplete LRS Atlas of Low Resolution Spectra (1986). [An improved set of LRS corrections has very recently been described by CWW but the primary artifact near 8  $\mu\text{m}$  is already accounted for by Volk & Cohen (1989a). Applications of the Sky Model are statistical in nature, its predictions are robust so the slightly erroneous red slope of Volk and Cohen does not constitute a significant problem, by comparison with the newer curve.]

### 3.6 Exotic Objects

For reflection nebulae, planetaries, and galaxies, I scaled fragments according to the apertures originally used, and always compared with the largest aperture photometry or spectra available. For planetary nebulae, both the near-infrared continuum level and emission line peaks were used to assure meaningful rescaling. Some lack any spectra below  $\sim 3.0 \mu\text{m}$ . These were extrapolated shortward of  $\sim 3.0 \mu\text{m}$  by an optically thin free-free continuum (essentially  $F_\lambda \propto \lambda^{-2}$  since the total wavelength range was so small that Gaunt factor variations were negligible). An initial estimate of infrared continuum was made on the basis of known radio continuum flux and extinction, but the free-free level was rescaled by comparison with near-infrared photometry.

The more extreme AGB M stars lack short wavelength fragments, although photometry and LRS spectra exist. Many are OH/IR stars, whose overall spectral energy distributions are defined by the photometry of Hyland *et al.* (1972) and Gehrz *et al.* (1985).

The most extreme AGB C and CI objects have no optical counterparts and no near-infrared photometry. The reddest [12]–[25] indices found for the former were 1.00 (TT Cen) and 1.88 (HD 100764), so I interpolated linearly in [12]–[25] and [2.2]–[12] between these two stars to obtain generic “photometry” for the intervening categories (AGB C 13, 15, 17). These categories were treated by the method involving photometry, an LRS spectrum (defined as the average of the actual LRS spectra of many *IRAS* sources with the desired [12]–[25] indices: cf. WCVWS), and a single blackbody.

### 3.7 Template Generation: Correction for Interstellar Reddening

Once the complete spectra for all the individual sources had been created, I converted these into “templates” as follows. The literature provided an estimate of the purely interstellar component of extinction. For all AGB stars, the dominant source of extinction was assumed to be circumstellar and to be part of the intrinsic character of the star. Therefore, *no dereddening was applied to their spectra*. Individual spectra were checked for artifacts of interpolation, regridding, and splicing. Artifacts were removed by local blackbody interpolation, or subsequently smoothed away. Long wave substitutions by blackbodies were reexamined for improved matches with photometry and spectra using a reddened blackbody suffering the same extinction as determined for the source. The spectra were dereddened (the law described below), except for AGB stars. Intrinsic spectra were smoothed by Gaussians, typically lightly (FWHM 0.5  $\mu\text{m}$ ) from 2–10  $\mu\text{m}$ , but beyond  $\sim 15 \mu\text{m}$ , the FWHM was usually 1.0 (or 1.5)  $\mu\text{m}$ . Region(s) smoothed and degree(s) of smoothing were tailored to the individual spectra. Many bright spectra required either no, or only very limited, smoothing with the

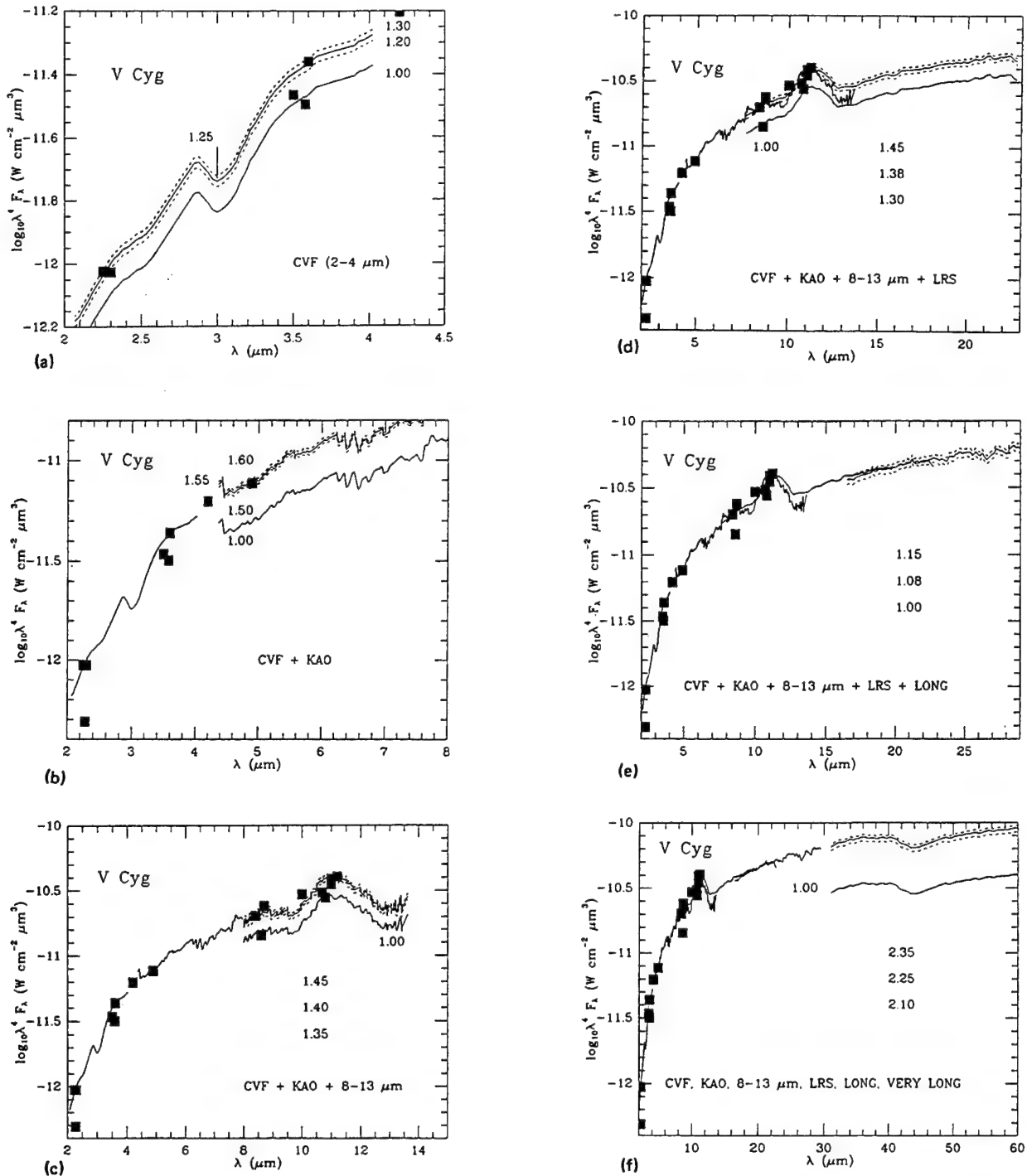


FIG. 1. Sequence of displays representing the construction of the complete 2-35  $\mu\text{m}$  template for the variable V Cyg. Plots are  $\log \lambda^4 F_\lambda$  vs  $\lambda$  to compress the displays for steeply falling spectra (essentially to remove the red pseudo-Rayleigh-Jeans falloff in normal stars). (a) Ground-based CVF data with nominal scaling (1.00 curve) and best match (solid, 1.25) fit to the broadband photometry (filled squares) showing plausible range of scale factors (1.20-1.30) that might also be fit to the photometry. The fitting is designed to favor the upper envelope of the photometry (so that one might renormalize all fragments to the maximum of the star). (b) Matching the CVF and KAO spectra; again, 1.00 represents the curve scanned in the literature which required scaling up by 1.55 (in the range 1.50-1.60 plausibly) to fit both the photometry at 4.2 and 4.9  $\mu\text{m}$  and the already scaled CVF fragment. (c) Merging CVF+KAO with the 8-13  $\mu\text{m}$  spectrum from the literature. Note that the rescaling again favors the upper envelope of the photometry. (d) Merging CVF+KAO+8-13  $\mu\text{m}$  with the *IRAS* LRS spectrum. The finally adopted best-fit involved rescaling by a factor 1.38 over the nominal calibrated average LRS spectrum; the plausible range of this factor is 1.30-1.45 (as represented by the two dashed curves that flank the selected best fit). (e) Further merging with the long wavelength KAO spectrum (from  $\sim 16$ -30  $\mu\text{m}$ ). Best-fit factor=1.08, range 1.00-1.15. (f) Final merging with the longest wavelength KAO data (from  $\sim 30$ -60  $\mu\text{m}$ ) taken at a different epoch from the other fragments and published only in relative units. Best fit factor 2.25, with range 2.10-2.35 (dashed curves). (g) Splicing of CVF and KAO spectral fragments after each has been rescaled. (h) Same for KAO and LRS (the 8-13  $\mu\text{m}$  spectra were used primarily to check the LRS level and shape and provide higher resolution coverage; the long wave LRS was always valuable). (i) Same for LRS and long KAO fragments. (j) Same for long and very long KAO fragments. (k) Composite of all the overlapping spectral fragments and photometry. (l) Complete 2-35  $\mu\text{m}$  spectrum with regridding of the wavelength scale by interpolation (no smoothing or cleaning has yet been performed).

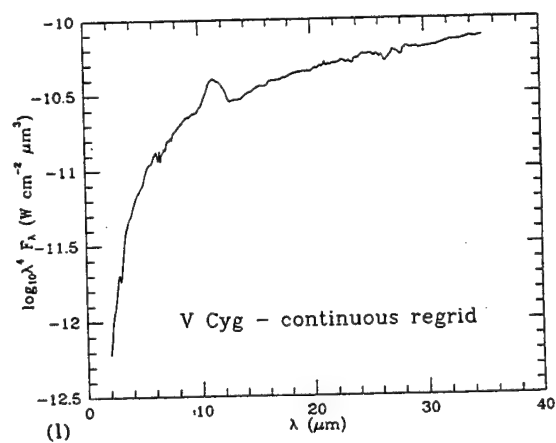
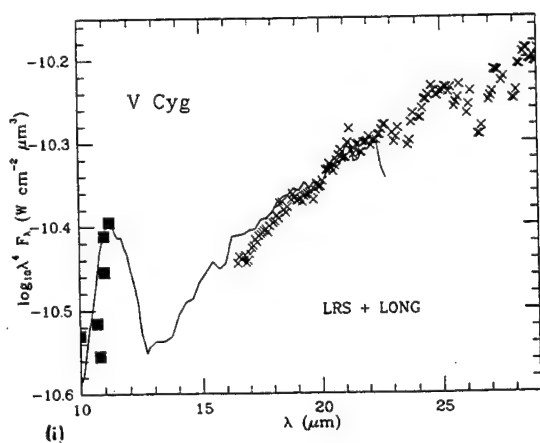
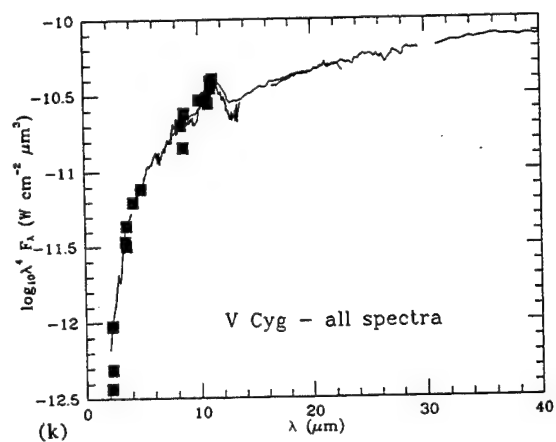
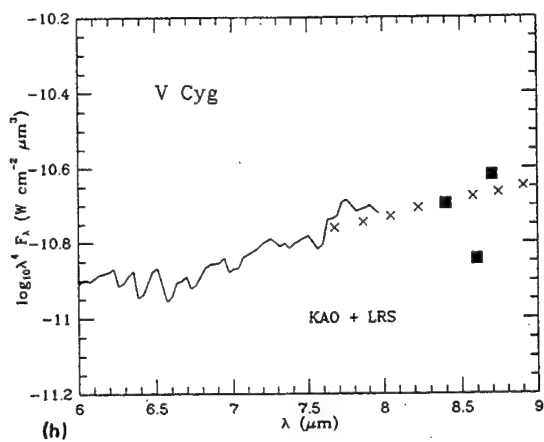
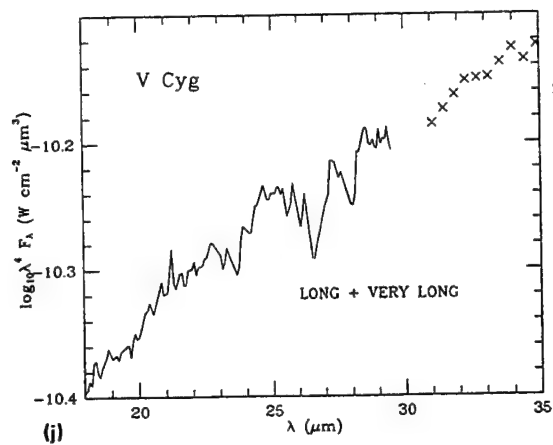
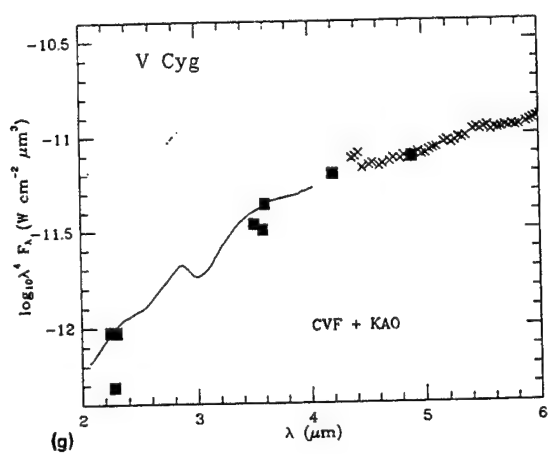


FIG. 1. (continued)

splicing of fragments in regions of overlap. The resulting spectra were normalized for subsequent combination.

WCVWS's law of interstellar extinction was extended by a  $1/\lambda$  extrapolation beyond  $22.7 \mu\text{m}$  and a van der Hulst #15 law below  $7.67 \mu\text{m}$ . Figure 2 presents the complete function,  $A_\lambda/A_V$ .

Smoothed intrinsic (normalized) templates were combined for categories represented by more than a single source. A simple average was used unless a subtemplate was distinct from all the rest (in energy distribution or length of the unobserved section). Such spectra (indicated by source names in {} in Table 1) were omitted from the average.

Exceptions to the averaging process were T Tau Stars and Planetary Nebulae. The former were represented by (4×AB Aur+2×RY Tau+2×GW Ori+HL Tau+R Mon) to achieve the presence and frequency of silicate emission (80%) and of absorption (20% of the class: Cohen & Witteborn 1985).

WCVWS divided planetaries into "blue" and "red" subtypes, depending on [12]–[25] color. Volk & Cohen (1990) summarized the frequencies of occurrence of their distinct archetypal LRS spectral shapes. I first assume that group "F" nebulae (very noisy spectra), would all be placed within the remaining seven groups with the same frequencies as the bulk of the population display, if their spectra were less noisy. Then I treat planetaries as occurring with seven archetypal LRS shapes with the following frequencies (%): D, 7.6; R, 31.0; P, 15.2; L, 6.3; H, 28.5; X, 2.6; E, 8.8 (Volk and Cohen define the letter designations). Spectra are available from the literature for only three "Blue Planetary Nebulae," namely GL 618 (group D), BD+30°3639 and M2–56 (both group P). Group P nebulae are twice as common as group D so the simple average of the spectra of these three nebulae faithfully represents the "PN BLUE" category. Red planetaries span all seven archetypes. Spectra available suggested the following choices: group D, NGC 6572; R, IC 4997; P, IC 418 and

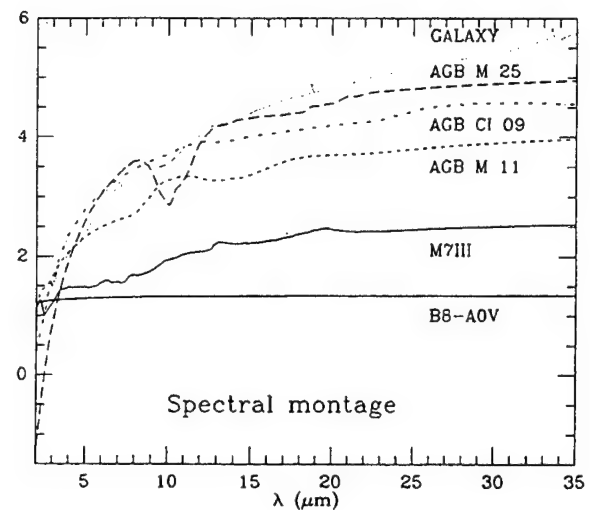


FIG. 3. Montage of intrinsic templates.

NGC 7027; L, He 2–131; H, Hb 5 and IC 2621; X, NGC 6302; E, NGC 7026. I represent the "PN RED" category by:  $[0.076 \times \text{NGC 6572} + 0.31 \times \text{IC 4997} + 0.076 \times \text{NGC 7027} + 0.076 \times \text{IC 418} + 0.063 \times \text{He 2–131} + 0.143 \times \text{Hb 5} + 0.143 \times \text{IC 2621} + 0.026 \times \text{NGC 6302} + 0.088 \times \text{NGC 7026}]$ , to embody the actual frequencies of occurrence of the archetypes.

IC 4997 and NGC 7026 lack spectra outside the LRS range so I used the two-blackbody method (see above, for extreme AGB stars) to fit the photometry and LRS, and modified the near-infrared continua to follow a free-free slope based on the radio continuum fluxes.

These techniques created 88 separate templates (87 Galactic, and one extragalactic). Figure 3 illustrates six such templates.

### 3.8 Extragalactic Templates

Galaxies play only a minor role in the Model except at long wavelengths ( $25 \mu\text{m}$ ), very low flux levels, and high galactic latitudes [cf. WCVWS's Fig. 11(b)]. Only four types of galaxies are required by the Model ("blue normal" and "red normal" galaxies, Seyferts, and quasars). WCVWS adopted the same LRS signature for all galaxies, but they tilted this to match the different [12]–[25] indices for the four galaxy types. Although not strictly accurate (only 31% of "active galaxies"—Seyferts of types 1 and 2, LINERS, or quasars—have the emission bands; the remaining 69% present power law spectra (Aitken & Roche 1985; Roche *et al.* 1984)), this suffices for current purposes (because the Model still excludes evolution, though it includes cosmology).

For the new version of the Model, the basic galaxy template is the average of those for M82, NGC 1068, and NGC 253. This is then tilted appropriately to yield separate templates for the four extragalactic categories.

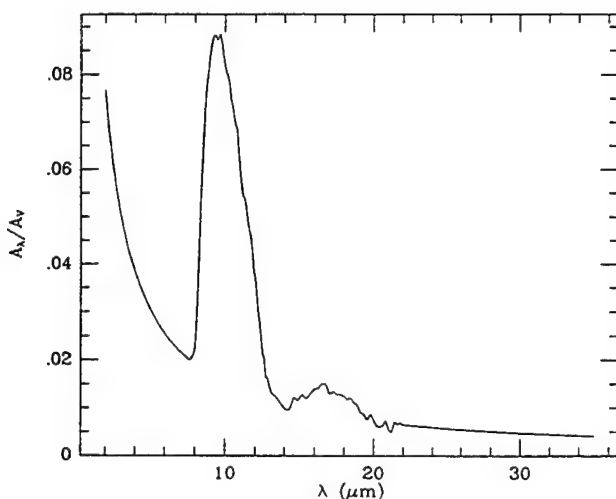


FIG. 2. The complete extinction curve from 2–35  $\mu\text{m}$  with its interstellar silicate features near 10 and 20  $\mu\text{m}$ , van der Hulst #15 extrapolation between 2.0 and 7.67  $\mu\text{m}$ , and  $\lambda^{-1}$  extrapolated component (that underlies the silicate features too) beyond 22.7  $\mu\text{m}$ .



### 3.9 Filling in Unobserved Photospheric Features

Intrinsic templates may finally require treatment for unobserved spectral regions. For example, if a category is represented by three separate sources only one of which has a 5–8  $\mu\text{m}$  airborne spectrum, I spliced this portion of the smoothed template of that particular source into the average template for the category.

Sources often lacked the 2.5–2.9 and 4.0–5.2  $\mu\text{m}$  portions of a spectrum, dominated by CO in cool stars. However, Arnaud *et al.* (1989) have published low-resolution 2.0–2.5  $\mu\text{m}$  spectra for a wealth of cool stars, both dwarfs and giants. I incorporated these first overtone fragments, normalized to overlap the adjoining continua, into the final average templates.

For the CO fundamental, far fewer spectra exist. Some are unpublished by Strecker, others by Bregman. These latter are contemporaneous 1.2–2.4, 3.0–4.2, and 4.4–5.6  $\mu\text{m}$  measurements of K and M giants ( $\alpha$  Aur G5 III+G0 III;  $\delta$  And K3 III;  $\alpha$  Tau K5 III; 2 Peg M1 III; HR 8621 M4 III; EU Del M6 III; TX Cam M10; U Ori OH/IR Mira). These constitute an incomplete but extremely valuable set of normalized fragments spanning the CO fundamental. I supplied the 5  $\mu\text{m}$  band for missing spectral types by interpolating between adjacent types.

I also accommodated newly obtained airborne spectra of relevant types, e.g., a 2.4–8.0  $\mu\text{m}$  high-resolution spectrum of the extreme AGB M star GL 1686 from a 1990 April KAO deployment in New Zealand). This shows no CO fundamental, perhaps due to shrouding by circumstellar dust emission. This provides support for a smooth featureless interpolation across the 4.7  $\mu\text{m}$  region in other (especially extreme) AGB M stars. Featureless interpolations are justified in extreme carbon stars by the generally blackbody-like nature of their infrared continua in which even the 3.1  $\mu\text{m}$  polyatomic feature is absent or very weak. I used unpublished 4–8  $\mu\text{m}$  KAO spectra of UU Aur (AGB C 03) to represent this unobserved region in R Lep (AGB C 03) and S Cep (AGB C 05). Other valuable new KAO 5–8  $\mu\text{m}$  spectra were of R LMi and  $\alpha^1$  Her taken in 1990 April. R LMi is an AGB M 07 so I inserted its KAO fragment in TX Cam and RS Cnc (AGB M 05) after rescaling.  $\alpha^1$  Her was substituted for the “M3–4 I–II” category.

### 3.10 “Missing” Categories

Even with such a large spectral database, some rare categories were still unrepresented. For AGB M 21 and 25, only OH/IR stars with either no, or only near-infrared, fragments could be found. So AGB M 21 was represented by the average of AGB M 19 and 23, for which good spectral coverage was obtained. AGB C 13, 15, and 17 were generated from the Model’s average LRS spectra for these categories (WCVWS) and the interpolated photometry (3.6). AGB C 21, 23, and 25 were taken to have the same template as that for AGB C 19 (cf. WCVWS). No example of a confirmed extreme AGB C or CI star has been discovered with  $[12] - [25] > 2.00$ , in spite of concerted

systematic attacks on the complete LRS database (Volk & Cohen 1989b; Volk *et al.* 1991, 1990) so I took the spectrum for AGB CI 19 to represent all categories from AGB CI 21 to 31. AGB CI 11 is taken to be the average of AGB CI 09 and 13.

## 4. OTHER CHANGES IN THE NEW MODEL

The actual code used to calculate the numbers and brightnesses of sources along the line-of-sight was maintained exactly as described by WCVWS, nor have I introduced changes in the tables of  $M_{12}$  and  $M_{25}$ . Therefore, the mid-infrared validation of the Model described by WCVWS still pertains to the new Model.

### 4.1 Surface Brightness Algorithm

Two code modifications were introduced. An algorithm was incorporated to calculate the cumulative surface brightness from the differential ( $\log N$ ,  $\log S$ ) table, corresponding simply to smearing the observed point sources over the area sampled (output is  $\text{W m}^{-2} \text{deg}^{-2}$ ). These brightnesses have been compared directly with the maps of the Galactic Plane at 2.4 and 3.4  $\mu\text{m}$  summarized by Okuda (1981: his Table I). The new Model does not violate any constraints imposed by these maps. However, such comparisons do not strictly constitute a validation of the new Model which deals only with the content of the point source sky while the rocket and balloon experiments near 2.4  $\mu\text{m}$  utilize large beams, sensitive to diffuse radiation as well as point sources.

### 4.2 Absolute Near-Infrared Magnitudes

WCVWS were primarily concerned with the LRS spectral range. Therefore, although they were able to demonstrate reasonable matches of their Model to 2  $\mu\text{m}$  source counts, their inherent table of absolute  $K$  magnitudes ( $M_K$ ) was not validated by explicit spectra. Using the new complete spectral library, I carefully examined the  $M_K$  table, integrating the original Johnson (1965: his Appendix Table A-2)  $K$  filter over the 87 Galactic templates (allowing for a slight extrapolation of the spectra below 2.0  $\mu\text{m}$  to accommodate the onset of the  $K$  filter). I compared the resulting  $M_K$ s with those derived from values of intrinsic  $K$ -[12] gleaned from the literature for the individual sources generating the new templates. These two sets of  $M_K$  were combined into a new table that differs slightly from that of WCVWS. I also created a Gaussian filter to represent the Japanese experiments at 2.4  $\mu\text{m}$  (effective wavelength 2.38, FWHM 0.09  $\mu\text{m}$ : cf., Hayakawa *et al.* 1981; Maihara *et al.* 1978). Integration of this Gaussian over the 87 templates yielded a new table for  $M_{2.4}$ . Because short wavelength magnitude tables are constructed from colors such as  $(B-V)$ ,  $(V-J)$ ,  $(J-H)$ , etc., the new Model also differs from WCVWS in  $M_B$ ,  $M_V$ ,  $M_J$ ,  $M_H$ , and  $M_K$ .

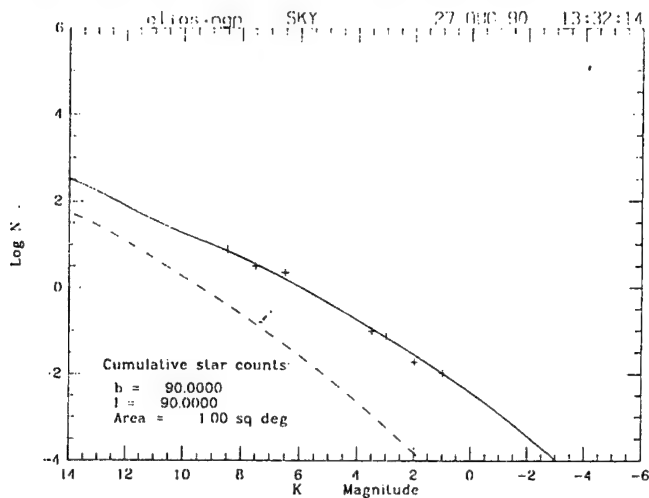


FIG. 4. Model predictions for  $(\log N, \log S)$  cumulative source counts. The different components in the model are represented as follows: total of all contributors, solid line; dots, disk; short dash, bulge; long dash, spiral arms; dot-short dash, molecular ring; dot-long dash, halo; short dash-long dash, external galaxies. Predictions for the north galactic pole compared with Elias (1978) actual counts (observational counts are represented by crosses).

Even when new absolute magnitude tables differ from the old, their effects on luminosity functions are minimal. I recreated the  $V$  and  $K$  luminosity functions and found them virtually indistinguishable from those of WCVWS, no doubt because the principal alterations in absolute magnitudes are for categories with extremely red spectra and very low population densities. However, the new tables are preferable because they provide consistency between the two modes of application of the Model; i.e., one now predicts basically identical source counts whether using the "hard-wired"  $K$  and  $[2.4]$  options or using the "customized" version in which an arbitrary filter profile may be introduced and carried through the modeling. (This short wavelength consistency was not required by WCVWS.)

##### 5. VALIDATIONS OF THE NEW MODEL

The wavelength at which most point source counts relevant to the new Model have been carried out is  $2.2 \mu\text{m}$ . I have, therefore, compared the  $K$  predictions of the new Model with: the north Galactic polar counts of Elias (1978); source counts in the Galactic plane in all seven zones of Eaton *et al.* (1984); and all four of the six zones

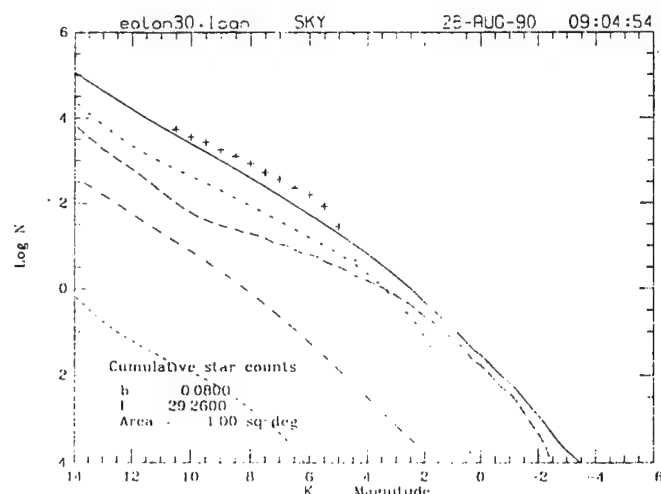
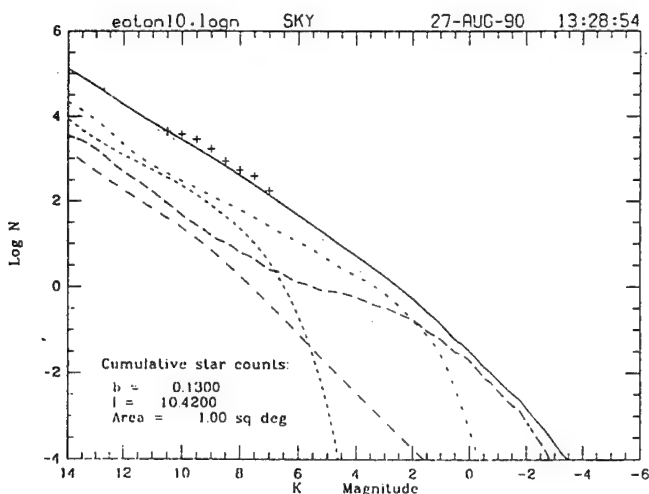
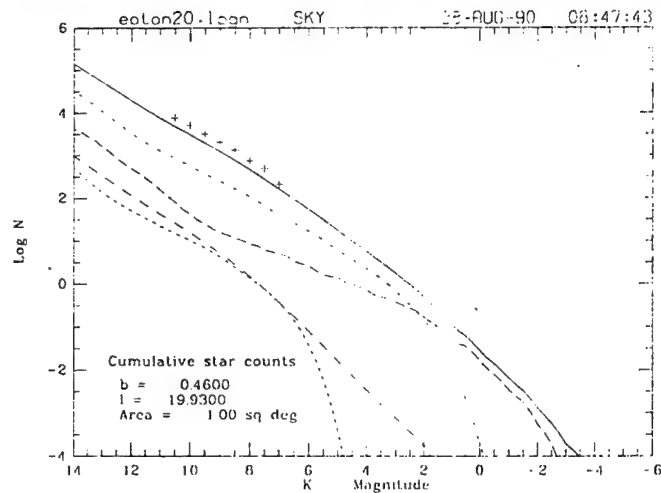
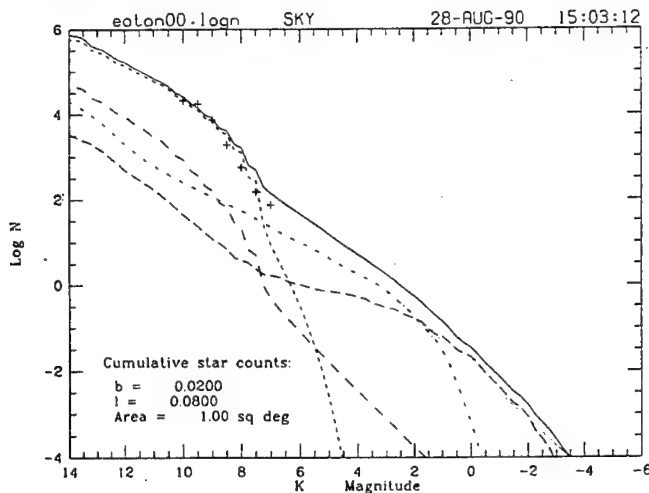


FIG. 5. As in Fig. 4 but for the seven small areas in the Galactic plane studied by Eaton *et al.* (1984): (a)  $l=0.08^\circ$ ,  $b=0.02^\circ$ ; (b)  $l=10.42^\circ$ ,  $b=0.13^\circ$ ; (c)  $l=19.93^\circ$ ,  $b=0.46^\circ$ ; (d)  $l=29.26^\circ$ ,  $b=0.08^\circ$ ; (e)  $l=39.96^\circ$ ,  $b=0.07^\circ$ ; (f)  $l=49.68^\circ$ ,  $b=0.16^\circ$ ; (g)  $l=59.70^\circ$ ,  $b=0.09^\circ$ .



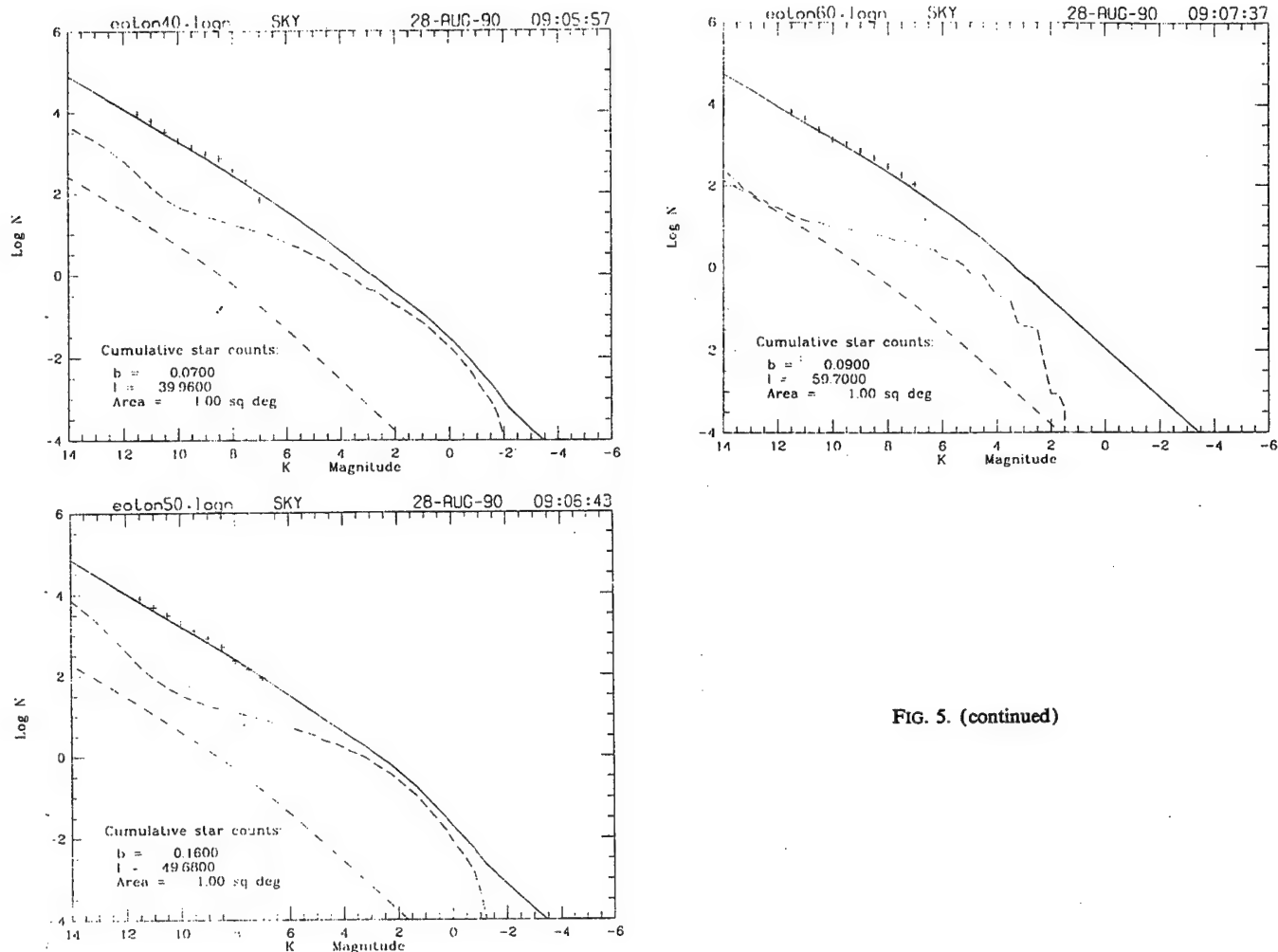


FIG. 5. (continued)

in the plane measured by Kawara *et al.* (1982) that represent contiguous areas. (Note that Eaton *et al.* give cumulative counts per square degree while Kawara *et al.* represent total cumulative counts for each zone, where zone areas vary between 3.2 and 48.0 square degrees.) Figures 4–6 present these 12 comparisons.

The Model does as well as WCVWS in the Eaton *et al.* regions, that is, it matches very well except near  $l=29^\circ$ , where it falls short of observations by a factor of 2 at the brightest magnitudes, and at the Center, where the brightest bulge stars are somewhat overpredicted. The comparisons with the Kawara *et al.* counts show the same behavior. These discrepancies could arise either because the Model's circular molecular ring is inappropriate, or because the extinction is treated too simply (without any real clumpiness). At the north Galactic pole, the agreement with Elias's counts is excellent.

These observations do not indicate any major discrepancies between the Model's predictions and actual counts.

## 6. CONCLUSIONS

The newest version of the Point Source Infrared Sky Model performs identically to WCVWS at 2.2, 12, 25  $\mu\text{m}$ . It accommodates all filters whose transmission curves extend from zero to zero wholly within the 2.0 to 35.0  $\mu\text{m}$

range, with consistency between tables of broadband absolute magnitudes and those derived by integration of actual filter/system efficiency profiles over the real spectra. It also yields estimates of the surface brightness of the point sources smeared across the desired area, as a function of threshold sensitivity. These capabilities make the Model an ideal tool for predicting, and interpreting, source counts and the general appearance of the infrared sky, and for seeking potential cosmic backgrounds in the infrared regime, using future satellites (COBE, ISO, SIRTf) or for ground-based near-infrared surveys (2MASS, DENIS).

Finally, I detail some enhancements projected even for the current Model. Recently, the issue of infrared broadband and continuous spectral calibration has been reexamined in detail (Cohen *et al.* 1992a; Cohen *et al.* 1992; Cohen *et al.* 1992b). These papers demonstrate the manner in which previous infrared spectra in the literature have been warped systematically due to the widespread dependence on Planck functions to represent the photospheric spectra of normal K and M giant "calibrators." The primary effects are incorrect continuous slopes and spurious "emission" features between 7.5 and  $\sim 12 \mu\text{m}$  due to neglect of the fundamental band of SiO in absorption in these giants. These effects lead to 10%–25% errors in the shape of "calibrated" infrared spectra and are present in some of the current Model library spectra. The statistical character of

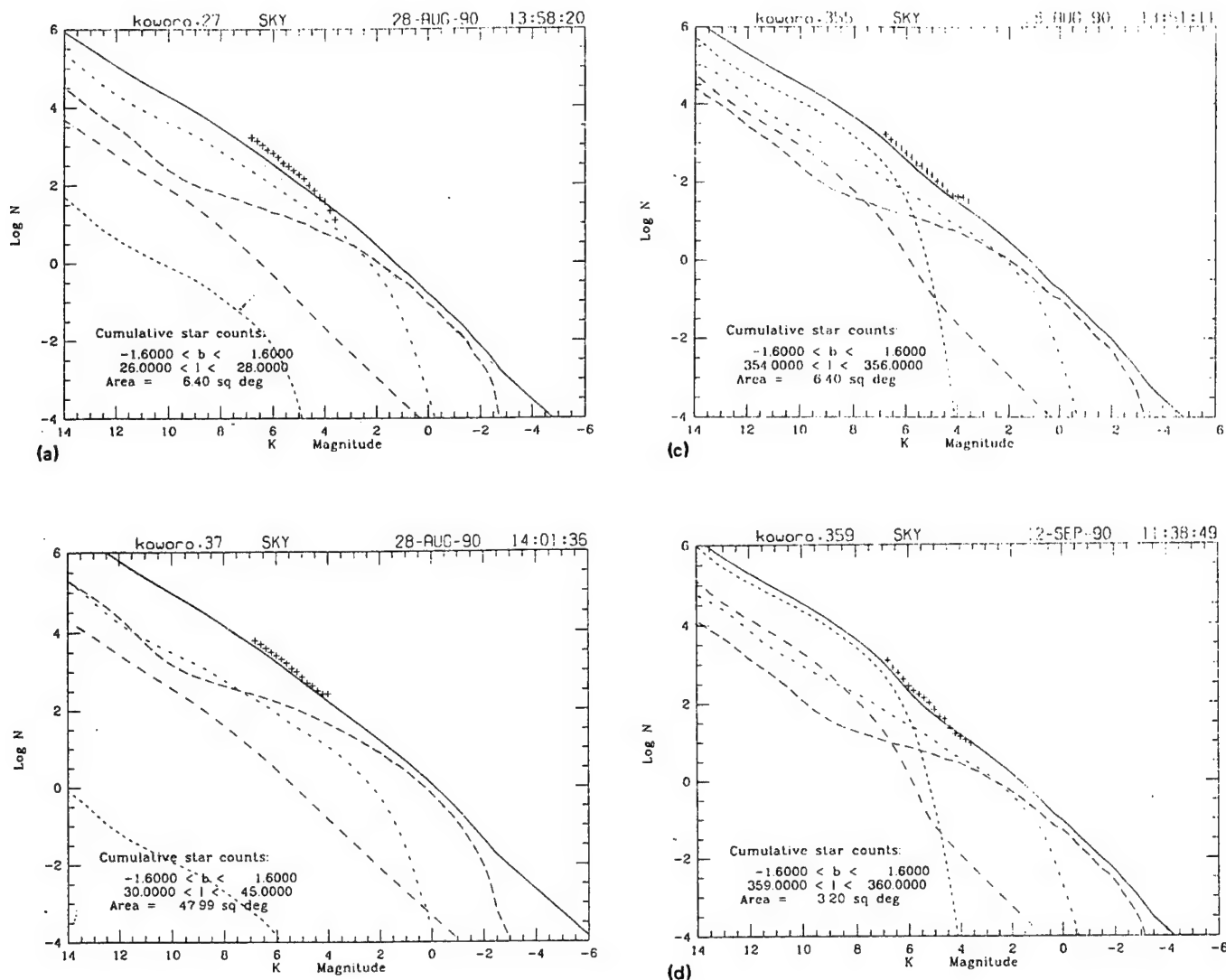


FIG. 6. As in Fig. 5 but for the Galactic plane zones observed by Kawara *et al.* (1982); the four zones involving contiguous areas are shown (crosses represent the observed cumulative counts). (a) For the zone near 27° longitude, the Model was run in its “integrate over area” mode, gridding the latitude range uniformly with step 0.8°, and longitude with step 0.5° (i.e., the sum of 16 separate calculations). (b) The zone centered near  $l=37^\circ$  was gridded in latitude by 0.8° and longitude by 5° (i.e., the sum of 12 calculated rays). (c) The zone centered on  $l=355^\circ$  was similarly the sum of 16 calculated rays (steps in latitude and longitude of 0.8° and 0.5°, respectively). (d) The zone centered on  $l=359^\circ$  was the sum of 16 rays with steps of 0.4° and 0.5°, respectively.

the Model and its typical application to relatively broad bandpass filters render the predictions quite robust in the face of such shape errors. However, I hope to reconstruct the spectral library using only infrared spectra of known calibration pedigree traceable to some fundamental “standard spectrum” such as that of Sirius (Cohen *et al.* 1992a). Likewise, the future spectral library will take advantage of new models for the atmospheres of cool dwarf stars. These latter improvements affect only the library spectra of normal stars and so have minimal consequences for typical Model predictions. More significant improvements might be anticipated if the present smooth characterization of interstellar extinction could be replaced by one incorporating the real clumpiness in the galactic plane. For example, Kent *et al.* (1991) have analyzed near-infrared surface brightness measurements made during the Spacelab 2 mission using a model for the distribution of

interstellar dust that is based upon interpretation of CO and HI observations. It should be possible to combine this kind of realistic extinction picture with the geometric and spectral detail inherent in the current Model.

I thank Fred Witteborn and Jesse Bregman at NASA-Ames for giving me access to their copious infrared spectral database; Don Strecker for valuable discussions and for his original set of unpublished KAO spectra; Bill Glaccum for sending me many of his dissertation spectra from the KAO; and Amara Graps for valuable assistance in establishing the scanner software on an Ames MAC SE. I am grateful to Richard Wainscoat for vital input on the modifications made to the original Sky Model code. This work was supported by Dr. S. D. Price at the Phillips Laboratory under Contract No. F19628-89-C-0116 with Jamieson Science & Engineering, Inc.

## REFERENCES

- Aitken, D. K., & Roche, P. F. 1982, *MNRAS*, 200, 217  
 Aitken, D. K., & Roche, P. F. 1985, *MNRAS*, 213, 777  
 Aitken, D. K., Roche, P. F., & Allen, D. A. 1982, *MNRAS*, 200, 6P  
 Arnaud, K. A., Gilmore, G., & Collier-Cameron, A. 1989, *MNRAS*, 237, 495  
 Ashley, M. C. B., & Hyland, A. R. 1988, *ApJ*, 331, 532  
 Berriman, G., and Reid, N. 1987, *MNRAS*, 227, 315  
 Bregman, J. 1990, private communication  
 Cohen, M. 1975, *MNRAS*, 173, 279  
 Cohen, M. 1980, *MNRAS*, 191, 499  
 Cohen, M. 1984, *MNRAS*, 206, 137  
 Cohen, M., Allamandola, L. J., Tielens, A. G. G. M., Bregman, J., Simpson, J. P., Witteborn, F. C., Wooden, D., & Rank, D. 1986, *ApJ*, 302, 737  
 Cohen, M., Tielens, A. G. G. M., Bregman, J. D., Witteborn, F. C., Rank, D. M., Allamandola, L. J., Wooden, D. H., & de Muizon, M. 1989, *ApJ*, 341, 246  
 Cohen, M., & Volk, K. 1989, *AJ*, 98, 1563  
 Cohen, M., Walker, R. G., & Witteborn, F. C. 1992, *AJ*, 104, 2030 (CWW)  
 Cohen, M., Walker, R. G., Barlow, M. J., & Deacon, J. R. 1992a, *AJ*, 104, 1650  
 Cohen, M., & Witteborn, F. C. 1985, *ApJ*, 294, 345  
 Cohen, M., Witteborn, F. C., Carbon, D. F., Augason, G. C., Wooden, D. H., Bregman, J., & Goorvitch, D. 1992b, *AJ*, 104, 2045  
 Cutri, R. M., *et al.* 1981, *ApJ*, 245, 818  
 Eaton, N., Adams, D. J., & Giles, A. B. 1984, *MNRAS*, 208, 241  
 Eiroa, C., Hefele, H., & Zhang-Yu, Q. 1983, *A&AS*, 54, 309  
 Eiroa, C., Neckel, Th., Sanchez Magro, C., & Selby, M. J. 1981, *A&A*, 95, 206  
 Elias, J. H. 1978, *AJ*, 83, 791  
 Forrest, W. J., *et al.* 1978, *ApJ*, 219, 114  
 Forrest, W. J., McCarthy, J. F., & Houck, J. R. 1979, *ApJ*, 233, 611  
 Forrest, W. J., Houck, J. R., & McCarthy, J. F. 1981, *ApJ*, 248, 195  
 Gehrz, R. D., Kleinmann, S. G., Mason, S., Hackwell, J. A., & Grasdalen, G. L. 1985, *ApJ*, 290, 296  
 Giguere, P. T., Woolf, N. J., & Webber, J. C. 1976, *ApJ*, 207, L195  
 Glaccum, W. 1990, Ph.D. dissertation, University of Chicago  
 Goebel, J. H., Bregman, J. D., Strecker, D. W., Witteborn, F. C., & Erickson, E. F. 1978, *ApJ*, 222, L129  
 Goebel, J. H., & Moseley, S. H. 1985, *ApJ*, 290, L35  
 Hacking, P., & Houck, J. R. 1987, *ApJS*, 63, 311  
 Hayakawa, S., Matsumoto, T., Murakami, H., Uyama, K., Thomas, J. A., & Yamigami, T. 1981, *A&A*, 100, 116  
 Houck, J. R., Forrest, W. J., & McCarthy, J. F. 1980, *ApJ*, 242, L265  
 Houck, J. R., Shure, M. A., Gull, G. E., & Herter, T. 1984, *ApJ*, 287, L11  
 Hyland, A. R., Becklin, E. E., Frogel, J. A., & Neugebauer, G. 1972, *A&A*, 16, 204  
 IRAS Catalogs and Atlases, Vol. 1, Explanatory Supplement 1988, edited by C. A. Beichman, G. Neugebauer, H. Habing, P. E. Clegg, and T. J. Chester (GPO, Washington, DC)  
 IRAS Catalogs and Atlases, Vols. 2-6, The Point Source Catalog. 1988, edited by C. A. Beichman, G. Neugebauer, H. Habing, P. E. Clegg, and T. J. Chester (GPO, Washington, DC) (PSC2)  
 IRAS Catalogs and Atlases, Atlas of Low Resolution Spectra, 1986, IRAS Science Team, *A&AS*, 65, 607  
 Isaacman, R. 1984, *A&A*, 130, 151  
 Johnson, H. L. 1965, *ApJ*, 141, 923  
 Jones, B., Merrill, K. M., Puetter, C. R., & Willner, S. P. 1978, *AJ*, 83, 1437  
 Jones, T. J., Hyland, A. R., Fix, J. D., & Cobb, M. L. 1988, *AJ*, 95, 158  
 Kawara, K., Kozasa, T., Sato, S., Kobayashi, Y., Okuda, H., & Jugaku, J. 1982, *PASJ*, 34, 389  
 Kent, S. M., Dame, T. M., & Fazio, G. 1991, *ApJ*, 378, 131  
 Knacke, R. F., Puetter, R. C., Erickson, E. F., & McCorkle, S. 1985, *AJ*, 90, 1828  
 Magazzu, A., & Strazzulla, G. 1989, in *Infrared Spectroscopy in Astronomy*, Proc. 22nd ESLAB Symposium, edited by B. H. Kaldeich, ESA SP-290, p. 371  
 Maihara, T., Oda, N., Sugiyama, T., & Okuda, H. 1978, *PASJ*, 30, 1  
 McCarthy, J. F., Forrest, W. J., & Houck, J. R. 1978, *ApJ*, 224, 109  
 Merrill, K. M., & Stein, W. A. 1976a, *PASP*, 88, 285  
 Merrill, K. M., & Stein, W. A. 1976b, *PASP*, 88, 294  
 Merrill, K. M., & Stein, W. A. 1976c, *PASP*, 88, 874  
 Noguchi, K., Maihara, T., Okuda, H., Sato, S., & Mukai, T. 1977, *PASJ*, 29, 511  
 Okuda, H. 1981, in *Infrared Astronomy*, IAU Symposium No. 96, edited by C. G. Wynn-Williams and D. P. Cruikshank (Reidel, Holland), p. 247  
 Puetter, R. C., Russell, R. W., Sellgren, K., & Soifer, B. T. 1977, *PASP*, 89, 320  
 Ridgway, S. T., Joyce, R. R., White, N. M., & Wing, R. F. 1980, *ApJ*, 235, 126  
 Roche, P. F., & Aitken, D. K. 1986, *MNRAS*, 221, 63  
 Roche, P. F., Aitken, D. K., Phillips, M. M., & Whitmore, B. 1984, *MNRAS*, 207, 35  
 Russell, R. W., Soifer, B. T., & Merrill, K. M. 1977, *ApJ*, 213, 66  
 Russell, R. W., Soifer, B. T., Willner, S. P. 1977, *ApJ*, 220, L49  
 Russell, R. W., Soifer, B. T., & Willner, S. P. 1978, *ApJ*, 220, 568  
 Scargle, J., & Strecker, D. W. 1979, *ApJ*, 228, 838  
 Sellgren, K. 1986, *ApJ*, 305, 399  
 Sellgren, K., Allamandola, L. J., Bregman, J. D., Werner, M. W., & Wooden, D. H. 1985, *ApJ*, 299, 416  
 Strecker, D. W. 1990, private communication  
 Strecker, D. W., Erickson, E. F., & Witteborn, F. C. 1978, *AJ*, 83, 26  
 Strecker, D. W., Erickson, E. F., & Witteborn, F. C. 1979, *ApJS*, 41, 501  
 Volk, K., & Cohen, M. 1989a, *AJ*, 98, 1918  
 Volk, K., & Cohen, M. 1989b, *AJ*, 98, 931  
 Volk, K., & Cohen, M. 1990, *AJ*, 100, 485  
 Volk, K., Stencel, R. E., Brugel, E. W., & Kwok, S. 1990, *Supplementary IRAS LRS Spectra of 1810 Sources Brighter than 10 Jy not included in the LRS Atlas*, preprint  
 Volk, K., Stencel, R. E., Brugel, E. W., & Kwok, S. 1991, *ApJS*, 77, 607  
 Wainscoat, R. J., Cohen, M., Volk, K., Walker, H. J., & Schwartz, D. E. 1992, *ApJS*, 83, 111 (WCVWS)  
 Walker, R. G., & Cohen, M. 1989, *Contractor's Final Report to Boeing Aerospace (CZ 1521)*  
 Willner, S. P., *et al.* 1982, *ApJ*, 253, 174  
 Willner, S. P., Jones, B., Puetter, R. C., Russell, R. W., & Soifer, B. T. 1979, *ApJ*, 234, 496  
 Willner, S. P., Soifer, B. T., Russell, R. W., Joyce, R. R., & Gillett, F. C. 1977, *ApJ*, 217, L121  
 Witteborn, F. C. 1990, private communication  
 Witteborn, F. C., Strecker, D. W., Erickson, E. F., Smith, S. M., Goebel, J. H., & Taylor, B. J. 1980, *ApJ*, 238, 577

# POWERFUL MODEL FOR THE POINT SOURCE SKY: FAR-ULTRAVIOLET AND ENHANCED MIDINFRARED PERFORMANCE

MARTIN COHEN

Jamieson Science & Engineering, Inc., 5321 Scotts Valley Drive, Suite 204, Scotts Valley, California 95066 and  
Radio Astronomy Laboratory, 601 Campbell Hall, University of California, Berkeley, California 94720  
Electronic mail: cohen@bkyast.berkeley.edu

Received 1993 July 14

## ABSTRACT

I report further developments of the Wainscoat *et al.* [ApJS, 83, 111 (1992)] model originally created for the point source infrared sky. The already detailed and realistic representation of the Galaxy (disk, spiral arms and local spur, molecular ring, bulge, spheroid) has been improved, guided by CO surveys of local molecular clouds, and by the inclusion of a component to represent Gould's Belt. The newest version of the model is very well validated by *IRAS* source counts. A major new aspect is the extension of the same model down to the far ultraviolet. I compare predicted and observed far-ultraviolet source counts from the Apollo 16 "S201" experiment (1400Å) and the *TD1* satellite (for the 1565Å band).

## 1. INTRODUCTION

The basic model (SKY) is described by Wainscoat *et al.* (1992, hereafter referred to as WCVWS). It was originally designed to provide predictions for midinfrared point source counts. However, the guiding philosophy was *not* to produce a model specific to the infrared, but rather one that stressed geometric realism and accuracy of physical attributes of stars and nonstellar pointlike objects over a very broad range of wavelengths. SKY's wavelength capabilities are of two kinds. It operates with a number of broadband "hardwired" filters: standard Johnson *B, V, J, H, K*; the Japanese narrow-band balloon bandpass at 2.4  $\mu\text{m}$ ; and *IRAS* [12] and [25]. It can also customize its predictions for specific filters because its code draws upon an embedded complete library of continuous infrared spectra for all categories of source. WCVWS provided a library based on the *IRAS* Low Resolution Spectrometer ( $\lambda\lambda 7.7$ – $22.7 \mu\text{m}$ ). Cohen (1993) extended this spectrally continuous library to handle any filter whose full width at zero intensity bandpass lies strictly within the 2.0–35.0  $\mu\text{m}$  range. This provides the flexibility to make predictions for the present generation of infrared satellites (e.g., *COBE/DIRBE*) and the next (e.g., *ISO*).

The purpose of the present paper is twofold: first, to report a significant improvement in the realism of midinfrared sky simulations; and second, to demonstrate that the same model, with some specific modifications, also operates satisfactorily in the far-ultraviolet domain.

## 2. IMPROVED GEOMETRY FOR THE SPIRAL LOCAL SPURS

SKY incorporates five fully detailed Galactic components: an exponential disk; a Bahcall-type bulge; a de Vaucouleurs halo; a four-armed spiral and a local spur; and a circular molecular ring. Each geometrical element may contain up to 87 categories of source based upon detailed analyses of the content of the *IRAS* sky (Walker *et al.* 1989). These comprise 33 normal stellar types; 42 types of

AGB star, both oxygen and carbon rich; six types of object that are distinct from others only by their midinfrared high luminosity; and six types of exotica including T Tau stars, H II regions, planetaries, and reflection nebulae. Every category of source has its own set of absolute magnitudes in the hardwired passbands; its own dispersion in  $M_{12}$ ; its own individual scale height and volume density in the local solar neighborhood. In addition, some sources may be absent from specific geometrical components (the arms and ring are made rich in high-mass stars; the halo deficient in these). SKY also accommodates external galaxies, through their *IRAS* luminosity functions, but only for wavelengths beyond 5  $\mu\text{m}$ , where their pointlike character is assured.

These many attributes, all drawn from the astronomical literature, are entirely equivalent to the customary *V* and *K* luminosity functions (WCVWS). But this tabular approach facilitates augmentation of the content of the model sky by adding other populations, or updating of physical parameters as these become better known from independent studies.

Cohen (1993) did not modify the geometry inherent in WCVWS. However, careful examination of the discrepancies between the 12 and 25  $\mu\text{m}$  sky as predicted by SKY and that observed by *IRAS* [Figs. 8(a)–8(d) of WCVWS] suggests potential improvements. First is to simulate the local spur better. The Sun essentially lies in a H I "valley" between two ridges. Not only is there a piece of the local spur toward the anticenter direction, there is a second ridge toward the center, WCVWS and Cohen (1993) already incorporate the spur toward the anticenter. I have now added that toward the center, mimicking the longitude confines of the original spur but closer to the center (winding constant,  $a=4.57$ ; starting galactocentric distance,  $R_{\text{min}}=7.591 \text{ kpc}$ ; starting angle,  $\theta_{\text{min}}=5.847 \text{ radians}$ ; angular extent=0.55 radians). However, to simulate the H I distribution even more realistically than did WCVWS, I have represented the spurs as having lesser width than the 750 pc of the four-armed spiral. In fact, I used only 300 pc width for the two spurs. This is consistent

with the distribution of local molecular clouds (Dame *et al.* 1987) and OB associations (Blauuw 1991).

It is likely that the local molecular clouds that delineate these spurs include significant embedded populations, detectable in the midinfrared but heavily obscured in the optical. Consequently, I have chosen to enhance the stellar populations of both the disk and spiral arm components where the line of sight is strictly within the local spurs (i.e., where the absolute magnitude of the difference between the local galactocentric radius and either of the two spiral segments that represent the spurs is less than their halfwidth of 150 pc). I have used simultaneous comparisons between the predicted 12 and 25  $\mu\text{m}$  cumulative source counts and those observed by *IRAS* to determine the best local enhancements of disk and arm populations. The criterion for a satisfactory match of prediction and observation was always that deviations in  $(\log N, \log S)$  occur only where Poisson statistics dominate the accuracy of the counts; i.e., for  $\log N$  below  $\sim 1.5$ . Within this framework, the two boosts were generally well determined. The extent of the clouds within which these local boosts to stellar population were applied was found to follow Table 2 of Dame *et al.* closely for the first and second quadrants. By the third and fourth quadrants, interplay between local clouds and the more distant Carina arm complicates the geometry and it was no longer possible simply to follow Dame *et al.*'s table of the nearest clouds. However, CO emission is always associated with those directions in which the *IRAS* counts demand enhanced population densities and can be recognized from Fig. 6 of Dame *et al.* (1987). The entire *IRAS* sky in the range  $|l| > 40^\circ$ ,  $|b| < 20^\circ$  was examined exhaustively and detailed improvements made on the basis of the 12 and 25  $\mu\text{m}$  counts using the same grid of zones described by WCVWS.

Figures 1 and 2 illustrate typical improvements achieved by using the current (still-developing) version of the code as compared with version 1 of the model (WCVWS) at both 12 and 25  $\mu\text{m}$ . Figures 1(a) and 2(a) show the discrepancies between *IRAS* counts and those predicted by WCVWS. Note that the slopes of these disagreements can readily be recognized as that of the spiral arms' contribution rather than that of the disk. Figures 1(b) and 2(b) demonstrate the excellent matches between the new model and *IRAS* counts. Both these zones were represented by WCVWS as "black" in assessing the overall performance of version 1 of the model, i.e., zones where the cumulative discrepancies between *IRAS* counts and prediction exceeded a factor of 2. Now both are essentially perfectly matched ("clear" zones in Fig. 3 below).

I have also incorporated the weakening of the H I in the disk that is detectable to *IRAS* (see WCVWS) as regions where model predictions exceed observed counts. This chiefly affects the range  $205^\circ < l < 275^\circ$  for  $-2^\circ < b < 10^\circ$  although the latitude extent of this phenomenon is longitude dependent. The effect is typically a diminution of the associated stellar disk population to 60% of that expected, although in the area  $240^\circ < l < 250^\circ$  and  $-0.5^\circ < b < 2^\circ$ , the inferred residual population is a mere 10% of that expected from an ideal disk.

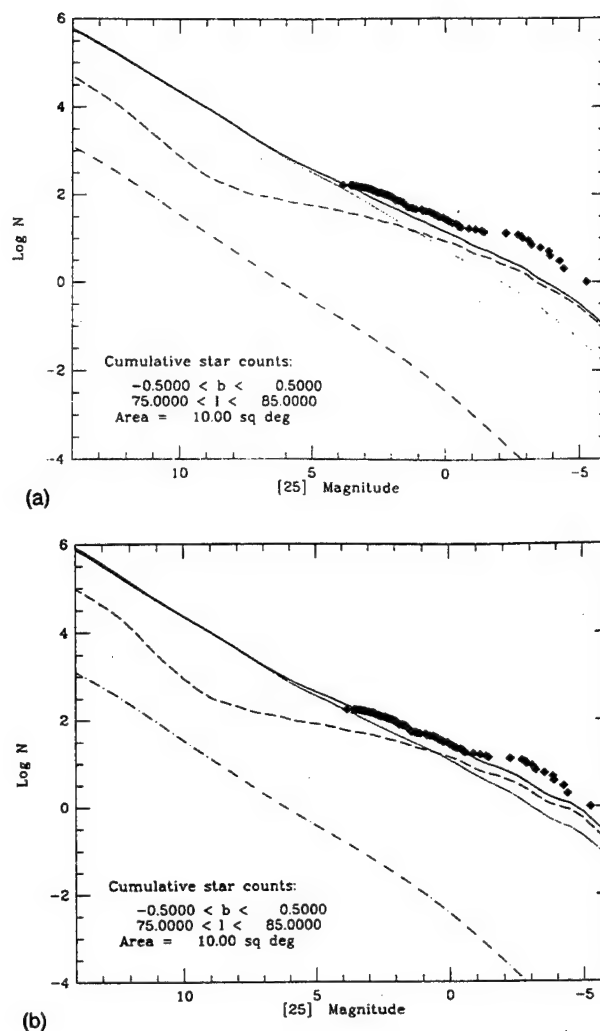


FIG. 1. Typical improvements achieved by the new model compared with WCVWS' first version. 25  $\mu\text{m}$  predictions for the zone  $-0.5 < b < 0.5$ ,  $75 < l < 85$ . Diamonds, observed counts; solid line, total model prediction; dots, disk; long dashes, spiral arms, spurs, and Gould's Belt; long dash-dot, halo. (a) WCVWS. (b) New model.

### 3. AN IMPROVED REPRESENTATION OF THE MIDINFRARED (*IRAS*) SKY

WCVWS compared the performance of SKY with observed *IRAS* point source counts at 12 and 25  $\mu\text{m}$  across the entire sky. They sampled 238 separate Galactic zones, finding 87% of these zones well predicted (within a factor of 1.5) at 12  $\mu\text{m}$  and 76% equally well predicted at 25  $\mu\text{m}$ . Nowhere did any discrepancies exceed a factor 3. This fidelity is quite remarkable because all the modeling in this first version of SKY was purely analytically expressed.

With the improved representation of the local spurs and the associated enhanced population densities in disk and arms, the 12  $\mu\text{m}$  skywide counts are now predicted almost perfectly, with only 6 zones (2.5%) discrepant by a factor as large as 1.5 [Figs. 3(a) and 3(c)]. The 25  $\mu\text{m}$  sky is also improved. A few problems remain near the galactic plane and toward the Orion OB association [Figs. 3(b) and 3(d)] but only 8% of the 238 zones are discrepant by  $\geq 1.5$ . Indeed, the quality of the new model makes it meaningful to consider those discrepancies that exceed a factor of only



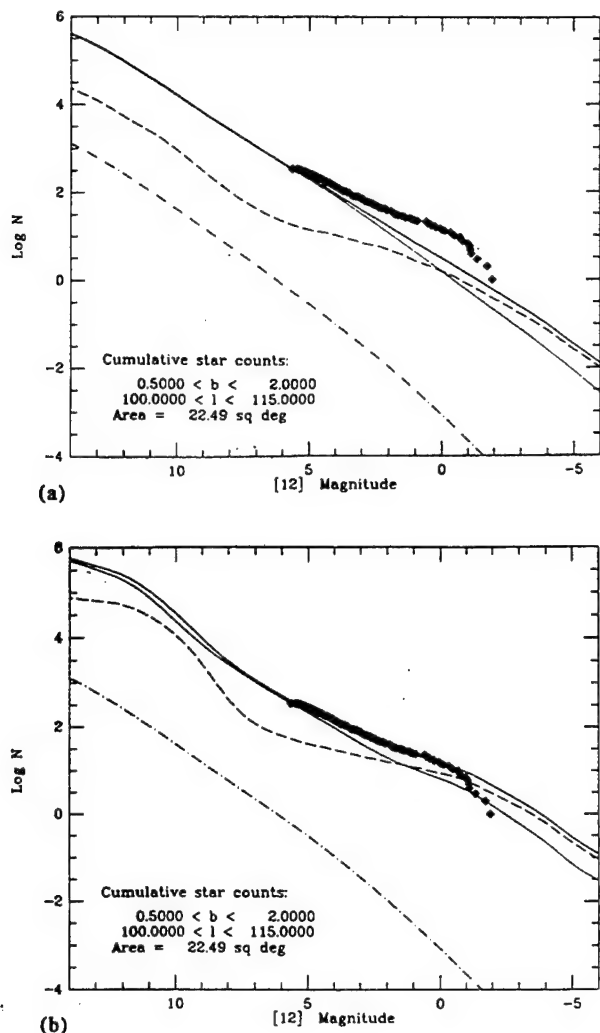


FIG. 2. As in Fig. 1 but for the zone  $0.5 < b < 2.0$ ,  $100 < l < 115$  at  $12 \mu\text{m}$ . (a) WCVWS. (b) New model.

1.3. With this threshold, 95% of the  $12 \mu\text{m}$  sky and 85% of the  $25 \mu\text{m}$  sky are well represented. These percentages do not include the handful of zones near the Galactic Center in which the new model (which defaults precisely to version 1 here) slightly overpredicts *IRAS* counts (within a factor of 1.3).

Note that although this resulting fourth version of the model seems to assess stellar populations accurately in the midinfrared, the extra extinction associated with these same molecular clouds is not yet included. Consequently, there is great merit in investigating the performance of the model at far-ultraviolet wavelengths where the potentially clumpy character of the extinction ought to dominate the counts in some directions close to the Galactic plane. In the near infrared, say at  $2 \mu\text{m}$ ,  $A_K/A_V \sim 0.09$  so that one might well expect the model's performance at  $K$  to go hand-in-hand with the improved capability to simulate the midinfrared sky. Indeed, as deeper or more extensive  $K$  surveys are performed, both at high latitudes (Wainscoat 1992) and in the plane (the "TMGS" of Garzon *et al.* 1993), SKY continues to perform extremely well, right into the inner Galaxy. However, the bulge representation is still that of WCVWS and one might consider a different

formalism (perhaps using a bar) for the innermost Galaxy both to address minor problems at  $12/25 \mu\text{m}$  and more serious but localized ones at  $K$  (near  $l \sim 20^\circ$  and  $30^\circ$ ). Those enhancements represent work in progress and are not described here.

#### 4. OPTICAL PERFORMANCE

WCVWS demonstrated the validity of their model at  $V$ , comparing it with data for the NGP assembled by Bahcall & Soneira (1984). A more difficult test of performance at  $B$  and  $V$  is illustrated by Terndrup's (1988) differential counts for Baade's Window [Figs. 4(a) and 4(b)]. His counts fall away from SKY's predictions essentially where he estimates his incompleteness to set in. While optical starcounts are certainly of interest, several programs of digitization of the new epoch plates of the NGS-Palomar Observatory Sky Survey are just beginning, while the University of Minnesota Automated Plate Scanner (Pennington *et al.* 1993) database of digitized first epoch Palomar plates will soon be publicly available. Therefore, I shall defer discussions on SKY's simulations of deep blue and red plate material to a future paper. For the moment, the far ultraviolet promises to provide a more substantial challenge to any sky model.

#### 5. FAR-ULTRAVIOLET CAPABILITIES

It is eventually intended that a future version of SKY will extend the flexibility to customize predictions to a user's passband (that now exists for the  $2.0\text{--}35.0 \mu\text{m}$  range: Cohen 1993) to the range  $0.12\text{--}35 \mu\text{m}$ . This will be accomplished by means of a complete far-ultraviolet to midinfrared spectral library exactly akin to that described by Cohen (1993) for version 3 of SKY. However, it is clearly desirable first to address the many questions relevant to the far-ultraviolet sky through use of hardwired broadband filters. Such questions include the following. (1) How well does the model's source table still represent the content of the far-ultraviolet sky? (2) How important are white dwarfs to a good far-ultraviolet sky simulation? (3) How necessary is it to include horizontal-branch stars in the far ultraviolet? (4) Do sufficient observations exist to provide the requisite broadband  $M_{\text{FUV}}$  tables to add such passbands to SKY? (5) Is the model's relatively simple analytic expression of interstellar extinction still adequate at low latitudes and at far-ultraviolet wavelengths where  $A_{\text{FUV}}/A_V$  is far greater than in the optical and near infrared? (6) Is SKY's geometry adequate for far-ultraviolet predictions; e.g., does the explicit absence of Gould's Belt pose any obvious problems (cf. Henry 1991)?

To provide any test of the far-ultraviolet capability of the model requires a database that contains either far-ultraviolet absolute magnitudes directly or (more commonly)  $[\text{UV}] - V$  color indices. Carnochan's (1982) detailed postflight analysis of the entire dataset from the *TD1* satellite (Boksenberg *et al.* 1973) established color indices for many types of normal star. Consequently, these provide a logical starting point not just for color indices but also for

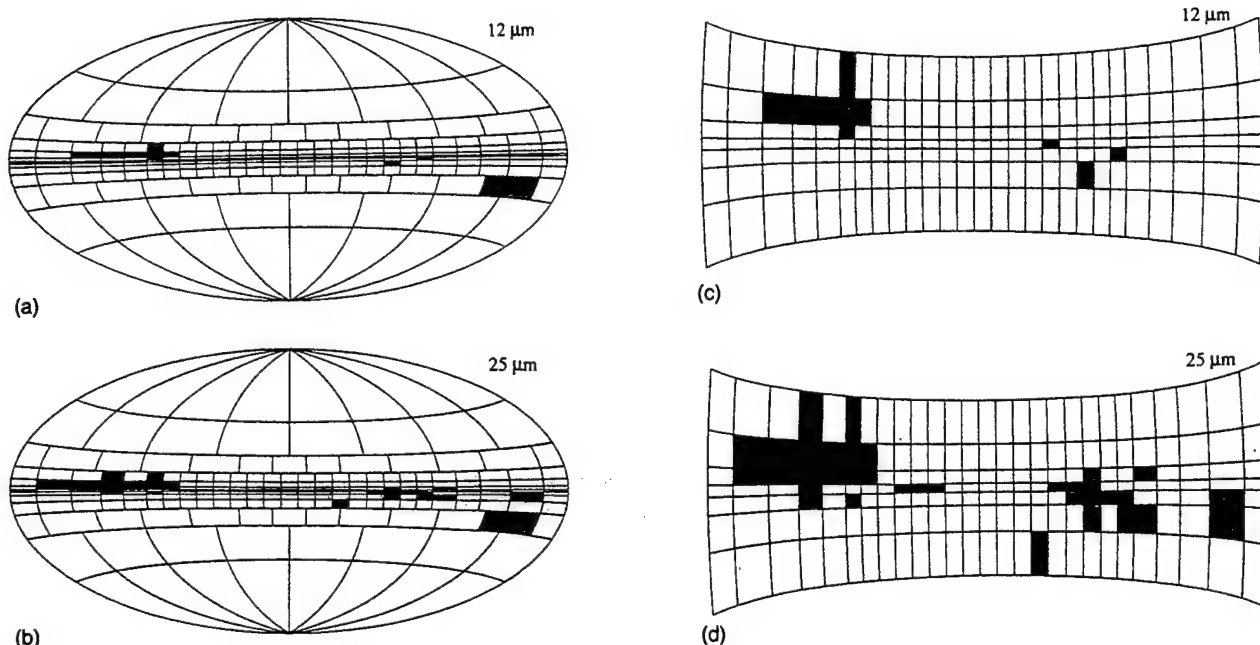


FIG. 3. All-sky comparison of the new model's predicted counts with the *IRAS Point Source Catalog* at 12 and 25  $\mu\text{m}$ . The Aitoff projection is identical to that used by WCVWS and shows the same 238 zones. The Galactic Center is at the center and longitude increases to the left. The lightest shading indicates regions in which the model prediction exceeds the observed cumulative counts by a factor of between 1.15 and 1.30. Midgray shading characterizes zones in which the observed cumulative counts exceed the model prediction by a factor  $> 1.3$  but  $< 2.0$ . Dark gray indicates that counts exceed prediction by a factor of  $> 2.0$  but  $< 3.1$ . Black indicates that counts exceed prediction by a factor of  $> 3.1$ . (a) 12  $\mu\text{m}$ . (b) 25  $\mu\text{m}$ . (c) Magnified view of the region  $|b| < 10^\circ$  at 12  $\mu\text{m}$ . (d) As in (c) but at 25  $\mu\text{m}$ . In all plots,  $l=0^\circ$  is at the center,  $l=180^\circ$  at the left edge.

the far-ultraviolet extinction in the *TDI* bands ( $A_{1565}/A_V=8.09$ ; see Table 1 of Carnochan 1982). The desire to go as far as possible into the far ultraviolet dictated the choice of the  $\lambda 1565$  passband to represent the *TDI* sky. Carnochan (1989) has noted the nonlinearity of *TDI*'s faint-end calibration so I excluded sources fainter than  $[1565]=8.8$  mag from consideration in matching star-counts. Further, Murthy (1992) has provided a copy of the enlarged *TDI*  $\lambda 1565$  database created by Landsman (1984; see, also, Henry *et al.* 1988), supplemented by all those stars originally discarded when multiple objects fell on the *TDI* detectors. This contains 58 012 stars.

I followed Carnochan's (1982) prescription for defining *TDI* far-ultraviolet magnitudes from in-band fluxes, including the correction to the newer scale set by reanalysis of the  $\eta$  UMa fluxes (Bohlin *et al.* 1980). Initially, I integrated the  $\lambda 1565$  passband over a wide variety of *IUE* spectra (Heck *et al.* 1984; Wu *et al.* 1991). However, there is a dearth of cool stars with adequate signal-to-noise short-wave *IUE* coverage from which to determine [far-ultraviolet]- $V$  indices. For example, Carnochan's (1982) color tables (specifically his Table 2) provide no information for stars cooler than F2 V, F0 III, and A2 I. One might also worry that even those stars above these boundaries and having adequate *IUE* spectra might be peculiar so that only atypically far-ultraviolet-bright representatives of their spectral types were actually detected.

Ultimately, therefore, I chose to use Kurucz's (1991) library of synthetic stellar model atmospheres and integrated the  $\lambda 1565$  passband across all 412 models with solar abundances. I simultaneously integrated over the original  $V$  bandpass (Johnson 1965, his Table A-1) and formed the

$[1565]-V$  indices. I basically followed Carnochan (1982) in setting the "zero point" of color so that an A0 V star ( $T_{\text{eff}}=10\,000$  K, log gravity of 4.0) had  $[1565]-V=-0.57$ . In fact, I preferred to use a more broadly based match to Carnochan's color tables, and compared with Kurucz atmospheres for F0 V, A0 V, B0.5 V, and O6.5 V. The average of these  $[1565]-V$  indices was forced to be correct. I selected those individual Kurucz models, or averages of pairs of models, that corresponded best in log  $T_{\text{eff}}$  and log  $g$  to the 33 normal stellar categories represented in the model's sky, after calculating gravities based on best (most recent) estimates for stellar mass, luminosity, and effective temperature. Ideally, one needs far-ultraviolet representation for the full range of source categories inherent in the sky model (cf. Table 2 of WCVWS). In reality, however, all the AGB stars possess circumstellar dust shells that effectively obliterate all emergent far-ultraviolet light. Therefore, I set all AGB categories to a negligibly faint level in the  $M_{1565}$  table. Likewise I have not yet included the exotica, whose UV spectra are often dominated by emission lines.

I have also made strenuous efforts to improve the pedigree of the model's hardwired  $M_V$  table by cross comparison of several compilations or discussions of absolute  $V$  magnitudes (e.g., Schmidt-Kaler 1982; Humphreys & McElroy 1984; Grenier *et al.* 1985; de Jager & Nieuwenhuijzen 1987). Tables of the absolute 1565A magnitudes,  $M_{1565}$ , were obtained by adding the  $[1565]-V$  color indices to  $M_V$ . Consequently, use of the Kurucz grid, together with these simplifying assumptions and neglect of exotic objects, provided the hardwired *TDI*  $\lambda 1565$  absolute magnitude table for model work.

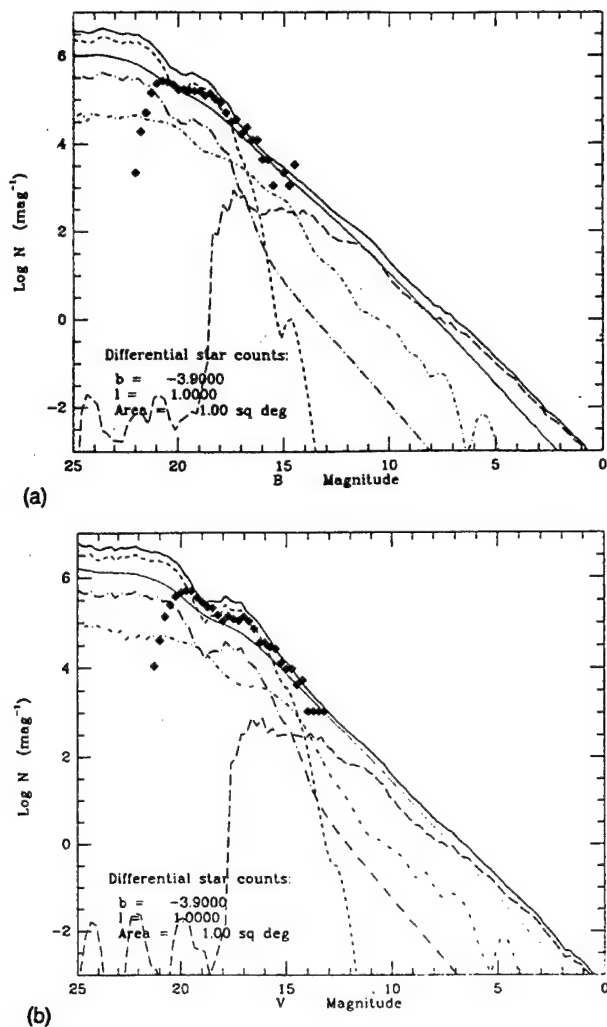


FIG. 4. Performance at  $B$  and  $V$  illustrated by Terndrup's (1988) differential counts for Baade's Window (filled diamonds). Lines as in Fig. 1, with the addition of: short dashes, bulge; short dash-dot, molecular ring. (a)  $B$ . (b)  $V$ . Note the incompleteness of the observed counts fainter than 16th magnitude.

In identical fashion I have hardwired absolute magnitude tables corresponding to the  $\lambda 1400$  band of the S201 Apollo 16 dataset (Page *et al.* 1982) and the Shuttleborne FAUST  $\lambda 1660$  band (Bowyer *et al.* 1993). Analysis of the FAUST database constitutes a separate paper (Cohen *et al.* 1994) so I focus here on analysis of the sky as seen by S201 and *TD1*. Zero points for color indices,  $[1400]-V$ , were set equal to those Carnochan (1982) gives for  $[1565]-V$ .

## 6. FAR-ULTRAVIOLET PERFORMANCE

### 6.1 S201

Because of the limited number of fields involved in this experiment, it is more convenient to discuss SKY's performance at 1400Å first. I made no predictions for the Mensa or Capricorn fields where the LMC and the Earth appear in the field of view, respectively. For four of the remaining eight fields, data were extracted directly from a machine-readable copy of the Revised S201 catalogue provided on the NSSDC's first released CD-ROM of Astronomical Cat-

TABLE 1. Details of S201 target fields modeled.

Target	$l$ (deg)	$b$ (deg)	No. stars	Mode	Average deviation (dex)
Grus	342.0	-70.5	44	$d$	-0.13
Cetus	194.0	-60.0	40	$d$	+0.02 <sup>a</sup>
Aquarius	73.0	-55.0	57	$d$	-0.05
Fornax	223.0	-52.0	24	$d$	-0.02 <sup>a</sup>
Pavo	345.0	-43.5	30	$d$	+0.05
Norma	330.0	-13.0	259	$e, 1.4$	+0.04
Sagittarius	5.5	-10.0	1005	$e, 2.0$	+0.04
Cygnus	83.5	-9.0	812	$e, 4.0$	+0.04

Notes to TABLE 1

Mode is either " $d$ " (default) or " $e$  No." (using extra populations and extinction boosted by No.).

<sup>a</sup>These two fields are better matched by including Gould's Belt (Sec. 6.2). Without modeling Gould's Belt, Cetus and Fornax are each matched to -0.09 dex.

alogs (Vol. 1) (for Cetus, Fornax, Pavo, Norma). For the Grus, Aquarius, Sagittarius, and Cygnus fields, I preferred the individual papers by Carruthers & Page (1983), Carruthers & Page (1984a,b) because these represent deeper analyses of the original data than are available in Page *et al.* (1982). The number of detected sources per field varies widely from 24 (Fornax) to 1005 (Sagittarius). Table 1 summarizes the details of the fields: their approximate central galactic coordinates; the total number of sources; SKY's "mode" for best simulation of the observations (see below); and the average deviation of the best prediction from the counts (in  $\log N$ , measured in dex). The table is organized by decreasing southern galactic latitude.

Figures 5(a)–5(h) illustrate the comparison of predicted differential star counts ( $\log N/\text{mag}/\text{deg}^2$ ) at 1400Å with S201 data. The five high-latitude fields ( $b < -40^\circ$ ) are quite well predicted (given the inherent Poisson errors) by the currently best version far-ultraviolet model, namely one in which the two local spurs are present but their populations are *not* boosted beyond the normal, as are those in the infrared (since we still lack a quantitative detailed description of the extra extinction that attends the clouds along these spiral spurs). However, with this "default" ultraviolet version, the three low-latitude fields of Norma, Sagittarius, and especially Cygnus, are less satisfactorily modeled, although Sagittarius [Fig. 5(g)] lies surprisingly close to this prediction. Running the other option, namely inclusion of the two local spurs, populations boosted according to the best simulation of the midinfrared sky, and allowing the extinction to be artificially boosted solely within the local spurs, these three fields can be better modeled. The requisite increases in the extinction local to the spurs are by factors of 2, 1.4, and 4 times normal, for Norma, Sagittarius, and Cygnus, respectively; all are quite modest given the optical thickness of the clouds and their likely patchiness.

$A_{1565}$  is 8.09 times  $A_V$  (Carnochan 1982) or about 5.0  $\text{mag kpc}^{-1}$  in the Galactic plane. Within the local spurs this quantity is enhanced over the normal value, although it still diminishes perpendicular to the plane as an exponential with a 100 pc scale height. Even if the enhancement



were a factor of 10, the actual length along the line of sight over which  $A_{1565}$  is elevated is never more than 300 pc (even at latitude zero). Therefore, the maximum local extinction,  $A_V$ , attributable to a clump is  $\sim 15$  mag, not unreasonable for a dense molecular cloud core. More typical

extinction boosts of  $\sim 3$  would correspond to cloud cores with total obscuration of  $A_V \sim 5$  mag. Along a line of sight at nonzero latitude, although the extinction is always increased by the same factor over the simple expression of WCVWS, the absolute incremental contribution decreases,

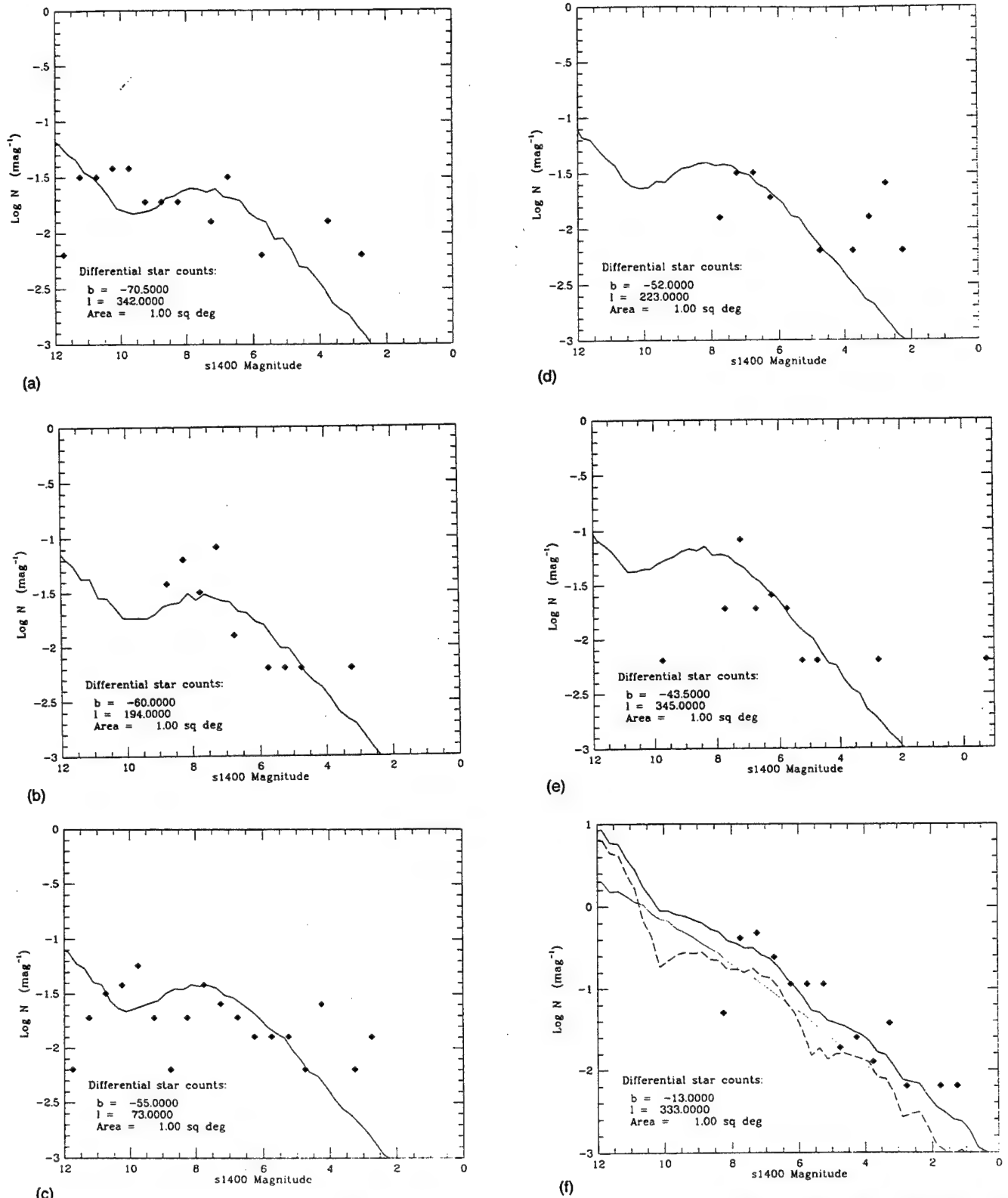
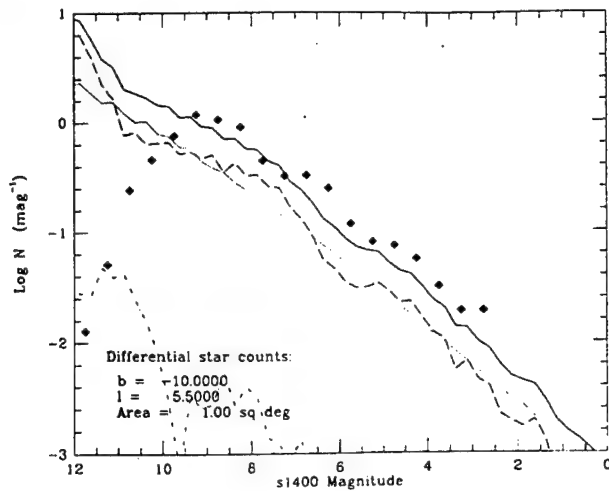
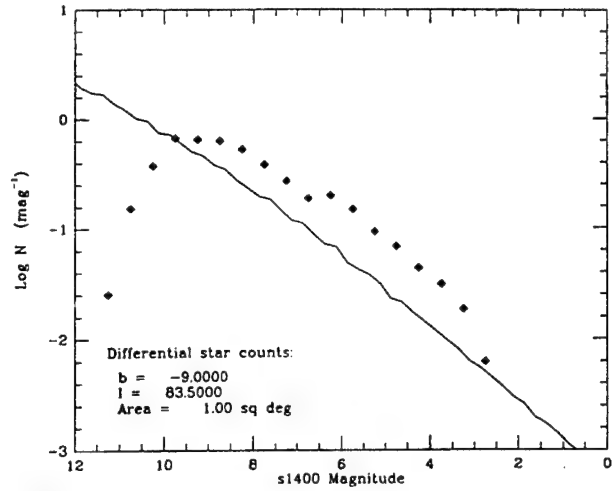


FIG. 5. Comparison of predictions and observed differential starcounts at 1400A for the target fields of the S201 experiment. All models represent the default ultraviolet mode, without extra populations or extra associated extinction in the local spurs. (a) Grus; (b) Cetus; (c) Aquarius; (d) Fornax; (e) Pavo; (f) Norma; (g) Sagittarius; (h) Cygnus. Diamonds: observations. Line styles as in Fig. 1.



(g)



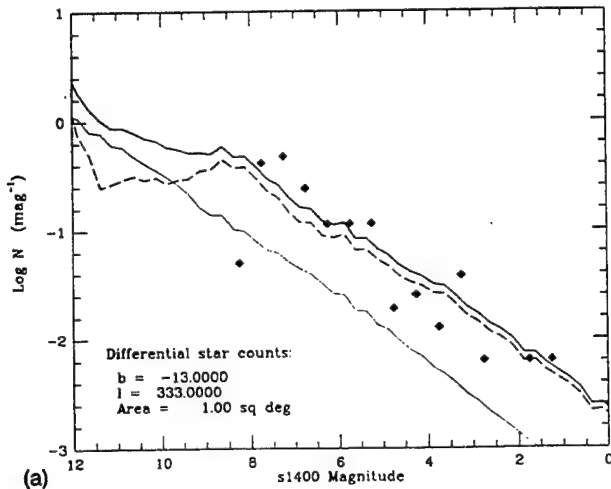
(h)

FIG. 5. (continued)

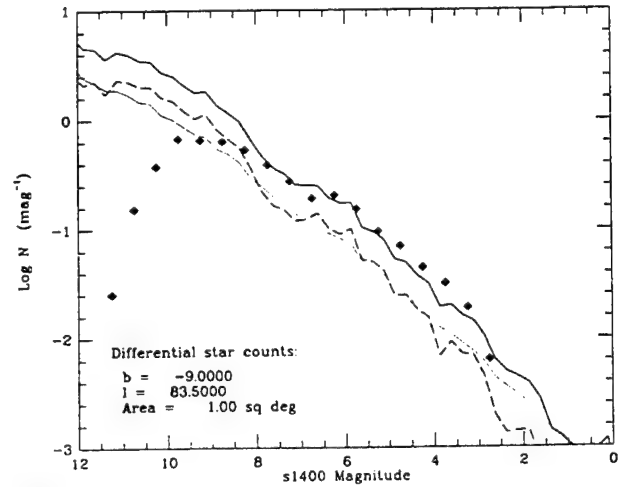
stepping along a ray because the  $z$  distance increases. Figures 6(a)–6(c) represent the boosted-population/enhanced-extinction versions of Figs. 5(f)–5(h). Figure 6(c), for Cygnus, highlights the improvement most dramatically.

To quantify the fidelity of SKY, Table 1 also lists the average deviation (in dex) of the predicted  $\log N$  from the

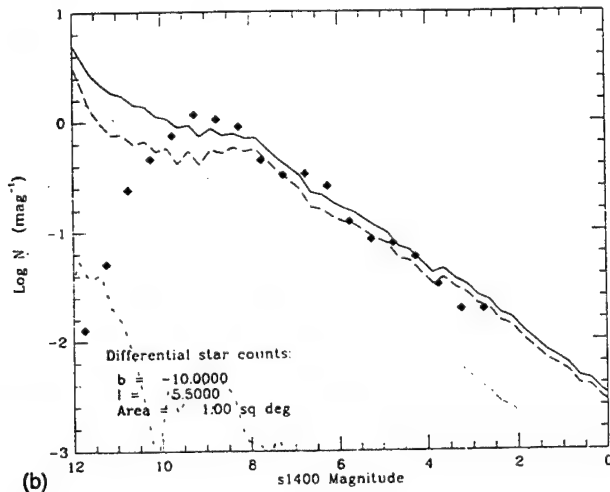
S201 counts for each field, using the best mode of prediction for this assessment [i.e., Figs 5(a)–5(e) and Figs. 6(a)–6(c)]. Occasionally, points that represent obvious incompleteness in the counts have been dropped to evaluate these matches. To recognize the improvements illustrated in Fig. 6, note that the default model's average deviations were: Norma,  $-0.11$  dex; Sagittarius,  $+0.11$ ; Cygnus,



(a)



(b)



(c)

FIG. 6. Comparison of predictions and S201 observed differential star counts at 1400Å. Now SKY is used with boosted local spur populations and increased extinction. (a) Norma, extinction boosted by a factor of 2.0; (b) Sagittarius, the factor is 1.4; (c) Cygnus, the factor is 4.0.

TABLE 2. Regions isolated for comparison with *TDI*.

Latitude range	Longitude range	No. of <i>TDI</i> stars	Area (deg <sup>2</sup> )	Mode
50–90	270–360	103	1550	<i>d</i>
20–40	90–180	562	1200	<i>d</i>
–5–5	0–25	530	250	<i>e</i> ,1.2
–5–5	140–220	1626	800	<i>e</i> ,9.0
–5–10	200–240	519	200	<i>e</i> ,3.0
–10–20	180–270	1307	870	<i>e</i> ,10.
–40–20	0–180	909	3100	<i>e</i> ,4.0
–40–20	270–360	447	1550	<i>e</i> ,4.5
–40–20	180–270	861	1550	<i>d</i>
–90–50	180–270	128	1200	<i>d</i>

Notes to TABLE 2

Mode is either *d* (default) or *e*. No. (using extra populations and extinction boosted by a factor No.).

–0.34. When using the best mode of SKY for each region, typical counts are matched to within a few hundredths of a dex.

### 6.2 *TDI*

Most applications of the model to the far-ultraviolet sky in the future are likely to pertain to issues of smeared stellar surface brightness and the existence of diffuse background radiation. This is clearly best sought at high galactic latitudes. Consequently, I have chosen to describe the high and intermediate latitude performance of the new model. However, the most challenging regions for modeling are always near the Galactic plane. I, therefore, present comparisons with *TDI* for four regions at low latitudes, two of them with  $|b| < 5^\circ$ .

Table 2 summarizes the regions selected for comparison and indicates their galactic latitude and longitude ranges, the total number of stars in the augmented *TDI* database with in-band fluxes above  $3\sigma$  at 1565Å within the region, the approximate area in square degrees, and the mode used for the most accurate prediction by SKY. The table is organized by decreasing latitude of the regions' limits. Figures 7(a)–7(j) illustrate the predictions of the model compared with differential star counts at  $\lambda 1565$ . To assure sufficient stars it was sometimes necessary to extract *TDI* sources over wide areas.

The quadrants near the north Galactic cap follow the predicted total count well, certainly within the Poisson error bars associated with the *TDI* differential counts [Figs. 7(a) and 7(b)]. The two zones chosen to straddle the Galactic plane are also well matched by the model using the boosted stellar populations and extra extinction option. Actually, for Fig. 7(c), the populations are boosted but the extinction is only 20% above that normally expected within the model along this line of sight. In the anticenter direction, however, the extinction was enhanced by a factor of 9.0 in order to match the observed counts [Fig. 7(d)]. The zones presented in Figs. 7(e), 7(g), and 7(h) were selected to sample low-to-intermediate latitudes in the south and all three are well matched by additional spur populations, and extinctions amplified by factors of 3.0, 4.0, and 4.5, respectively.

One advantage of the all-sky nature of *TDI*'s coverage is that one can probe directly for discrepancies arising from Gould's Belt. Stothers & Frogel (1974; hereafter referred to as SF; their Fig. 3) indicate that, in the quadrant  $l = 180^\circ$ – $270^\circ$ , many of the local OB complexes lie systematically below the Galactic plane. In the opposite direction, the distinction between Gould's Belt and the Galactic plane is far less obvious (their Fig. 2). Therefore, I sampled *TDI* in the longitude range  $180^\circ$ – $270^\circ$  for low ( $-10^\circ$  to  $-20^\circ$ ), intermediate ( $-20^\circ$  to  $-40^\circ$ ), and high latitudes ( $-50^\circ$  to  $-90^\circ$ ). None of the predictions illustrated in Fig. 7 had any modeling of Gould's Belt. Although the prediction of the default model is not inconsistent with the observed low starcounts shown in Fig. 7(j) (allowing for Poisson errors), the slope of the *TDI* counts was clearly too flat to be well modeled. Even the inclusion of boosted populations cannot account for the extremely flat distribution of *TDI* starcounts in Fig. 7(i). This localized phenomenon is presumably due to ultraviolet-bright stars in Gould's Belt that are not correctly assessed even by the incorporation of local clouds into SKY. This is a reasonable explanation because the local spurs follow the Galactic plane; they can, therefore, absorb any first quadrant peculiarities due to the rather weak continuation of Gould's Belt into this quadrant. However, the spurs cannot account for the systematic and substantial deviations between Belt and Galactic plane in the third quadrant.

Brosch (1991) explicitly included Gould's Belt in the paper in which he sought to model the S201 counts. One might wonder whether the S201 experiment saw Gould's Belt to any appreciable degree. Only the Cetus and Fornax target fields sample the longitude range at southerly latitudes in which one expects the dominant contribution, if any, from stars in Gould's Belt. Although the counts are very low, Fig. 5(d) does suggest a bimodal distribution of star counts with a bright peak ( $[1400] \sim 3$ ) of the same height as the faint peak ( $[1400] \sim 7$ ). One of the optional output files from SKY is a cumulative breakdown of the disposition of stars predicted in any field among their 87 source categories and among the five distinct Galactic components. Running this option for the Fornax field at 1400Å indicates that the primary contributor to *TDI* 1565Å counts near seventh magnitude is the category of B8–A0 V stars in the disk. The observed bright peak near third magnitude would be consistent with early B stars seen at distances of  $\sim 200$  pc, in the Belt.

This plausibility analysis and the strangely flat *TDI* differential counts suggested the value of including a geometrical component to represent the effects of Gould's Belt. After study of SF's Figs. 2 and 3, and comparison of a number of *TDI* starcounts with SKY over a wide range of latitudes and longitudes, I chose to treat Gould's Belt as proportional to the local disk population, concentrated to the latitude range  $-12^\circ$  to  $-65^\circ$  and longitude range  $191^\circ$ – $252^\circ$ . This wedge is truncated at a distance 800 pc from the Sun and consists solely of the hottest OB categories included in the model (namely "young OB stars," "B0,1 V," "B2,3 V," and "B5 V"). Because I could see no apparent effects of the Belt on counts north of about  $-12^\circ$  latitude,

the upper latitude limit was set by an OB star 1 scale height (90 pc) above the plane of the Belt (itself inclined  $19^\circ$  below the Galactic plane: SF) and at 800 pc from the Sun. The lower latitude limit was determined by an OB star 1

scale height below the plane of the Belt when viewed on the inner edge of the 200 pc diameter "hole" in the projected distribution of O-B5 stars discussed by SF, whose closest approach to the Sun is about 90 pc in the quadrant  $180^\circ$ –

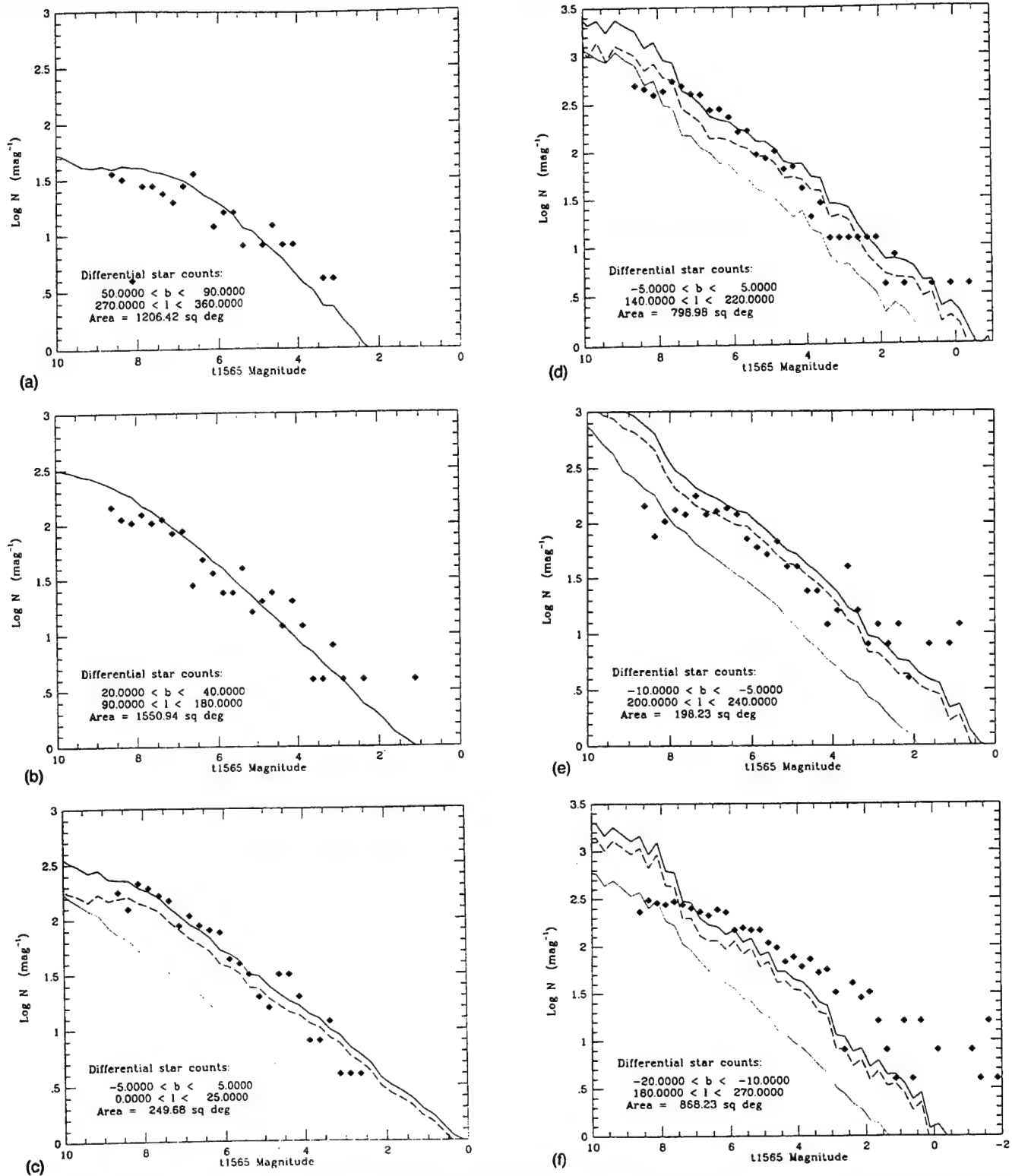


FIG. 7. Model predictions for the far-ultraviolet sky compared with *TDI* differential counts at 1565 Å (for magnitudes within *TDI*'s linear regime). None of these predictions included any representation of Gould's Belt. (a) Default model used (no additional local populations; no extra extinction) for a high latitude region near the north Galactic pole; (b) as in (a) but for a northern intermediate latitude zone; (c) low latitude inner Galaxy zone modeled with extra (spur) populations and associated extinction; (d) anticenter zone modeled with extra populations and associated extinction; (e) as in (d) but for a southern low intermediate latitude zone; (f) as in (e) but for a region where the effects of Gould's Belt are apparent; (g) intermediate southern latitude region; (h) as in (g); (i) as in (f) but for higher southern latitudes; (j) quadrant near the south Galactic cap where Gould's Belt may be important. Line types are as in Fig. 1. Note that Gould's Belt counts are absorbed into the component curve for the arms (long dashes).

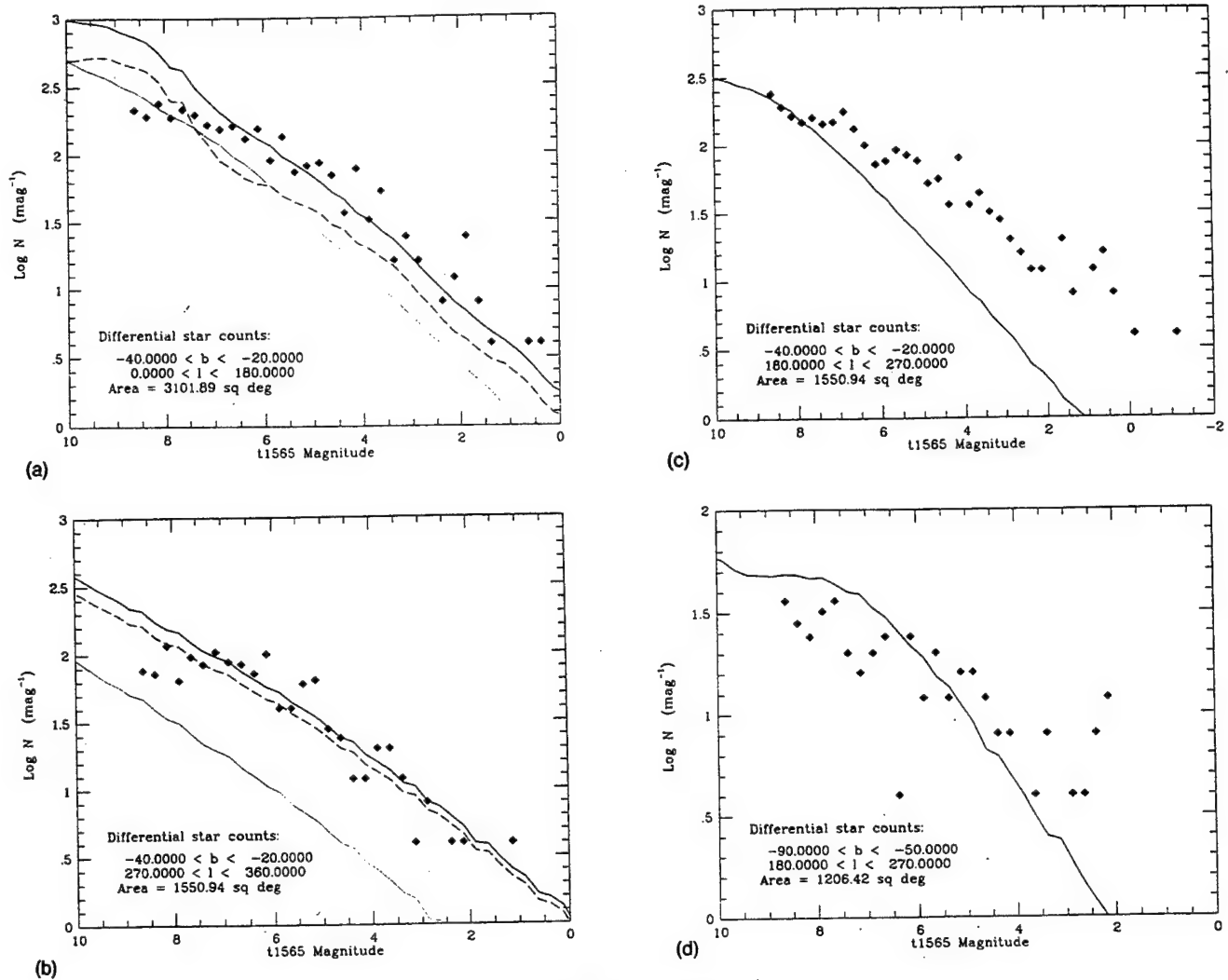


FIG. 7. (continued)

270°. The longitude range was determined from Fig. 3 of SF. The plethora of stellar concentrations in the three remaining quadrants as displayed by SF do not appear significantly displaced from the Galactic plane. Therefore, I chose not to modify the model in any quadrant other than the third. The volume density in Gould's Belt was set at 9.0 times that of the disk throughout the appropriately defined volume. This normalization ensured that the projected areal density of stars in Gould's Belt relative to that in the galactic disk was about 3:1 (see SF), using the characteristic thicknesses for the stellar distributions given in SF's Table V.

Figures 8(a)–8(e) illustrate the consequences of including this extra component on the predictions of the model for S201 and *TDI* counts in the southern third quadrant. For the S201 Cetus and Fornax fields, the absolute value of the average deviations between SKY and the observed counts drops by a factor of 4.5 to only 0.02 dex. The “total” curves of the model's predictions are now capable of matching the very flat differential counts observed by *TDI*, notably those in Fig. 8(d). (Note the behavior of the long-dashed curves in Fig. 8: for housekeeping purposes, I assigned belt stars to the spiral arms' counts.) Figure 8(c) includes the Orion region so it is not surprising that at this

relatively low latitude it is necessary to amplify the local far-ultraviolet extinction by a factor of 10.0. The four other zones are at much higher latitudes where the model without boosted populations and extinctions is appropriate.

*TDI* is felt to be complete to an ultraviolet magnitude of 8.0 (e.g., Gondhalekar 1990). Inspection of Figs. 7(a)–7(d) suggests that this is a fair estimate. There may be some mild latitude dependence but, in all these fields, the observed counts perceptibly roll away from the predictions near  $[1565]=8$ .

## 7. CONCLUSIONS

Improvement in the geometrical representation of the local spiral spurs and sculpting due to molecular clouds has greatly enhanced the fidelity of the model's simulations of the midinfrared sky. Blue and visible performance is perfectly satisfactory, insofar as it has been possible to provide detailed tests of the model. In spite of the necessary simplifications described above, far-ultraviolet performance is very good at high and intermediate latitudes, particularly with the incorporation of Gould's Belt. In the Galactic plane it is also adequate, although I would like to make these predictions more meaningful by improving the

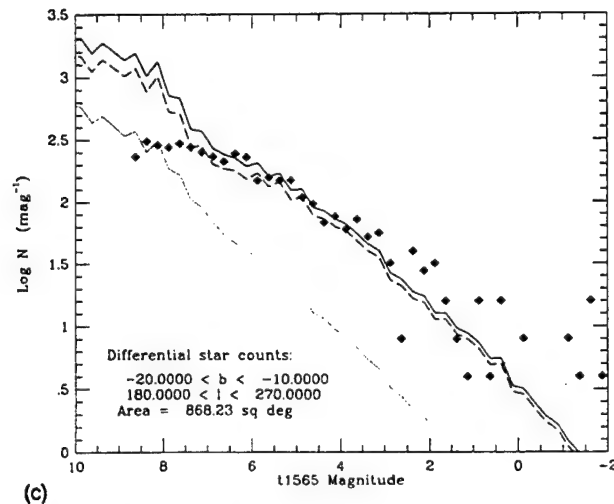
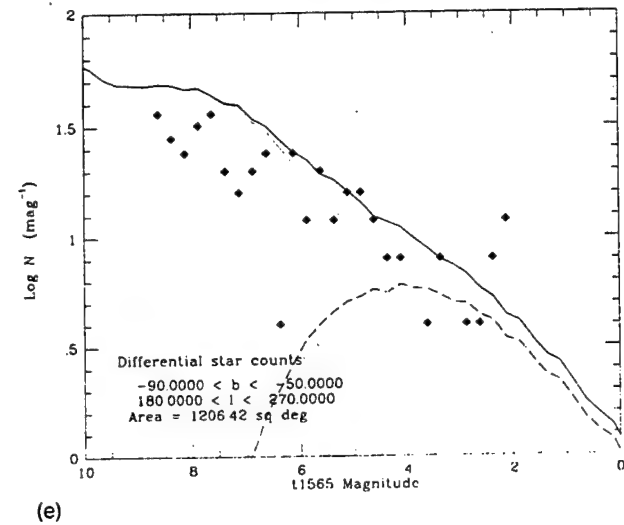
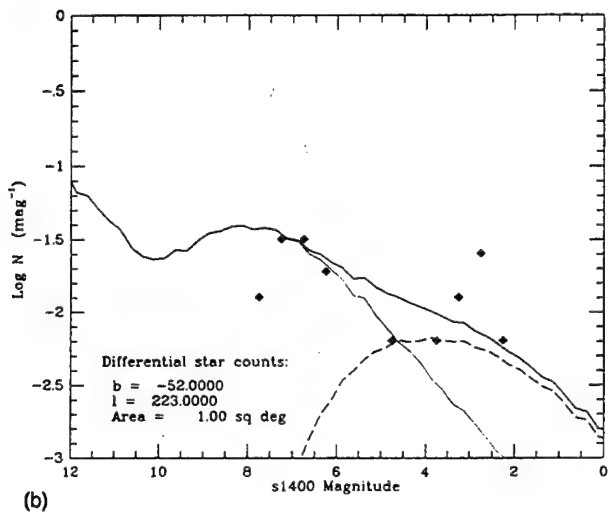
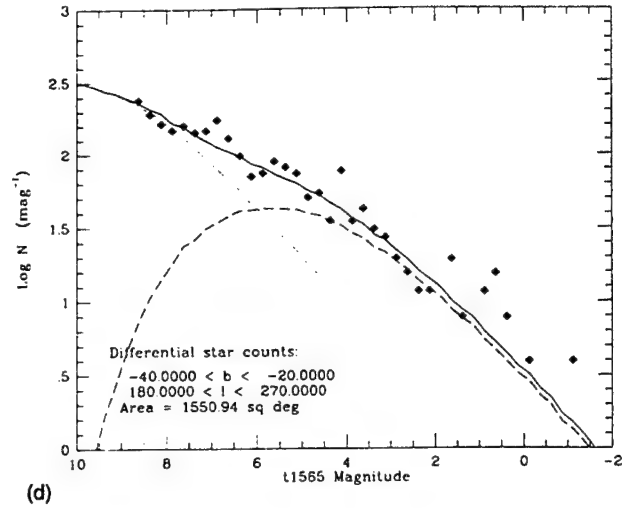
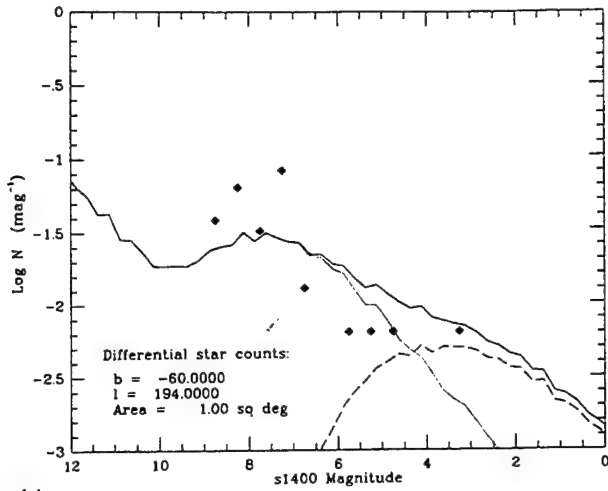


FIG. 8. Model predictions for the far-ultraviolet sky incorporating the effects of Gould's Belt. (a) S201, Cetus field; (b) S201, Fornax; (c) *TDI*, at lowish southern latitudes; (d) as in (c) for intermediate latitudes; (e) as in (c) for high latitudes.

extinction model for local molecular clouds rather than having to use ultraviolet counts essentially as a probe of enhanced extinctions. With regard to the adequacy of this model for far-ultraviolet work, I conclude the following.

(1) SKY's implicit source table represents the content of the far-ultraviolet sky well enough to test existing far-ultraviolet starcounts.

(2) On the basis of both S201 and *TDI* counts, I cannot conclude yet that white dwarfs are important to a good

far-ultraviolet sky simulation. If their inclusion represents only a 10% effect (cf. Brosch 1991) then Poisson errors and other uncertainties (e.g., extinction) militate against their recognition.

(3) A conclusion like (2) must pertain also to the horizontal-branch stars; the relevant evolutionary phases are very short, and the current datasets are not adequate to test more rigorous simulations.

(4) The Kurucz grid of model atmospheres can be used

to supply the requisite broadband  $M_{FUV}$  tables to add far-ultraviolet passbands to the model's repertoire.

(5) The relatively simple expression for interstellar extinction is still sufficient at intermediate and high latitudes. At low latitudes it is desirable already to have determined the line-of-sight extinction, e.g., from CO emission surveys, but far-ultraviolet starcounts in conjunction with the model can effectively suggest enhancements in extinction in specific directions over the model's current expectations.

(6) Inclusion of Gould's Belt is important to modeling a shallow all-sky survey such as *TDI* where one wishes to match the observed distribution of bright stars. If, however, the purpose of a model is to extrapolate greatly below *TDI*'s thresholds to simulate the appearance of the far-ultraviolet sky at very low flux levels, the influence of Gould's Belt should be minimal on faint starcounts. The reason is that the Belt is an intrinsically local phenomenon, populated by relatively few, but luminous, objects. At faint magnitudes, the line-of-sight integration must be dominated by the disk and by the plethora of less luminous

stars. Indeed, I am indebted to Dr. R. Henry for carrying out an experiment with the *TDI* dataset by which a series of 1565A all-sky brightness maps are made with different displays and contrast "stretches" to emphasize fainter and fainter stars. Scaled to the peak brightness one clearly sees Gould's Belt, tilted across the Galactic plane. But dropping the saturation limit of the display by a factor of 100 makes the tilted aspect of the Belt almost vanish; now the Galactic plane dominates the faint *TDI* sky.

Past and current development of this model is supported by the US Air Force Phillips Laboratories through Dr. Stephan D. Price under Contract No. F19628-92-C-0090 with JS&E, Inc. I am grateful to Dick Henry, Jayant Murthy, Marsha Allen, and Tim Sasseen for valuable discussions on the FUV sky and its databases, and to Harold Weaver for useful discussions on the structure of the local spurs. I am grateful to NASA-Ames Research Center for support at Berkeley through cooperative Agreement No. NCC 2-142.

#### REFERENCES

- Bahcall, J. N., & Soneira, R. M. 1984, *ApJS*, 55, 67  
 Blaauw, A. S. 1991, in *The Physics of Star Formation and Early Stellar Evolution*, edited by C. J. Lada and N. D. Kylafis (Kluwer, Dordrecht), p. 125  
 Bohlin, R. C., Holm, A. V., Savage, B. D., Snijders, M. A. J., & Sparks, W. M. 1980, *A&A*, 85, 1  
 Boksenberg, A., et al. 1973, *MNRAS*, 163, 291  
 Bowyer, S., Sasseen, T. P., Lampton, M., & Wu, X. 1993, *ApJ*, 415, 875  
 Brosch, N. 1991, *MNRAS*, 250, 780  
 Carnochan, D. J. 1982, *MNRAS*, 201, 1139  
 Carnochan, D. J. 1989, cited by Gondalekhar, P. M. (1990)  
 Carruthers, G. R., & Page, T. 1983, *ApJS*, 53, 623  
 Carruthers, G. R., & Page, T. 1984a, *ApJS*, 54, 271  
 Carruthers, G. R., & Page, T. 1984b, *ApJS*, 55, 101  
 Cohen, M. 1993, *AJ*, 105, 1860  
 Cohen, M., Sasseen, T., & Bowyer, S. 1994, *ApJ* (in press)  
 Dame, T. M., et al. 1987, *ApJ*, 327, 706  
 de Jager, C., & Nieuwenhuijzen, H. 1987, *A&A*, 177, 217  
 Garzon, F., Hammersley, P. L., Mahoney, T., Calbet, X., Selby, M. J., & Hepburn, I. D. 1993, *MNRAS* (in press)  
 Gondalekhar, P. M. 1990, in *The Galactic and Extragalactic Background Radiation*, IAU Symposium No. 139, edited by S. Bowyer and C. Leinert (Kluwer, Dordrecht), p. 49  
 Grenier, S., Gomez, A. E., Jaschek, C., Jaschek, M., & Heck, A. 1985, *A&A*, 145, 331  
 Heck, A., Egret, D., Jaschek, M., & Jaschek, C. 1984, ESA SP-1052  
 Henry, R. C. 1991, *ARA&A*, 29, 89  
 Henry, R. C., Landsman, W. B., Murthy, J., Tennyson, P. D., Wofford, J. B., & Wilson, R. 1988, *Atlas of the Ultraviolet Sky* (The Johns Hopkins University Press)  
 Humphreys, R. M., & McElroy, D. B. 1984, *ApJ*, 284, 565  
 Johnson, H. L. 1965, *ApJ*, 141, 941 (Table A-1)  
 Kurucz, R. L. 1991, NATO ASI Ser. C, Math. Phys. Sci., Vol. 341, 441  
 Landsman, W. B. 1984, PhD. thesis, The Johns Hopkins University (University Microfilms, Ann Arbor, Michigan), pp. 85-86  
 Murthy, J. 1992, private communication  
 Page, T., Carruthers, G. R., & Heckathorn, H. M. 1982, NRL Rep. 8487  
 Pennington, R. L., Humphreys, R. M., Odewahn, S. C., Zumach, W., & Thurmes, P. M. 1993, preprint  
 Schmidt-Kaler, T. 1982, in *Landolt-Bornstein, Neue Serie*, Vol. 2 part b, (Springer-Verlag), pp. 14-18  
 Stothers, R., & Frogel, J.A. 1974, *AJ*, 79, 456  
 Terndrup, D. M. 1988, *AJ*, 96, 884  
 Wainscoat, R. J. 1992, private communication  
 Wainscoat, R. J., Cohen, M., Volk, K., Walker, H. J., & Schwartz, D. E., 1992, *ApJS*, 83, 111 (WCVWS)  
 Walker, H. J., Cohen, M., Wainscoat, R. J., & Schwartz, D. E. 1989, *AJ*, 98, 2163  
 Wu, C.-C., Crenshaw, D. M., Blackwell, J. H., Wilson-Diaz, D., Schiffer III, F. H., Burstein, D., Fanelli, M. N., & O'Connell, R. W. 1991, *IUE Newslett.* 43, UV Spectral Atlas: Addendum I



## **8. Appendix B. Data Analysis Papers**

## THE GALACTIC FAR-ULTRAVIOLET SKY AS SEEN BY FAUST: MODELING AND OBSERVATIONS

MARTIN COHEN,<sup>1</sup> TIMOTHY P. SASSEEN,<sup>2</sup> AND STUART BOWYER<sup>2,3</sup>

Received 1993 September 13; accepted 1993 November 23

### ABSTRACT

We test the model of the Galactic point source sky recently extended to the far-ultraviolet by Cohen (1994) against the set of Galactic far-ultraviolet point sources detected by the FAUST experiment. We find excellent agreement between the predicted ( $\log N$ ,  $\log S$ ) and the observed source counts for a range of Galactic directions observed by FAUST. At low galactic latitudes, we can directly infer the amount of interstellar extinction in a given direction associated with local molecular complexes, based on comparison of model calculations and FAUST star counts. The model can also be used to predict the statistical stellar content of any field. We compare the model predictions with the observations of Brosch et al. (1994), who have spectroscopically studied an optically identified complete sample of FAUST objects in a region near the north Galactic pole. We have used the model to determine that the contribution of far-ultraviolet stars fainter than  $6 \times 10^{-14}$  ergs  $s^{-1} cm^{-2} \text{\AA}^{-1}$  (the FAUST detection limit) is less than 1% of the diffuse sky brightness, and less than about 4% of the total point source flux.

*Subject headings:* diffuse radiation — ultraviolet: ISM

### 1. INTRODUCTION

Few models exist that describe the point source content of the far-ultraviolet sky, as opposed to the diffuse background. Even when such models have been reported, based upon the conversion from optical star catalogs to expected far-ultraviolet emission from those same stars (e.g., Henry 1977), the final representations have always been degraded to portray the expected stellar contribution to the diffuse far-ultraviolet sky. Only recently was a stellar viewpoint adopted by Brosch (1991). He adapted the Bahcall & Soneira (1980) galaxy model to the 1500–2500 Å sky, adding white dwarfs and including Gould's Belt as an extra ultraviolet-specific geometrical component. Brosch compared this modified Bahcall-Soneira model to the *Apollo 16* S201 experiment's counts at 1400 Å (Page, Carruthers, & Heckathorn 1982).

Cohen (1994) has recently described an extension of the original Wainscoat et al. (1992: hereafter WCVWS) and Cohen (1993) "SKY" model to the far-ultraviolet. The new version of the model contains an even more richly detailed Galactic geometry than WCVWS used, comprising a disk, halo, bulge, spiral arms, and two local spurs in which the stellar populations can be augmented by those associated with local molecular clouds, and a molecular ring. Cohen (1994) also added a component to represent Gould's Belt. The original model was developed to predict the appearance of the near- and mid-infrared point source sky by simulating ( $\log N$ ,  $\log S$ ) source count curves in either differential or cumulative form, and for an arbitrary bandpass. It populates the sky with 87 different types of celestial object, some or all of which can belong to any of these distinct Galactic components. Cohen's (1994) (fourth) version of the code simulates the *IRAS* point source sky extremely well because of its improved geometry. To mimic the

effects of local molecular clouds that follow the local spurs of the spiral arms, the stellar populations of both the disk and arms components are multiplicatively boosted where the line of sight is strictly within the local spurs. In the far-ultraviolet, the default mode of operation of the model is one in which both the local spurs are present but their normal populations are *not* boosted, essentially because we do not yet have a quantitative assessment of the extra extinction associated with these local clouds, which plays an important role in the far-ultraviolet. Galaxies are not represented in the model's far-ultraviolet sky. The new version of the model performs well predicting the *Apollo 16* S201 1400 Å source counts and has been compared with wide areas of the 1565 Å all-sky survey made by *TD-1* (Cohen 1994).

In the present paper we describe the customization of this model and its application to the analysis of the sky at 1600 Å as observed by the Far-Ultraviolet Space Telescope (FAUST), flown on the shuttle *ATLAS-1* in 1992 March. We (i) test the performance of this model in terms of  $\log N$ – $\log S$  against the sky most deeply probed by FAUST; (ii) interpret the stellar content of the FAUST sky in terms of spectral types observed at a variety of galactic longitudes and latitudes; (iii) deduce the character of extinction in the far-ultraviolet in the lowest latitude FAUST fields; and (iv) use the model to make predictions for the contribution to the diffuse Galactic far-ultraviolet background from faint stars.

### 2. THE FAUST DATA SET

Details of the FAUST experiment including calibration, a description of the data set obtained, and preliminary results are described by Bowyer et al. (1993). Briefly, the FAUST telescope is a 2-mirror Wynne camera with photon-counting microchannel plate detector and a bandpass from ~1400 to 1800 Å. Almost 5000 sources were detected in 21 separate regions studied. Two are 30° long scans across the sky, the remaining 19 are pointed observations of the 7.6 diameter field at specific target positions. Here we have extracted those point sources from 12 fields whose in-band fluxes place them at least  $4\sigma$  above the local background emission. We have identified

<sup>1</sup> Jamieson Science & Engineering, Inc., 5321 Scotts Valley Drive, Suite 204, Scotts Valley, CA 95066, and Radio Astronomy Laboratory, University of California, Berkeley, CA 94720.

<sup>2</sup> Center for EUVE Astrophysics, University of California, Berkeley, CA 94720.

<sup>3</sup> Department of Astronomy, University of California, Berkeley, CA 94720.

(via search of the RC 3 catalog) the known galaxies in each field and have removed these from the point source counts when they make appreciable contributions to these counts. We have chosen here not to model fields containing the Magellanic Clouds, fields with short (<8 minute) exposures, or fields which showed geophysical contamination.

### 3. CUSTOMIZATION OF THE MODEL FOR FAUST

We follow Cohen's (1994) approach to develop a table of absolute 1660 Å magnitudes for all the 87 categories of source with which the model populates the point source sky. FAUST's system response function is given by Bowyer et al. (1993). We integrated the  $\lambda$ 1660 FAUST passband across all the 412 stellar model atmospheres with solar abundances in Kurucz's (1991) library of synthetic atmospheres, and integrated over the original Johnson (1965, his Table A-1)  $V$  bandpass to form the  $[1660] - V$  color indices. We defined FAUST magnitudes exactly as Carnochan (1982) did for  $TD-1$ , namely

$$[1660] = -2.5 \log_{10} F(\lambda) - 21.175,$$

where  $F(\lambda)$  is the observed specific monochromatic intensity in units of  $\text{ergs cm}^{-2} \text{s}^{-1} \text{\AA}^{-1}$  (the zero point is that of Hayes & Latham 1975). We essentially followed Carnochan (1982) in setting the "zero point" of color index so that an A0 V star ( $T_{\text{eff}} = 10,000 \text{ K}$ ,  $\log$  gravity of 4.0) has  $[1660] - V = -0.56$  (by linear interpolation in wavelength between his values of intrinsic  $[1665] - V$  and  $[1565] - V$ ). In fact, we used a more broadly based match to Carnochan's color tables, and compared with Kurucz atmospheres for F0 V, A0 V, B0.5 V, and O6.5 V. We adopted the average of the offsets between Kurucz and Carnochan indices for these four spectral types as our zero point offset in  $[1660] - V$ . We selected those individual Kurucz models, or averages of pairs of models, that corresponded best in  $\log T_{\text{eff}}$  and  $\log g$  to the 33 normal stellar categories represented in the model's sky, after calculating gravities based on recent estimates for stellar mass, luminosity, and effective temperature. This method furnished  $M_{1660}$  magnitudes for all 33 normal types of star by adding  $[1660] - V$  indices to the values of  $M_V$  that the model uses (see Cohen 1994).

All the asymptotic giant branch (AGB) stars were set to a negligibly faint level of  $M_{1660}$  because their associated circumstellar dust shells will absorb all emergent far-ultraviolet light. Likewise we have effectively excluded the more exotic objects (H II regions, planetary and reflection nebulae, T Tau stars: cf.

Table 2 of WCVWS), whose UV spectra are often dominated by a few narrow emission lines, that would make negligible 1660 Å contributions. Use of the Kurucz grid together with these simplifying assumptions provided the  $\lambda$ 1660 absolute magnitude table for model work. SKY currently uses a spatial "double exponential" extinction law whose separate radial, vertical, and wavelength dependences are treated as invariable with galactic longitude and latitude. Bless & Savage (1972) found evidence of far-ultraviolet spectral variations in the form of the extinction law. Excluding the peculiar environs of  $\theta^1$  Ori and  $\sigma$  Sco, however, these data indicated variations of only about  $\pm 10\%$  about the average ratio of  $A_{1660}/A_V$  (their Fig. 6). But their observations treated only 17 relatively local OB stars and the authors themselves remarked that this sample was unsuitable for eliciting any dependence of extinction law on galactic structure. Bless & Savage (1972) argued that these anomalous extinction laws reflected local modifications of interstellar grains due to intense radiation fields. More recently, Carnochan (1982) analyzed 1200 stars using the  $TD-1A$  database and offered the average far-ultraviolet extinction in the  $\lambda\lambda 1400-2740$  range. He saw no significant deviations from this average curve either with line-of-sight direction or wavelength. Consequently, for the normal interstellar extinction we adopted  $A_{1660}/A_V$  of 7.78 by inspection of Carnochan's (1982) Table 1 for  $\lambda$ 1675.

### 4. COMPARISON OF MODEL PREDICTIONS WITH FAUST

Table 1 summarizes those FAUST fields (using the same numbers as Bowyer et al. 1993 assigned) for which we have run the model and predicted the source counts. This table summarizes for each field: the principal FAUST target; the field-center pointing in galactic longitude and latitude; the area we analyzed; the total number of sources detected; the number of galaxies identified; and the average deviation in  $\log N$  (measured in dex) between the model used to represent the region most accurately (see below) and the FAUST number counts (possibly omitting the faintest points where incompleteness is apparent). (For reference, Fig. 3 provides an Aitoff projection map showing the locations of all these FAUST fields.) None of the FAUST target fields lies in that portion of the sky dominated by Gould's Belt; hence this new data set does not provide any additional tests of the fidelity of the model's representation of the Belt.

In Figures 1a-1l we compare our model predictions with the observed FAUST source counts. We corrected the observed counts for galaxies in all fields except 5, 14, and 17 whose low

TABLE 1  
DETAILS OF FAUST TARGET FIELDS MODELED

Field	Target	$l$	$b$	Area (deg <sup>2</sup> )	Sources	Galaxies	Fit (dex)
2	Dorado	265.93	-44.08	20.131	38	4	+0.10
5	PKS 0745	235.27	3.35	34.238	563	1	+0.06
8	Near NGP	250.23	75.32	34.238	56	10	+0.04
9	M87	284.25	73.83	35.213	154	68	-0.16
10	Virgo	280.45	76.67	34.773	102	59	-0.13
11	Virgo	283.11	71.63	35.453	143	61	-0.10
13	Near NGP	277.46	82.95	33.609	57	4	+0.03
14	Centaurus	301.96	22.59	27.578	85	5	-0.04
15	Coma 1	54.57	88.34	31.786	33	7	+0.02
16	M83	314.41	33.65	31.786	83	10	-0.02
17	Ophiuchus	5.59	9.67	34.039	166	3	+0.07
18	NGC 6752	336.39	-24.82	24.000	136	7	+0.01

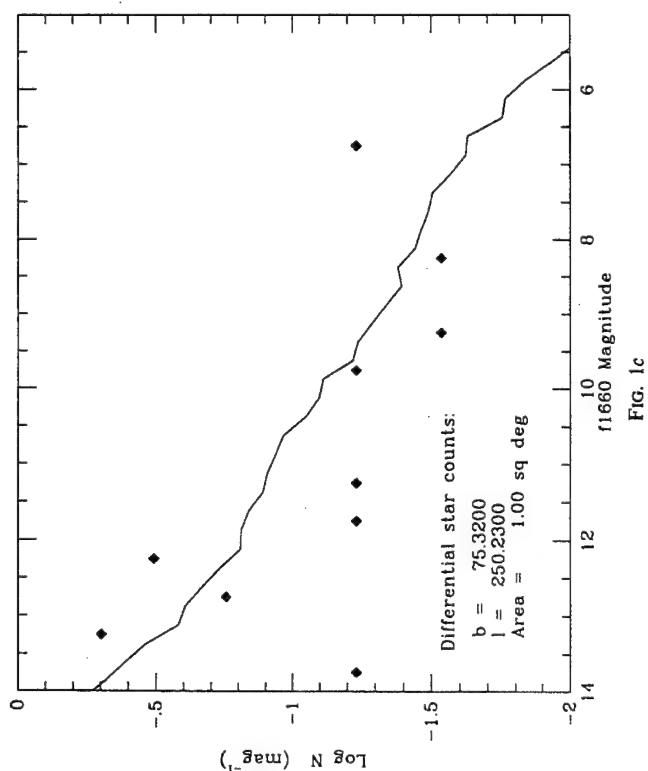
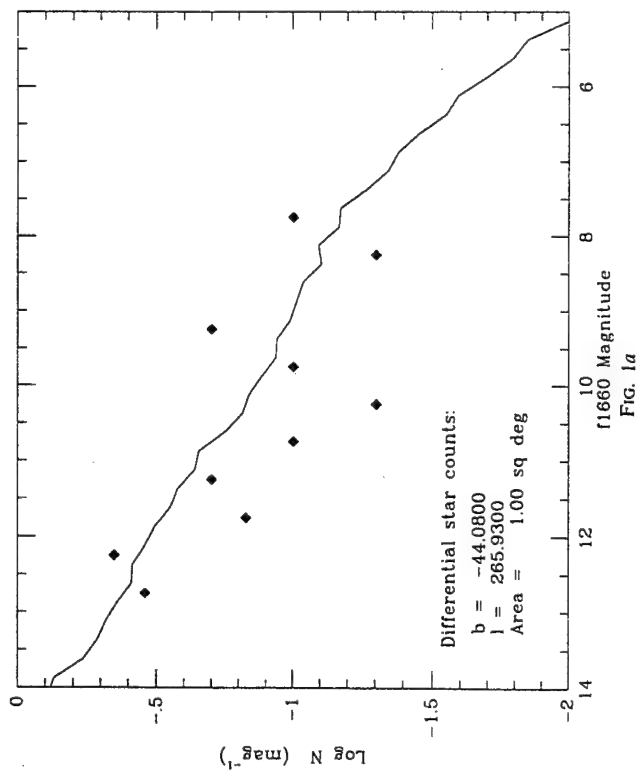
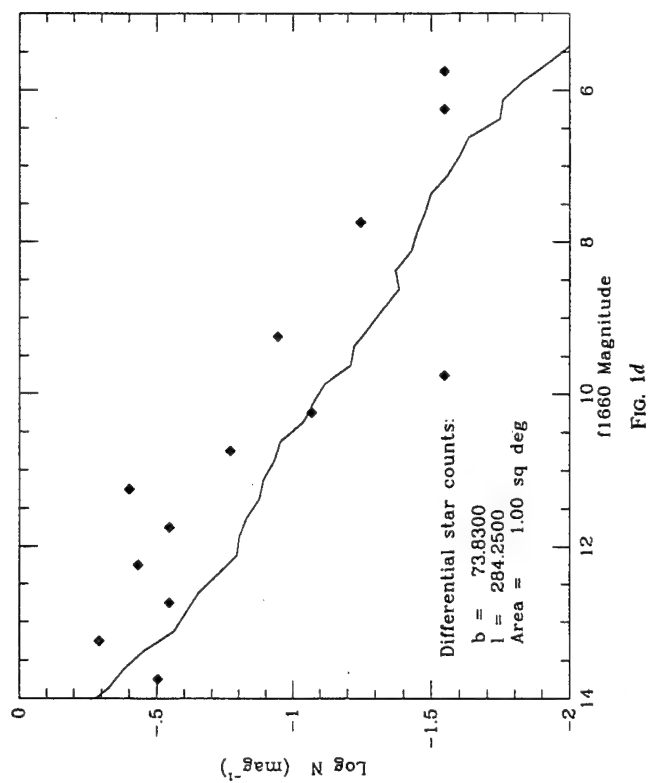
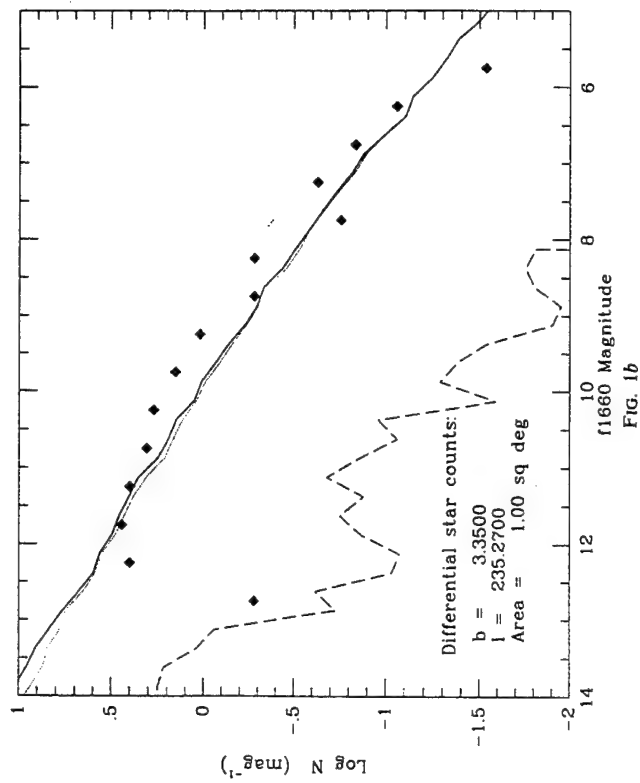
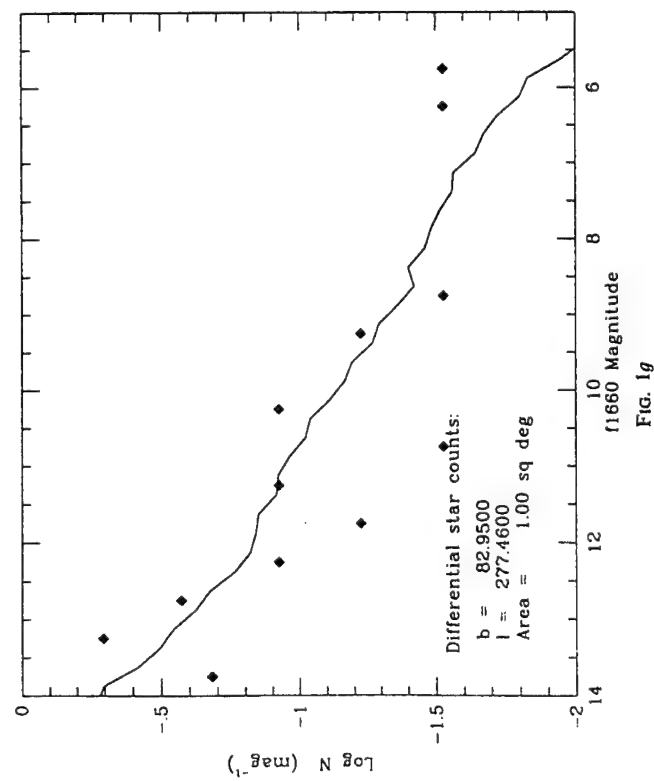
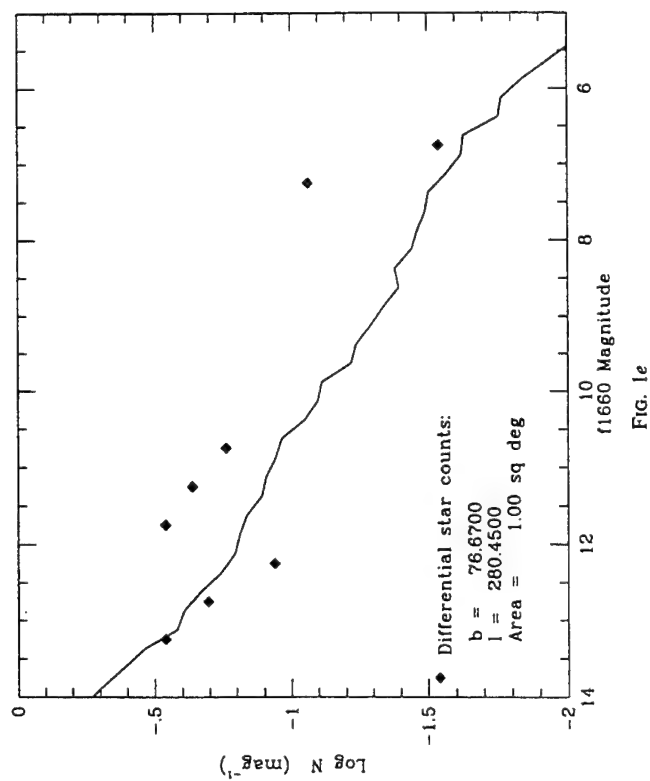
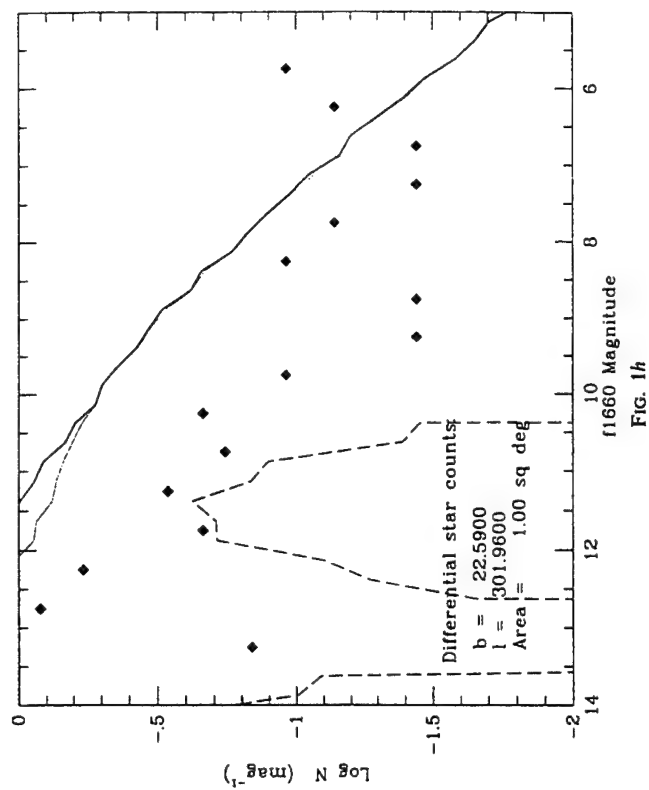
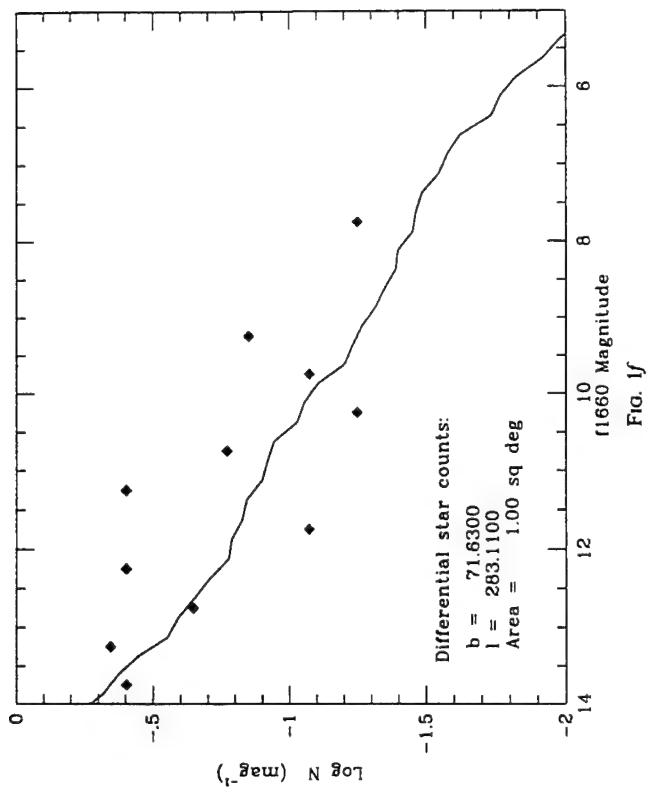


Fig. 1.—Comparison between SKY's predicted differential counts and those measured by FAUST. In this and subsequent figures, diamonds represent observed counts; solid line, total model prediction; dots, disk (often indistinguishable from the solid line); long dashes, arms; short dash-dot, molecular ring. Each figure is labeled with the Galactic coordinates of the center of the fully sampled FAUST field. (a) field 2; (b) field 5; (c) field 8; (d) field 9; (e) field 10; (f) field 11; (g) field 13; (h) field 14; (i) field 15; (j) field 16; (k) field 17; (l) field 18.



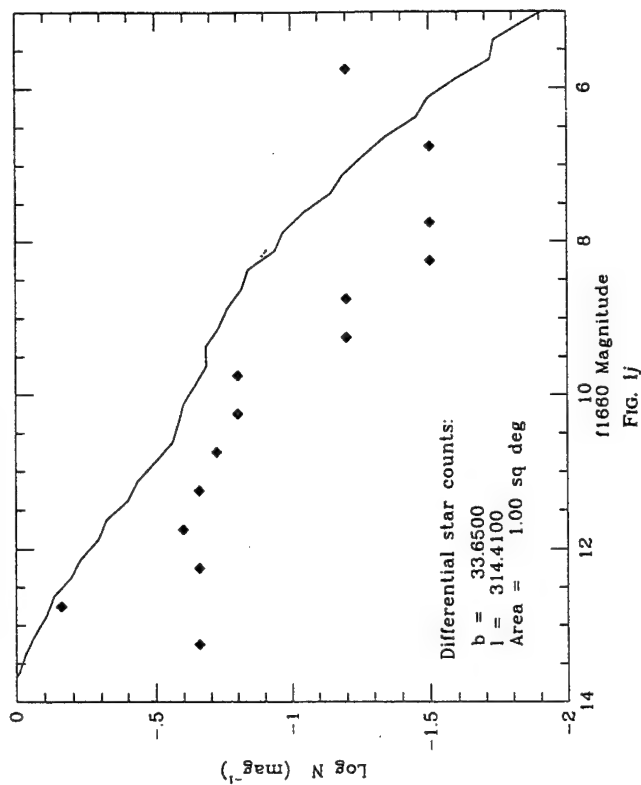


FIG. 1j

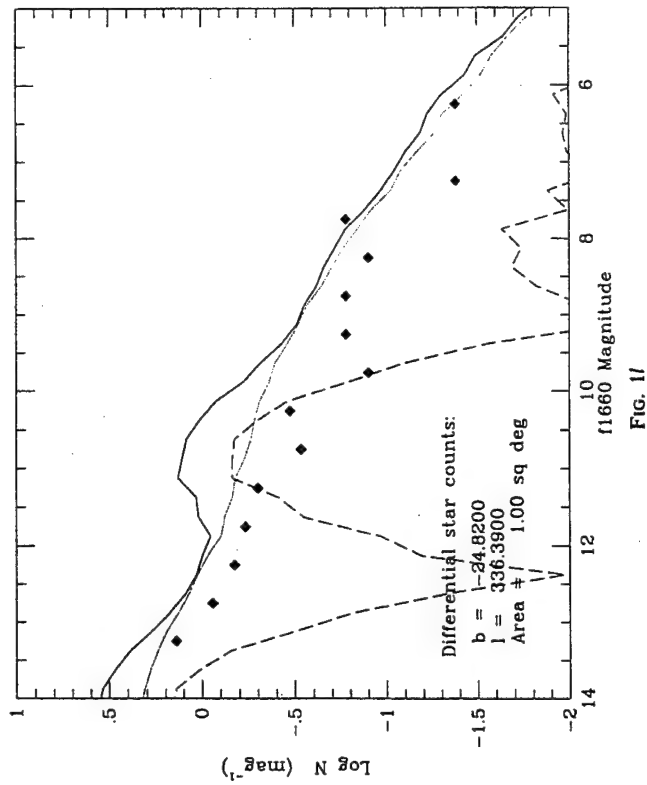


FIG. 1i

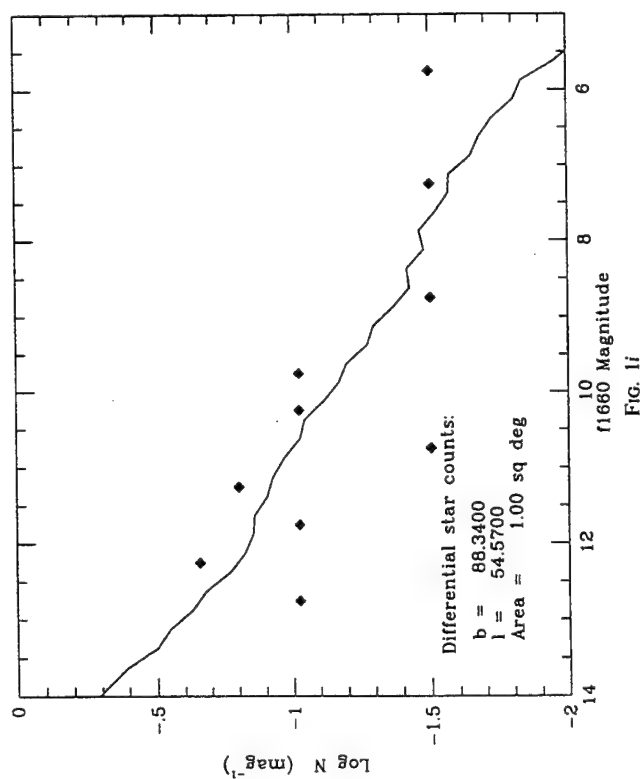


FIG. 1l

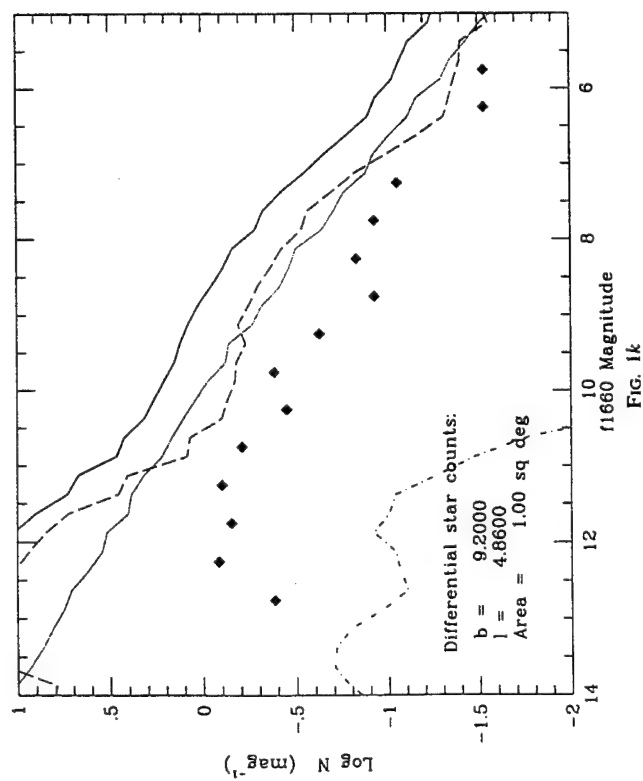


FIG. 1k

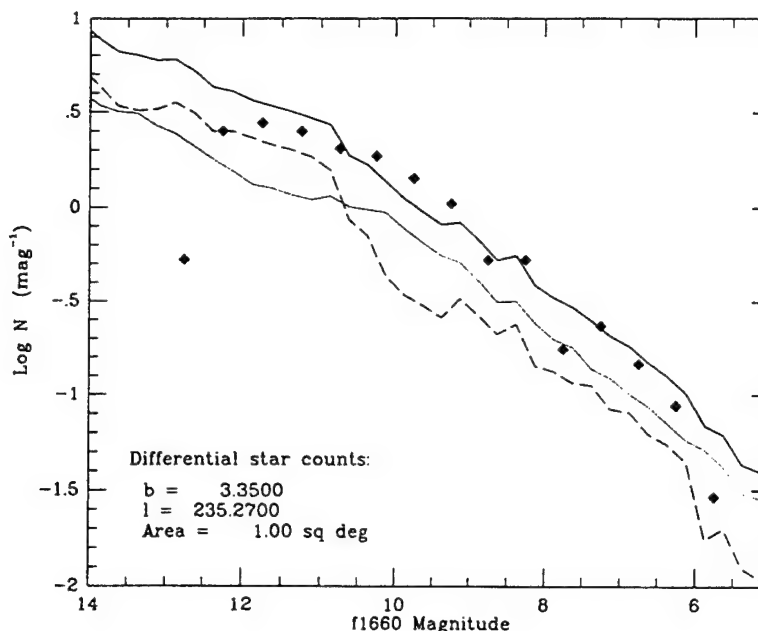


FIG. 2a

FIG. 2.—As in Fig. 1 but now using the enhanced populations mode that produces the best simulation of the mid-infrared sky together with increased far-ultraviolet extinction in the local spurs. (a) field 5; (b) field 14; (c) field 16; (d) field 17; (e) field 18. Compare these with the default mode predictions in Fig. 1b, h, j, k and l, respectively.

latitudes ensure that galaxies provide negligible contamination of the stellar counts. These figures portray the differential source counts in the form of  $\log N$  ( $\text{mag}^{-1} \text{ degree}^{-2}$ ) against [1660], the FAUST magnitude. In all cases, we have computed the FAUST counts over a square subset, centered on the original target area, that is fully sampled by the observations and have scaled the counts per square degree. The model was always run for a 1 square degree patch at the central position of these square regions. In the following discussion one should note that typical fields contain roughly 100 FAUST sources distributed into about 10 mag bins. Therefore, random errors due to Poisson uncertainty can attain about 30%, or 0.12 dex.

We find excellent matches to predicted differential counts for fields 2, 8, 9, 10, 11, 13, and 15, i.e., the predicted curve for total count falls centrally through the observed counts to within about  $\pm 0.15$  dex. These are conspicuously the high-latitude fields ( $|b| > 44^\circ$ ) and all were run using the model's default mode (without enhanced populations in the local spurs).

The remaining five fields are at lower latitudes and show various degrees of discrepancy when compared with the default model. We now describe how these fields can be better modeled. Field 5 is our lowest latitude comparison field. The same basic model yields a satisfactory match (Fig. 1b) although most of the observations lie about 0.1 dex above the predicted "total" count. In field 14 the basic model (Fig. 1h) predicts some 3 times as many stars as we actually detect, yet the galactic latitude is not low ( $22^\circ$ ). Field 16, toward M83, also shows that the default model (Fig. 1j) overpredicts the observations by an average factor of  $\sim 2$ , at  $b = 34^\circ$ . Field 17 samples the dense  $\rho$  Oph clouds lying just above the Galactic plane. The degree of obscuration internal to those clouds can be appreciated from Fig. 1k where the default model predicts about 4 times as many stars as are actually observed. Field 18 targets the globular cluster NGC 6752. The default prediction (Fig. 1l) is slightly above the observed counts except in the magnitude range  $[1660] = 9-12$  where it peaks a factor of 3-5 above the

FAUST counts. (We note for the benefit of other modelists of the FAUST sky that while SKY's predictions are quite insensitive to exact galactic direction on a scale of about  $0.5^\circ$ , the FAUST number counts are very sensitive on this same scale.)

We can achieve very good matches (well within a few hundredths of a dex) to FAUST counts in all these five lower latitude fields when we allow ourselves to boost the disk and spiral arm components of stellar population in the local spurs (only in the local spurs do we enhance these populations above their norm) and also to posit extra associated extinction within these same lines of sight through the spurs. Figure 2a-e illustrate these improved predictions. All correspond to disk and arm populations in the local spurs that are boosted so as to mimic best the mid-infrared sky as portrayed by *IRAS* (Cohen 1994). The factors by which the expected extinction should be multiplied in order to obtain these improved far-ultraviolet predictions that match FAUST so well are: field 5, 4.0; field 14, 6.0; field 16, 7.3; field 17, 4.0; and field 18, 4.3. Note that these are multiplicative factors, not the total extinctions. The actual  $A_{1660}$  may be quite small along these lines of sight even after boosting in this fashion, and two lines of sight with identical factors can have very different  $A_{1660}$  values.  $A_{1660}$  is 7.78 times  $A_V$  (Carnochan 1982) or about  $3.4 \text{ mag kpc}^{-1}$  in the Galactic plane. Within the local spurs this quantity is larger than the normal value, although it still diminishes perpendicular to the plane as an exponential with a 100 pc scale height. Even for an enhancement by a factor of 7, the actual length along the line of sight over which  $A_{1660}$  is elevated is never more than 300 pc (even at latitude zero). Therefore, the maximum local extinction,  $A_V$ , attributable to such a clump is  $\sim 10$  mag, not unreasonable for a molecular cloud core. More typical extinction boosts of  $\sim 4$  would correspond to cloud cores with total obscuration of  $A_V \sim 6$  mag, readily attained in the CMa OB1 and  $\rho$  Oph clouds sampled by fields 5 and 17. Along a line of sight at nonzero latitude, the absolute incremental contribution decreases stepping along a ray because the  $z$ -distance



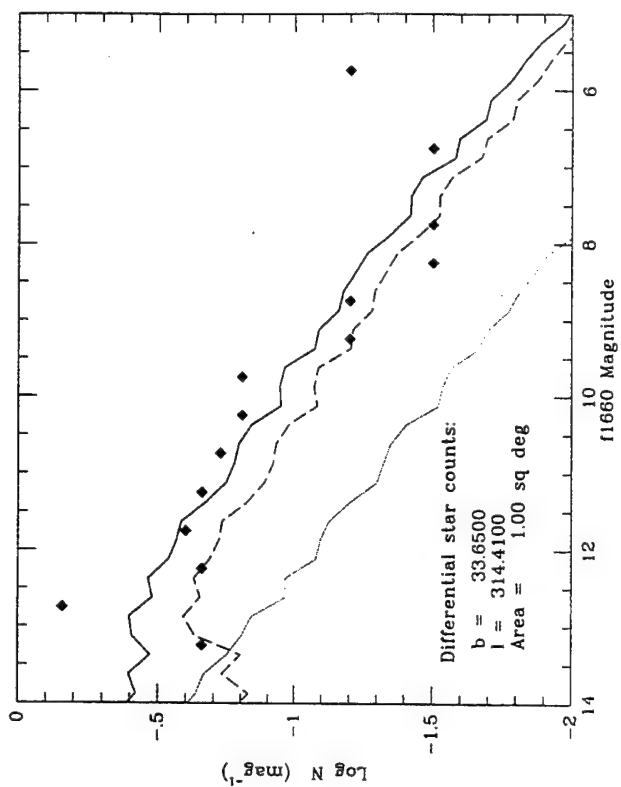


FIG. 2c

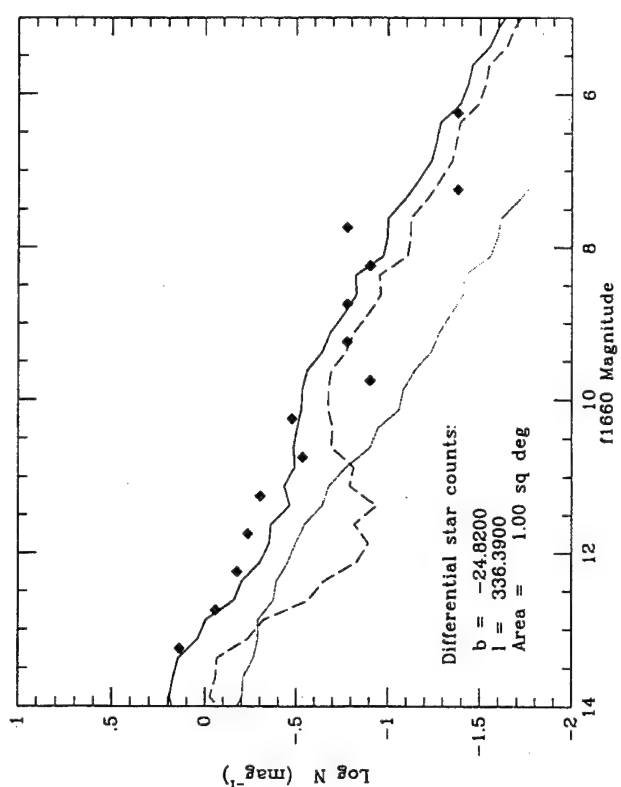


FIG. 2e

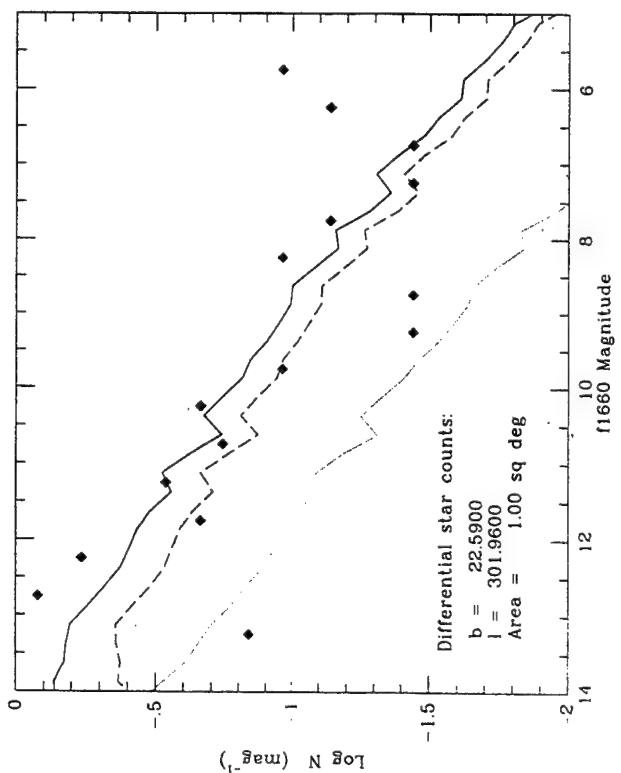


FIG. 2b

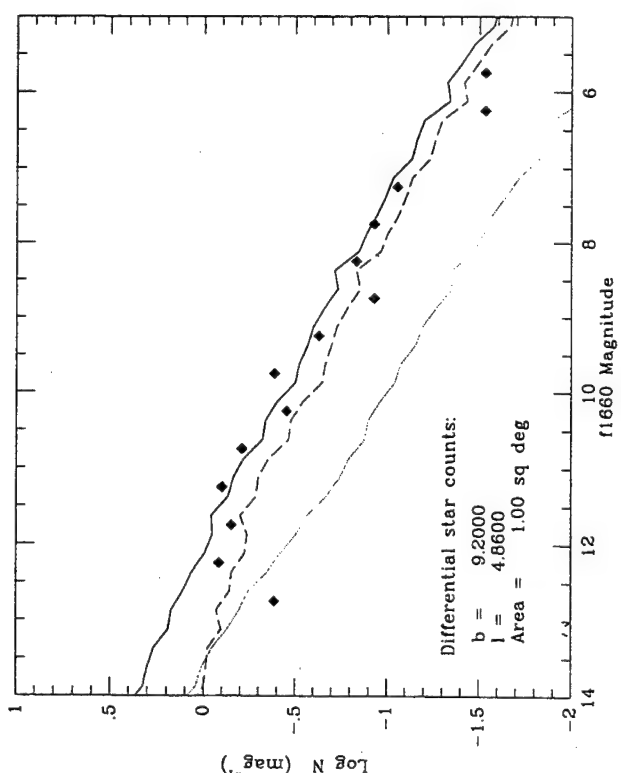


FIG. 2d

increases, even though the extinction is always increased by the same factor over WCVWS's simple expression.

By using the model in these two modes, either without intervention (most appropriate at high latitudes) or as a probe of extinction for FAUST using the enhanced populations' method that best matches the mid-infrared sky (most appropriate at low latitudes), we have achieved matches to the FAUST data that show a mean deviation in  $\log N$  of only  $-0.01$  dex over all 12 fields modeled (the standard error of this mean is only  $0.02$  dex).

### 5. THE DIFFUSE FAR-ULTRAVIOLET BACKGROUND DUE TO STARS

SKY can also provide an estimate in any direction of the total integrated surface brightness due to all the point sources seen in that direction (either in a finite area within specified bounds or for the default 1 square degree area). We have used SKY with this option to assess the contributions to diffuse background light due to stars unresolved and below the FAUST detector threshold. We analyzed all 12 fields and totaled all the in-band flux observed by FAUST in the form of well-detected stars (galaxies were removed) above the threshold for approximate completeness ( $6 \times 10^{-14}$  ergs s $^{-1}$  cm $^{-2}$  Å $^{-1}$ ; Bowyer et al. 1993) but below the flux level at which the FAUST photometric response ceases to be linear (approximately 25 times brighter than the completeness limit). These limiting fluxes correspond to [1660] magnitudes of 11.88 and 8.40, respectively. We then compared the cumulative growth of surface brightness according to SKY as a function of magnitude in essentially the identical magnitude range (12.00–8.50). These slightly different magnitude ranges for SKY and FAUST should yield identical estimates for integrated surface brightness because most ( $\log N$ ,  $\log S$ ) curves have slope of  $-1$ , so the interval between magnitudes 8.38 and 8.50 contributes as much surface brightness as that between 11.88 and 12.00. One might expect a systematic offset because the model's hard-wired value of in-band flux for zero magnitude may not accord precisely with the empirical approach to establishing the flux density, hence magnitude, scale in analysis of the FAUST data. (For SKY's purposes, the in-band flux for a zero magnitude star is simply the product of the monochromatic specific intensity for such a star multiplied by the half-power bandwidth, estimated as 304 Å, of the FAUST passband.) Table 2 tests for this offset by tabulating the ratio of model-estimated surface brightness to that observed by FAUST.

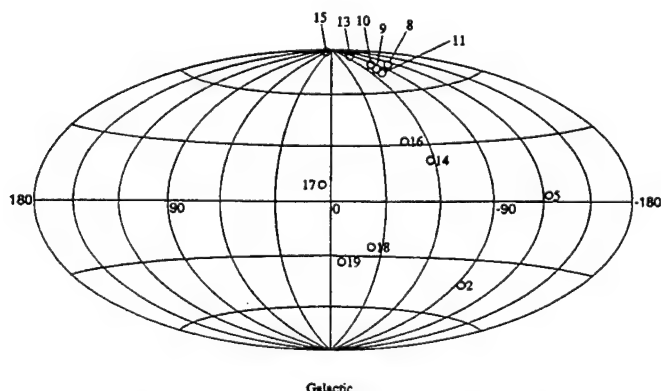


FIG. 3.—Aitoff projection map locating the 13 FAUST fields we discuss. The Galactic center is at the center of the map and longitudes are labeled, as are the fields with their FAUST target numbers.

TABLE 2

SURFACE BRIGHTNESS CALIBRATIONS IN FAUST TARGET FIELDS<sup>a</sup>

Field	FAUST-SB	Model-SB	Model/FAUST
2	1.02E-13	5.36E-14	0.53
5	1.18E-12	4.63E-13	0.39
8	3.12E-14	2.73E-14	0.88
9	2.46E-14	2.81E-14	1.14
11	4.43E-14	2.89E-14	0.65
13	3.84E-14	2.62E-14	0.68
14	1.25E-13	6.08E-14	0.49
15	3.63E-14	2.58E-14	0.71
16	9.39E-14	4.29E-14	0.46
17	3.19E-13	1.34E-13	0.42
18	2.35E-13	1.01E-13	0.43
19	1.23E-13	1.01E-13	0.82

<sup>a</sup> Units are (W m $^{-2}$  deg $^{-2}$ ). Columns indicate the in-band flux observed by FAUST between 8.5 and 12.0; that estimated by the model; and their ratio.

Field 10 was dropped because, after correction for galaxies, there are too few stars in the sampled magnitude range to derive a meaningful estimate of surface brightness. Field 19 (Telescopium) was added because it lies in a direction where the galactic structure is simple and could be modeled by the default mode of SKY.

The average ratio of SKY's prediction for integrated surface brightness due to stars between [1660] = 8.5 and 12.0 and that actually observed by FAUST in the same selected areas is  $0.63 \pm 0.07$ . There is apparently a systematic difference between fields modeled using the default mode and those treated with extra populations and extinction. Seven fields modeled with the default mode yield an average of  $0.77 \pm 0.07$ ; five treated with extra extinction give an average of  $0.44 \pm 0.02$ . However, in all cases, Poisson statistics dominate both the observations and the model's estimates. Changing the number of magnitude 8.5 stars within any region by 1 has an appreciable effect on the assessed surface brightness so these apparent differences between modes of calculation may be purely infelicitous. All dispersions are quite small and suggest that we can readily rescale SKY's surface brightness calculations (by 1.29 based on an assessment of all 12 fields in Table 2) to bring them into line with those actually observed by FAUST.

The model shows that FAUST detects virtually all of the stellar flux as point sources. The in-band flux in undetected stars below this threshold is about 25% of that observed between magnitudes 8.5 and 12.0, and about 4% of the total FAUST stellar brightness (between [1660] = 5 and 12). The latter value is somewhat latitude dependent, falling as low as 3% at the Galactic poles, and rising as high as 7% in the plane. However, the smeared stellar surface brightness, both observed and extrapolated, is less than 1% of the diffuse background detected by FAUST in any field. Quantitatively, at high latitudes this unobserved stellar contribution is about  $6 \times 10^{-15}$  W m $^{-2}$  deg $^{-2}$  (e.g., for fields 13 and 15); at intermediate latitudes (e.g., field 14),  $1 \times 10^{-14}$ ; at low latitudes (e.g., fields 17 and 5) it attains values between  $4 \times 10^{-14}$  and  $1 \times 10^{-13}$  W m $^{-2}$  deg $^{-2}$ .

### 6. PREDICTIONS FOR STELLAR CONTENT AT DIFFERENT GALACTIC LATITUDES

One of the optional output files from the SKY model is a cumulative breakdown of the disposition of stars predicted in any field among their 87 source categories and among the five distinct Galactic components. We ran this option for field 13

and predicted the number of stars whose spectral types fall in the range B8–F8 V, down to various FAUST limiting magnitudes. Virtually all the stars we predict are A or F dwarfs. Brosch et al. (1994) have studied 64.8 square degrees of field 13 near the north Galactic pole in detail. They have spectroscopically observed 83 sources in this field in order to determine stellar types.

They found seven white dwarfs and four galaxies, but the bulk of the optical counterparts were dwarfs (or subdwarfs) from type A to F. Source counts based on their Table 2 suggest a sample with FAUST completeness to  $[1660] \sim 13$  although the uncertainties in this magnitude can be quite large (most are  $\leq 0.35$  mag). We wish to “calibrate” SKY’s predictions for the north Galactic pole using these observations by Brosch et al., because the completeness limits for optical identifications of FAUST sources, obtaining adequate spectra, and assigning spectral types will vary with spectral type. We have treated all luminosity classes as V when none were given, and omitted those stars whose magnitude errors exceed 0.35 mag.

In terms of SKY’s source categories, our best match to Brosch et al. comes from a prediction for a formal limiting magnitude of  $[1660] = 13.25$ ; namely, five stars B8–A0 V; 18 A2–5 V; 19 F0–5 V; and one F8 V. The corresponding breakdown for Brosch et al. to  $[1660] = 13.00$  is four B8–A0 V; 18 A2–5 V; 18 F0–5 V; and four F8 V. The accord is excellent given the Poisson uncertainties.

Table 3 provides our predictions for three very different galactic directions based upon a formal limit of  $[1660] = 13.25$ . We selected FAUST fields 5, 14, and 13 (in order of increasing galactic latitude) and have tabulated the number of sources of each type per square degree in these three directions, focusing again on the dominant stellar categories.

We note that our model does not explicitly include white dwarfs nor those ultraviolet-bright phases of either evolved post-AGB stars or horizontal branch stars. Brosch (1991) found that white dwarfs represented at most a 10% contribution to main-sequence and giant stars, even at the Galactic poles. The good far-ultraviolet performance of our model in spite of its neglect of white dwarfs is, therefore, no surprise. Post-AGB evolutionary phases are even shorter lived than the corresponding AGB phases so any far-ultraviolet bright stars on the horizontal branch should be negligible. This is in accord with Rocca-Volmerange & Guiderdoni (1987), who found that horizontal branch stars at 2000 Å contribute only minimally to a galaxy’s brightness.

TABLE 3

SURFACE DENSITIES TO  $[1660] = 13.25$  FOR A–F DWARF STARS  
WITH DIRECTION

Field	B8–A0V	A2–5 V (stars per sq. deg.)	F0–5 V	F8 V	Information Source
5 .....	3.06	2.30	0.38	0.01	SKY prediction
14 .....	0.20	0.12	0.07	0.01	SKY prediction
13 .....	0.07	0.28	0.30	0.01	SKY prediction
13 .....	0.06	0.28	0.28	0.06	Brosch et al. (1994)

## 7. CONCLUSIONS

We conclude that Cohen’s (1994) model, customized for application to the FAUST bandpass, provides an excellent match to the observed FAUST counts. This simultaneously increases our confidence in the far-ultraviolet capability and realism of SKY, and demonstrates the inherent value of the FAUST data set that extends down more than an order of magnitude below the reliable limiting fluxes of *TD-1*. Our primary findings are as follows.

1. The far-ultraviolet sky seen by FAUST is well-modeled with a population consisting of normal stellar types between B and F.
2. Enhanced extinction is necessary to model low-latitude fields where the line of sight penetrates molecular clouds associated with the local spiral spurs. Typical FAUST low-latitude lines of sight require extinctions to be increased by about 5 over the simple double exponential expression used by WCVWS.
3. Within its completeness threshold of  $6 \times 10^{-14}$  ergs s $^{-1}$  cm $^{-2}$  Å $^{-1}$ , FAUST detects 96% or more of the flux due to stars, and the residual starlight makes up less than 1% of the diffuse flux in any field.

Past development of the SKY model was supported by the US Air Force Phillips Laboratory through Dr. Stephan D. Price under contract F19628-92-C-0090 with JS&E, Inc. M. C. thanks NASA Ames Research Center for partial support at Berkeley through cooperative agreement NCC 2-142. This research is supported in part by NASA contract NAS 8-32577 and the CNES Science Program. S. B. acknowledges support from the John Simon Guggenheim Memorial Foundation, and the assistance of M. Lampton and X. Wu. We thank the referee, Dick Henry, for a careful reading of the paper and for his helpful suggestions.

## REFERENCES

- Bahcall, J. N., & Soneira, R. M. 1980, *ApJS*, 44, 73  
 Bless, R. C., & Savage, B. D. 1972, *ApJ*, 171, 293  
 Bowyer, S., Sasseen, T. P., Lampton, M., & Wu, X. 1993, *ApJ*, 415, 875  
 Brosch, N. 1991, *MNRAS*, 250, 780  
 Brosch, N., Almozino, E., Leibowitz, E. M., Netzer, H., Sasseen, T., Bowyer, S., & Lampton, M. 1994, preprint  
 Carnochan, D. J. 1982, *MNRAS*, 201, 1139  
 Cohen, M. 1993, *AJ*, 105, 1860, 1993  
 ———. 1994, *AJ*, 427, 582  
 Hayes, D. S., & Latham, D. W. 1975, *ApJ*, 197, 595  
 Henry, R. C. 1977, *ApJS*, 33, 451  
 Johnson, H. L. 1965, *ApJ*, 141, 941  
 Kurucz, R. L. 1991, in *Stellar Atmospheres: Beyond Classical Models*, ed. L. Crivellari, I. Hubeny, & D. G. Hummer, NATO ASI Series (Dordrecht: Kluwer), 440–448  
 Page, T., Carruthers, G. R., & Heckathorn, H. M. 1992, *NRL Rep.* 8487  
 Rocca-Volmerange, B., & Guiderdoni, B. 1987, *A&A*, 175, 15  
 Wainscoat, R. J., Cohen, M., Volk, K., Walker, H. J., & Schwartz, D. E. 1992, *ApJS*, 83, 111 (WCVWS)

## THE DISPLACEMENT OF THE SUN FROM THE GALACTIC PLANE USING IRAS AND FAUST SOURCE COUNTS

MARTIN COHEN<sup>1</sup>

Jamieson Science and Engineering, Inc., 5321 Scotts Valley Drive, Suite 204, Scotts Valley, CA 95066

Received 1994 September 15; accepted 1994 November 18

### ABSTRACT

I determine the displacement of the Sun from the Galactic plane by interpreting *IRAS* point-source counts at 12 and 25  $\mu\text{m}$  in the Galactic polar caps using the latest version of the SKY model for the point-source sky (Cohen 1994). A value of  $z_{\odot} = 15.5 \pm 0.7$  pc north of the plane provides the best match to the ensemble of useful *IRAS* data. Shallow *K* counts in the north Galactic pole are also best fitted by this offset, while limited FAUST far-ultraviolet counts at 1660 Å near the same pole favor a value near 14 pc. Combining the many *IRAS* determinations with the few FAUST values suggests that a value of  $z_{\odot} = 15.0 \pm 0.5$  pc (internal error only) would satisfy these high-latitude sets of data in both wavelength regimes, within the context of the SKY model.

**Subject headings:** Galaxy: structure — infrared: stars — Sun: general

### 1. INTRODUCTION

About 50 years ago, it was recognized that there is a slight asymmetry between star counts at the north and south Galactic poles (NGP and SGP). If one assumes that the Galaxy is a smooth symmetrical entity (i.e., that essentially only a disk is observed), this asymmetry can be attributed to a location of the Sun off the Galactic plane, which is the plane of greatest star densities. Van Tulder (1942) derived a location  $+13.5 \pm 1.9$  pc (north of the plane) for the Sun from analyses of several different types of star. Contemporary estimates differ both from one another and, in some cases, from this early estimate according to the type of object examined, but all lie in the range 4–40 pc. Some individual estimates (with their basis) are:  $+4 \pm 12$  (H I; Gum, Kerr, & Westerhout 1960),  $+7$  (Ratnatunga, Bahcall, & Casertano 1989),  $+10 \pm 4$  (dust; Pandey & Mahra 1987),  $+22 \pm 2$  (Population I; Blaauw et al. 1960),  $+26 \pm 20$  (Wolf-Rayets; Stenholm 1975),  $+36 \pm 6$  (Cepheids; Caldwell & Coulson 1987), and  $40 \pm 3$  pc (faint red stars of the halo; Yamagata & Yoshi 1992). Ratnatunga et al. (1989) found a value as large as 30 pc unacceptable within the context of the IAS-Galaxy model.

Infrared counts sample different stellar populations than optical or radio and, therefore, offer a valuable complementary perspective on the value of  $z_{\odot}$ . Hammersley et al. (1994) have recently determined a value of  $15.5 \pm 3$  pc for  $z_{\odot}$  on the basis of the ratio of 2  $\mu\text{m}$  star counts slightly above and below the Galactic plane, taken from the new survey of the plane by Garzon et al. (1993). Their estimate comes from treating the Galaxy as simply a disk and is supported by use of low-latitude *IRAS* source counts and DIRBE surface brightness.

In previous papers (Cohen 1994; Cohen, Sasseen, & Bowyer 1994) I have described a significantly enhanced new version of SKY, the model for the point-source sky originally developed by Wainscoat et al. (1992, hereafter WCVWS). In particular, SKY now offers a faithful representation of the *IRAS* sky, by virtue of its detailed geometry and comprehensive census of celestial sources. This infrared fidelity suggests that SKY can

play a role in determining  $z_{\odot}$ , without the need for artificial simplifying assumptions about the geometry of the Galaxy.

In the present paper, I apply a modified version of the new SKY model that can incorporate a solar location arbitrarily displaced in the  $z$ -direction from the Galactic plane, and I interpret *IRAS* source counts observed in the regions of the sky traditional for study of the solar displacement, namely, the Galactic poles. The influence of  $z_{\odot}$  can most readily be discerned at the NGP and SGP where one sees essentially only disk and halo. A purely mid-infrared-based determination of  $z_{\odot}$  is possible because the ratio of halo to disk counts is small at 12/25  $\mu\text{m}$  (approximately 0.01 at the *IRAS* Point Source Catalog [PSC] completeness limits of [12] = 5.0 and [25] = 4.0). There is greater sensitivity to the halo at optical wavelengths, where the ratio halo:disk = 1:1 at about  $V = 19$ , and therefore greater difficulty in using optical counts to assess  $z_{\odot}$  directly. I will first examine the relative proportions of halo and disk using a data set for the NGP at  $V$  assembled by Bahcall & Soneira (1984), then proceed to the mid-infrared analysis. I augment these *IRAS* Galactic polar counts by an examination of those at the north ecliptic pole (NEP) (*IRAS*'s deepest survey, due to Hacking & Houck 1987), and for the NGP at  $K$  and at 1660 Å.

### 2. A REDETERMINATION OF THE RELATIVE CONTRIBUTIONS OF HALO AND DISK

WCVWS present a comparison of the counts predicted by the first version of SKY at the NGP in  $V$  (their Fig. 13). From this one can see that their halo component was actually somewhat too large, assuming no contamination of the Bahcall-Soneira star counts by galaxies at the faintest magnitudes. WCVWS used a halo:disk normalization factor of 1:500 (adopted from Bahcall & Soneira 1984), within the estimated uncertainties obtained by Schmidt (1975), who derived a best value of 1:800 with rough probable range 1:550 to 1:1200. Bahcall, Schmidt, & Soneira (1983) similarly deduced ratios between 1:200 and 1:1500. Any renormalization of the halo within SKY primarily affects the deepest, high-latitude, optical predictions rather than those in the mid-infrared. The effects at  $K$  are intermediate between those at  $V$  and in the mid-infrared,

<sup>1</sup> Also Radio Astronomy Laboratory, University of California, Berkeley.

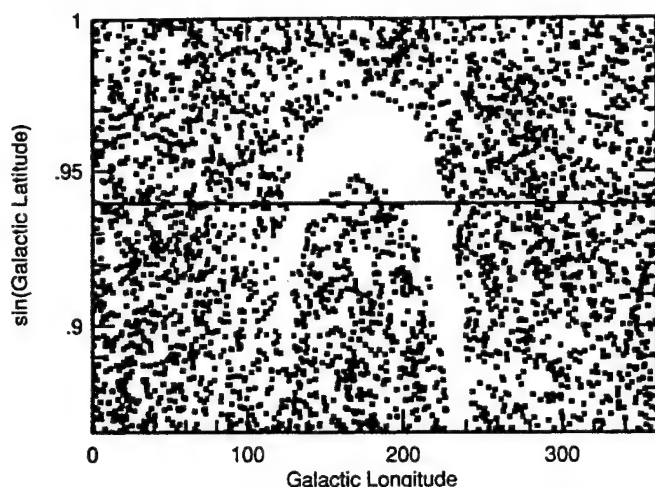


FIG. 1.—NGP coverage by *IRAS*: every object in the PSC with  $b > 60^\circ$  is plotted. Horizontal line corresponds to  $b = 70^\circ$ .

but with the increasing availability of wide-field deep surveys with large-format near-infrared array cameras, such a rescaling is appropriate. Indeed, analysis of deep unpublished  $K$  counts at high and intermediate altitudes (Wainscoat 1993) already results in a similar conclusion: that one needs to reduce the influence of the halo relative to that of the disk. This change in the halo's contributions to star counts has only a very small effect on predictions at 12 and 25  $\mu\text{m}$ , but to leave the halo less than satisfactory at  $V$  would undoubtedly perturb the inherent great sensitivity of SKY to the value of  $z_\odot$  when interpreting *IRAS* source counts.

Within the context of the SKY code, I find that a better scaling is between 40% and 50% of that described by WCVWS, or a number density ratio of halo:disk of 0.0008 (1:1250), at the lower bound of Schmidt's suggested approximate range, but within that determined by Bahcall et al. (1983).

### 3. MAPPING THE *IRAS* "HOLES" AT THE GALACTIC POLES

The *IRAS* unobserved area crosses both polar caps, and an accurate estimation of the areal coverage factor is a prerequisite for this investigation. Figures 1 and 2 illustrate *IRAS*'s polar coverage by plotting *all* sources in the PSC in the north and south Galactic caps, respectively. These diagrams clearly delineate the regions not covered by *IRAS*. The ordinate is  $\sin b$  so that equal areas are represented equally at all latitudes. I assume that the intrinsic distribution of *IRAS* sources is uniform in the "holes" and that the source densities on either side are representative of that in the actual holes. The heavy horizontal line crossing each diagram represents the value of  $\pm \sin 70^\circ$ ; the extreme values on the y-axes correspond to  $|b| = 60^\circ$  and  $90^\circ$ .

Table 1 results when these assumptions are applied to Figures 1 and 2. Note that if a fraction  $\xi$  of an area was

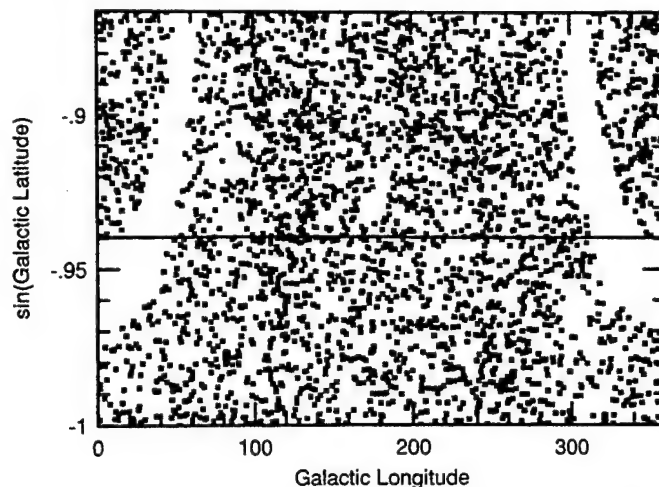


FIG. 2.—SGP coverage by *IRAS* for  $b < -60^\circ$ . Horizontal line is  $b = -70^\circ$ .

unobserved by *IRAS* then the comparison with SKY's predictions should be with the observed *IRAS* source counts multiplied by  $1/(1 - \xi)$ . Approximately 10% of each Galactic cap was unobserved by *IRAS*.

### 4. THE OBSERVED SOURCE COUNTS

At 12  $\mu\text{m}$ , a total cumulative count toward the two poles of  $\geq 1000$  sources can be achieved by analysis of the area with  $|b| > 70^\circ$  in the PSC. At 25  $\mu\text{m}$ , the reduced observed source density makes  $|b| > 60^\circ$  more appropriate. There are *IRAS* data in the Faint Source Survey (FSS) that can provide completeness to somewhat fainter flux density levels than the PSC. Therefore, I extracted FSS counts in the Galactic poles, based on version 2.0 of the FSS (on the NSSDC CD-ROM). Note that the FSS suffers essentially the same percentages of outage as does the PSC (Moshir 1994).

Finally, to extend the *IRAS* counts to the faintest possible levels, I used the Hacking & Houck (1987, hereafter HH) deep *IRAS* survey of the NEP, an intermediate Galactic latitude field. HH have distinguished between stars and galaxies. SKY offers a separate mode in which counts of external galaxies are not calculated, making this appropriate for comparison with HH "stars-only" counts.

### 5. COMPARISON WITH SKY PREDICTIONS

SKY is sufficiently sensitive to  $z_\odot$  that there is no formal reason to collapse the number of independent *IRAS* data sets by treating only ratios of northern and southern counts (cf. Hammersley et al. 1994). Consequently, the technique used was to run a series of SKY predictions differing only by 1 pc in their input value of  $z_\odot$ , then to compare the predicted counts with those separately observed at 12 and 25  $\mu\text{m}$ , for the NGP and SGP, analyzing both differential and cumulative counts. The best match to any data set was evaluated using statistical criteria, thus determining the value of  $z_\odot$  corresponding to the closest match. If the observed asymmetry in *IRAS* source counts were really caused by an offset of the Sun from the Galactic plane, then a common value of  $z_\odot$  should result from all these analyses.

Figure 3 illustrates detail from an enlarged view of a typical series of SKY predictions, compared with the NGP at 12  $\mu\text{m}$  from the FSS. The sensitivity to  $z_\odot$  is quite clear for this grid

TABLE 1  
*IRAS* "HOLES": VALUES OF  $\xi$ , AS DEFINED IN THE TEXT

Cap (range of $b$ )	NGP	SGP	Wavelength ( $\mu\text{m}$ )
( $70^\circ, 90^\circ$ )/( $-70^\circ, -90^\circ$ ).....	0.8852	0.8978	12
( $60^\circ, 90^\circ$ )/( $-60^\circ, -90^\circ$ ).....	0.9069	0.8854	25



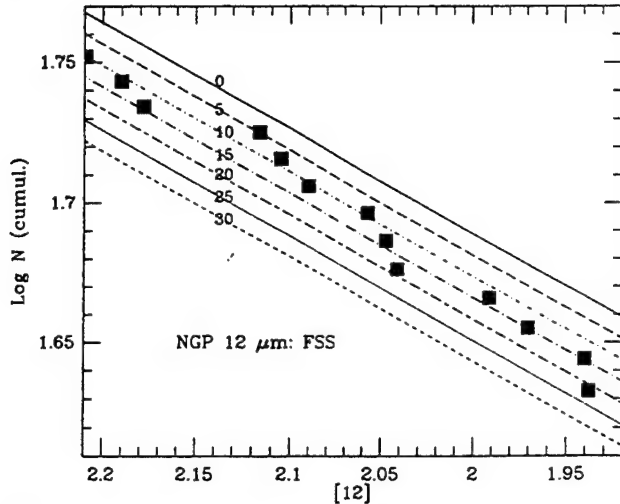


FIG. 3.—Cumulative *IRAS* counts for the NGP at  $12\ \mu\text{m}$  from the FSS (filled squares), boosted by a factor of 1.130 to allow for the area unobserved by *IRAS*. The curves represent SKY predictions for  $z_0 = 0\text{--}30$  pc in 5 pc steps, as labeled. To illustrate the separation of these curves, the detail is shown for the middle of the useful range of *IRAS* data.

with values of 0, 5, 10, 15, 20, 25, and 30 pc. When comparing data sets with SKY one needs to ignore those very few extremely bright sources where the deviation from SKY may be large but the associated Poisson error in the count is enormous. Likewise, one must avoid use of the faintest data bins where conspicuous roll-offs are seen due to incompleteness in the *IRAS* observations. In all comparisons with either differential or cumulative counts, I interpolated the model predictions to the same grid of magnitudes as the observed source counts (the many values actually observed for cumulative counts, and 0.25 mag bins for differential).

Differential counts offer independent counts for each magnitude bin but tend to be noisy. Cumulative counts are far less susceptible to the influence of an errant point but are no longer independent. I did not use a  $\chi^2$  formalism. This is not applicable to cumulative comparisons because it is predicated on the assumption of independent, normally distributed points. It is also inappropriate here for differential counts because, with the Poisson errors (defined above),  $\chi^2$  assigns weights to the terms at the faintest magnitudes that are over two orders of magnitude greater than those at the brightest viable magnitudes (i.e., those with  $\log N \sim 1.0$ ). Such a disproportionate formal bias is unwarranted.

To assess the quality of fit of SKY's predictions to the observed counts, I, therefore, considered three potential criteria: (1) the average algebraic deviation (AD) over the subset of points compared, (2) a weighted version of this average deviation (WAD); and (3) the sum of squared deviations (SSD). Uncertainties in all  $\log N$  quantities were based on Poisson errors,  $N^{1/2}$ , translated into the average of the associated uncertainties in  $\log N$  (i.e.,  $0.5 \log_{10}[(N + N^{1/2})/(N - N^{1/2})]$ ). Consequently, these quantities furnish the weights in the calculation of WAD and of  $\chi^2$ , in the form of the root sum square of the relevant quantities,  $[\epsilon(\text{IRAS})^2 + \epsilon(\text{SKY})^2]^{1/2}$ , in both SKY's predicted counts and the counts observed by *IRAS*.

To make the scheme more concrete, Figure 4 illustrates all three statistics for a common set of data, namely, that represented in Figure 3. All three criteria indicate a value of  $z_0$  close to 15 pc.

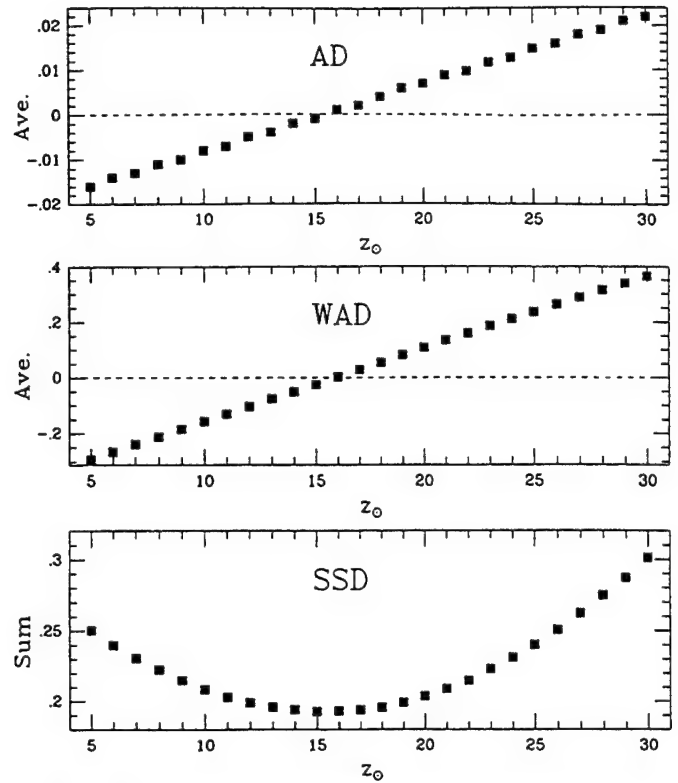


FIG. 4.—Trends of the three statistical estimators used, against value of  $z_0$ . These actually correspond to the data set depicted in Fig. 3.

SKY assumes an extragalactic sky that is intrinsically isotropic (before the application of the total extinction along the actual line of sight). Thus, any appreciable galaxy clustering will invalidate this assumption and result in an unpredictable shape for the curve of total source counts, as opposed to counts excluding galaxies. This is the case at  $25\ \mu\text{m}$ , especially for the SGP (presumably due to local clustering toward Fornax and Eridanus). The influence of galaxies on the total counts is minimal at  $12\ \mu\text{m}$ . Therefore, I also created "galaxy-free" *IRAS* polar counts at  $25\ \mu\text{m}$  using the criterion proposed by Strauss (1994) to exclude galaxies, namely, rejecting all sources having  $S(60)^2/[S(25) * S(12)] \geq 1$ . These samples enabled useful comparisons to be made between galaxy-free *IRAS* counts and the stars-only mode of SKY, in which no galaxy counts are assessed.

Table 2 summarizes these criteria for 14 comparisons of SKY with *IRAS* data sets and presents: the region of the sky considered; whether counts were cumulative (C) or differential (D); the observational catalog from which the *IRAS* counts were drawn; the wavelength; the widest range of magnitudes over which comparisons could be meaningfully made; the values of  $z_0$  for each of the three statistics, and the average of all three values. At the foot of the table are the ensemble averages of the values of  $z_0$  indicated by the criteria, with formal standard-error-of-the-mean (s.e.m.) uncertainties. The best estimate from Table 2, based solely on *IRAS* counts, is the inverse-variance-weighted mean of the three columnar averages of SSD, WAD, and AD, namely,  $15.5 \pm 0.7$  pc. This error is, of course, only internal to the context of SKY. There must also be an essentially unquantifiable systematic uncertainty based upon the representation of the Galaxy inherent in the model. However, the quality of SKY's predictions when compared



TABLE 2  
VALUES OF  $z_{\odot}$  FOR DIFFERENT CRITERIA, COUNTS, AND WAVELENGTHS

Region—C/D <sup>a</sup>	Observational Catalog	$\lambda$ ( $\mu\text{m}$ )	Magnitude Range	SSD	WAD	AD	<All Attributes>
NGP—C .....	PSC	12	-2-2	19.5	14	19.5	18
NGP—D .....	PSC	12	0-4	17	17	14.5	16
NGP—C .....	FSS	12	-2-4	15.5	16	15.5	16
NGP—D .....	FSS	12	0-4	10.5	25	11	15.5
SGP—C .....	PSC	12	-2-4.5	18	11	18.5	16
SGP—D .....	PSC	12	-1-4	22	19	21.5	21
SGP—C .....	FSS	12	-2-4	...	...	22.5	22.5
SGP—D .....	FSS	12	0-3.5	20	14	20	18
NGP—C .....	FSS	25	-1-2.5	12	11.5	13.5	12
NGP—D .....	PSC	25	0.5-3.3	9	15	10.5	11.5
No galaxies							
SGP—C .....	PSC	25	-4-3	13	14.5	13	13.5
No galaxies							
SGP—D .....	PSC	25	-2-3	11	11.5	11.5	11.5
No galaxies							
NEP—C .....	HH	12	5-6	18.5	23	18.5	20
NEP—C .....	HH	25	3-7	9.5	13.5	10.5	11
<All IRAS> .....				15.0	15.8	15.7	15.9
$\pm$ s.e.m. ....				1.2	1.2	1.1	1.0
NGP—C .....	Elias	2.2	1-8.5	17	17	19.5	18
NGP—8 <sup>b</sup> .....	FAUST	0.166	6.7-13.3	21	11.5	19	17
NGP—13 <sup>b</sup> .....	FAUST	0.166	5.7-13.7	13.5	17	14.5	15
NGP—15 <sup>b</sup> .....	FAUST	0.166	5.7-12.7	13	13	9	12
<All FAUST> .....				15.8	13.8	14.2	14.7
$\pm$ s.e.m. ....				2.6	1.6	2.9	1.5

<sup>a</sup> C: cumulative. D: differential.

<sup>b</sup> FAUST field number.

with observed counts and the independent conclusion that  $z_{\odot}$  is close to 15.5 pc by Hammersley et al. (1994) lend credence to the actual value of  $z_{\odot}$  I obtain.

#### 6. NON-IRAS SOURCE COUNTS

In addition to these *IRAS* counts there are other high-latitude counts, for example, at 2  $\mu\text{m}$ . Elias (1978) provides *K* data at the NGP, albeit only to  $K = 8.5$ . SKY's predictions at *K* were also calculated and compared with Elias's counts, as for the *IRAS* counts. Table 2 incorporates these results too. The best formal value is  $\sim 18$  pc, but there are insufficient faint data to determine the value well from this data set (the parabolae or slope lines for residual sums of the appropriate statistics are very shallow).

There are also far-ultraviolet counts from the FAUST experiment, in two separate fields near the NGP. This database has been modeled by Cohen et al. (1994), using an earlier version of SKY. At 1660 Å, SKY predicts a negligible contribution from halo stars toward FAUST fields 13 and 15 (Figs. 1g and 1i of Cohen et al.). The nongalaxy predictions are essentially pure disk, making a determination of  $z_{\odot}$  with FAUST an obvious experiment to attempt because it is independent of the halo:disk normalization discussed above, and because FAUST samples a very different stellar population than that which dominates the counts at infrared wavelengths. The FAUST data set is rather limited, and there is only one other suitably high latitude field with sufficient source counts for this experiment, namely, field 8. These analyses appear at the foot of Table 2. Given a statistically meaningful sample of counts, the

FAUST data appear as useful in constraining  $z_{\odot}$  as are *IRAS* source counts.

#### 7. DISCUSSION

Combining the columnar averages of SSD, WAD, and AD using  $1/(\text{s.e.m.})^2$  weighting solely for the analyses of *IRAS* data in Table 2, I conclude that  $15.5 \pm 0.7$  pc is the best estimate for  $z_{\odot}$ . Such a value also satisfies the currently available (weakly constraining) NGP *K* counts of Elias. Similarly, all three FAUST fields suggest  $z_{\odot}$  is  $\sim 15$  pc, with a formal best estimate of  $14.3 \pm 0.8$  pc, which overlaps the *IRAS* determination at the 1 s.e.m. level. Consequently, one can argue that  $15.0 \pm 0.5$  pc is the best compromise to satisfy data simultaneously in the far-ultraviolet and mid-infrared regimes when using SKY. No systematic uncertainties are included in this small final error.

Neglect of, or use of an inaccurate value for,  $z_{\odot}$  leads to artificial north-south Galactic asymmetries in predicted counts, so recognition of any isotropic near-infrared cosmic background is quite sensitive to this parameter. Indeed, any search for this background radiation is utterly dependent on highly accurate subtraction of both the contributions of sunlight scattered by zodiacal particles and of smeared foreground point sources. Interpretation of DIRBE data already mandates these corrections to the total observed diffuse fluxes (Cohen 1993), and the next infrared satellites will necessitate similar considerations, perhaps most precisely for interpretation of deep *Infrared Space Observatory* measurements. Consequently, the value of achieving a good normalization of halo:disk and

determining  $z_0$  from *IRAS* counts is clear, both to interpret new, deep, near-infrared counts from new large-aperture telescopes equipped with large-format arrays and for future satellite-borne sensors seeking cosmic backgrounds. Although galaxy counts overwhelm stars in the realm of  $K = 20$  (e.g., Cowie, Gardner, & Lilly 1990), significant stellar counts can be achieved from the halo. At levels of  $K = 20$ –24, brown dwarfs might even be detectable (if any exist in abundance). However, recognition of their presence requires that the Galactic geometry and the census of known celestial populations are

already extremely well characterized in the near-infrared and that we already have in place a reliable and accurate point-source sky predictor, such as the SKY model.

I thank US Air Force Phillips Laboratories for supporting these analyses and the development of the SKY model through S. D. Price under contract F19628-92-C-0090 with JS&E, Inc. I am grateful to P. Hammersley for useful discussions and to NASA-Ames Research Center for partial support at Berkeley through cooperative agreement NCC 2-142.

## REFERENCES

- Bahcall, J. N., Schmidt, M., & Soneira, R. M. 1983, *ApJ*, 265, 730  
 Bahcall, J. N., & Soneira, R. M. 1984, *ApJS*, 55, 67  
 Blaauw, A., Gum, C. S., Pawsey, J. L., & Westerhout, G. 1960, *MNRAS*, 121, 123  
 Caldwell, J. A. R., & Coulson, I. M. 1987, *AJ*, 93, 1090  
 Cohen, M. 1993, in *Proc. Workshop on Databases for Galactic Structure*, Swarthmore College, 1993, May 17–19, ed. A. G. Davis Philip, B. Hauck, & A. R. Uppgren (Schenectady, NY: Davis), 131 (also *Van Vleck Obs. Contr.* 13)  
 ———. 1994, *AJ*, 107, 582  
 Cohen, M., Sasseen, T., & Bowyer, S. 1994, *ApJ*, 427, 848  
 Cowie, L. L., Gardner, J. P., Lilly, S. J., & McLean, I. 1990, *ApJ*, 360, L1  
 Elias, J. H. 1978, *AJ*, 83, 791  
 Garzon, F., Hammersley, P. L., Mahoney, T., Calbet, X., Selby, M. J., & Hepburn, I. D. 1993, *MNRAS*, 264, 773  
 Gum, C. S., Kerr, F. J., & Westerhout, G. 1960, *MNRAS*, 121, 132  
 Hacking, P., & Houck, J. R. 1987, *ApJS*, 63, 311  
 Hammersley, P. L., Garzon, F., Mahoney, T., & Calbet, X. 1994, *MNRAS*, in press  
 Harmon, R. T., & Gilmore, G. 1988, *MNRAS*, 235, 1025  
 Moshir, M. 1994, private communication  
 Pandey, A. K., & Mahra, H. S. 1987, *MNRAS*, 226, 635  
 Ratnatunga, K. U., Bahcall, J. N., & Castertano, S. 1989, *ApJ*, 339, 106  
 Schmidt, M. 1975, *ApJ*, 202, 22  
 Stenholm, B. 1975, *AA*, 39, 307  
 Strauss, M. 1994, private communication  
 van Tulder, J. J. M. 1942, *Bull. Astron. Inst. Netherlands*, 9, 315  
 Wainscoat, R. J. 1993, private communication  
 Wainscoat, R. J., Cohen, M., Volk, K., Walker, H. J., & Schwartz, D. E. 1992, *ApJS*, 83, 111 (WCVWS)  
 Yamagata, T., & Yoshi, Y. 1992, *AJ*, 103, 117

## INTERPRETING SURVEYS WITH MODELS

M. COHEN

*University of California, Radio Astronomy Laboratory, 601  
Campbell Hall, University of California, Berkeley, CA 94720,  
USA and Jamieson Science & Engineering, Inc., Suite 204,  
5321 Scotts Valley Drive, Scotts Valley, CA 95066, USA*

**Abstract.** I discuss the interpretation of data from near-infrared surveys using the SKY model, focusing on those aspects of the counts from which one can most rapidly elicit valuable information about Galactic structure. For subtle issues, such as the ratio of halo:disc and the sun's displacement from the Galactic plane, one must know the pixel size and actual area surveyed in a region to better than 1%. I present an absolute calibration of the DENIS passbands, from which it is possible to deduce that any magnitude offsets between standard  $K$  and the DENIS  $K'$  passband are less than about  $0.03^m$  for the types of source so far characterized. I show first results from the newest version of the SKY model.

### 1. Introduction

Typical tools with which to elicit facets of Galactic structure from surveys are star counts, histograms of colours, colour-mag arrays, and profiles of star counts as a function of magnitude and Galactic coordinates. By judicious choice of direction it is possible to emphasize the separate contributions to star counts of the geometric components of the Galaxy, that is, the halo, disc, bulge, spiral arms and local spurs, and molecular ring.

### 2. The Importance of the System Passbands

The "SKY" model (Wainscoat *et al.* 1992; Cohen 1994) is designed with the capability to customise its predictions of star counts and colours specifically for a user's system passbands (*i.e.* the combination of filter transmission profile, site-dependent atmospheric transmission, and detector quantum ef-

ficiency curve). The most rigorous comparisons of a model with counts are based on detailed knowledge of these passbands. As yet we do not know the complete system profiles for DENIS because the wavelength dependence of the focal reducers and other intermediate optics have not yet been characterized and combined with the other elements. However, to make concrete predictions and, in particular, to assess the quantitative error made if one predicts for the "standard"  $K$  filter rather than for the DENIS  $K'$  band, I have constructed absolute calibrations for the DENIS passbands by defining the "zero magnitude" in-band fluxes and the isophotal specific intensities for the combination of detector, filter, and atmosphere in the  $J$  and  $K'$  bandpasses from the La Silla site.

### 3. The DENIS System

By integrating these passbands over the absolutely calibrated Vega model presented by Cohen *et al.* (1992), I characterize the DENIS absolute calibration at  $J$  and  $K'$  as having the following attributes: isophotal wavelengths of 1.226 and 2.164  $\mu\text{m}$ ; isophotal flux densities ( $F_\lambda$ ) of 3.21E-13 and 4.24E-14  $\text{W cm}^{-2} \mu\text{m}^{-1}$ . For the DENIS  $I$ -band, I have only preliminary values, which indicate 0.83  $\mu\text{m}$  and 1.02E-12  $\text{W cm}^{-2} \mu\text{m}^{-1}$ , respectively. At the San Miniato conference (Cohen 1995a), I expressed concern over the potential differences between predictions made for counts in the standard  $K$ -band as compared with model predictions specific to the DENIS and 2MASS  $K'$  band. The issue arose because the definition of zero magnitude involves reference to the spectrum of Vega, whose Br- $\gamma$  absorption affects the  $K'$  band more than the broader  $K$ -band, yet the typical source seen by DENIS at faint levels is a K-giant, whose CO first overtone absorption affects  $K'$  less than  $K$ . These concerns are valid, yet the slightly shorter isophotal wavelength of  $K'$  leads to a larger zero magnitude in-band flux, compared with that for the normal  $K$ . This effect mitigates the others. Consequently, the difference between standard  $K$  and true DENIS  $K'$  is no more than 0.03<sup>m</sup> for most types of celestial source. (This conclusion was reached by comparisons of actual integrations over SKY's spectral library through  $K'$  and  $K$  bands.)  $\Delta(K' - K)$  is much smaller than the typical photometry errors in DENIS photometry; nevertheless, the SKY model is now capable of formal predictions specific to the  $K'-K$  band, for the new (hemispheric) surveys.

*At some point, we will still need the real, complete, system passband profiles for DENIS.*

#### 4. High Latitudes

At high latitudes, there is sensitivity to the ratio of halo:disc, and to the displacement of the sun from the plane ( $z_{\odot}$ ). Although the effect of the former can be subtle, it is possible to extract an optimal ratio of halo: disc at a specified wavelength within an uncertainty of perhaps 10% (cf. Cohen 1995b). For this reason, it is necessary to know very accurately ( $\ll 1\%$ ) one's pixel scale and the area actually surveyed to yield the observed counts. At the Galactic poles, halo and disc contribute equal differential counts for  $K \sim 17.5$ . Nevertheless, one should still achieve useful estimates of halo:disc and  $z_{\odot}$  for surveys with  $J \leq 16$ ,  $H \leq 15$ , and  $K \leq 14$ . From such data, indications are still that  $z_{\odot} \sim 15$  pc (north) and halo/disc  $\sim 1/1000$  (within the context of SKY). Typical surveys are of only  $200''^2$  and it is clear that DENIS and 2MASS offer the opportunity for sharper determinations of these parameters because of their large survey areas, which serve to minimise the Poisson error bars associated with star counts.

If we push to magnitudes below those achieved by DENIS, the total counts' curve at the Galactic poles flattens somewhat, making the comparisons between models and observations less sensitive to errors in the photometry. But if we remain at the achieved levels of completeness of DENIS, the observed star counts are less "contaminated" by galaxies.

It is also important to use the SAME model for a wide variety of wavelengths. SKY's capacity to operate in the far-ultraviolet and optical is, therefore, a major advantage because the counts in each wavelength region highlight rather different types of source.

#### 5. Low Latitudes

One seeks directions in which the counts from bulge, arms, or ring exceed those of the disc. The inner Galaxy provides ample opportunities for contriving such situations, *e.g.* near the Centre at  $K$  and  $L$ . It is also possible to assess the ratio of halo:disc near the Galactic Centre where the inner portion of the halo contributes appreciably to the dominant disc component. This effect is seen in DENIS counts near  $b \sim 15$ ,  $l \sim 350$ .

#### 6. "TMGS"

Following the survey of the Galactic plane to  $K \leq 10$  by Garzon *et al.* (1993), we have undertaken the analysis of almost 600 patches of sky, directly comparing TMGS with SKY's predictions. Most of these areas show very good agreement yet it is important to have formal predictions of what one expects because these amplify even small deviations. A small set of patterns have emerged from these comparisons, which we seek to explain in

terms of either subtle differences in Luminosity Function and/or geometric components of the Galaxy that are lacking from models. TMGS very effectively highlights new “windows” in the plane and distinguishes off-plane obscuring clouds.

### 7. The Value of Colours

While SKY functions extremely well, its results may not be unique. The addition of colour information provides an extra constraint on models. A particular kind of source may occur relatively infrequently so that its contribution to differential counts is minimal, yet it may have a unique colour between two passbands that is an effective diagnostic of the presence of these objects. One can establish the need to include these sources from *IRAS* colours (*e.g.* very late M-giants), estimate their requisite space densities, and test these in another colour *e.g.* DENIS *J-K'*. In this way, colour information constrains the details of models.

### 8. Suggestions for Bright DENIS Nights

There are a number of obvious uses for non-survey (*e.g.* bright moon) DENIS nights. I would suggest the following: photometric calibration (always vital); repetitions and enlargement of structurally interesting areas where geometric components can be isolated, to confirm and enhance their value and to reduce the Poisson errors; revisit fields observed by satellites like *ISO*, to secure vital multi- $\lambda$  coverage and to assess variable stars' behaviour; repeat images of the Magellanic Clouds for variables, and to alleviate *IRAS* confusion; repeat bulge fields for comparison with MACHO and OGLE archives from which one can derive the amplitude( $\lambda$ ) for variable stars.

**Acknowledgements:** The development of the SKY model has been supported by Dr. S. D. Price through Phillips Laboratory.

### References

- Cohen, M. 1994, *AJ*, 107, 582
- Cohen, M. 1995a, *Mem. Soc. Astron. Ital.* 66, 641
- Cohen, M. 1995b *ApJ*, 444, 874
- Cohen, M., Walker, R. G., Barlow, M. J., & Deacon, J. R. 1992, *AJ*, 104, 1650
- Garzón F., Hammersley P. L., Mahoney T., Calbet X., Selby M. J., & Hepburn I. D. 1993, *MNRAS*, 264, 773
- Wainscoat, R. J., Cohen, M., Volk, K., Walker, H. J., & Schwartz, D. E. 1992, *ApJS*, 83, 111



## MSX Observations of Cometary Dust

R. G. Walker (VRI), D. J. Lein (Bucknell Univ.), S. Jayaraman (VRI),  
E. A. Barker(VRI), S. D. Price (AFRL)

### Abstract

We report preliminary results of observations in four infrared bands from 6.8 to 25 microns of comets Hyakutake, Tabur, Hale-Bopp, and Kopff obtained by the Midcourse Space Experiment (MSX) satellite. The line scanned arrays in the infrared telescope have a resolution of 18 arc seconds. MSX observed eight comets, but these are the four that have been examined to date. Each comet observation includes 15 scans along the comet's orbit (1° wide by 3.5° long). The large field scanned combined with the good sensitivity of the detectors and the factor of four co-add advantage from the 15 scans allows us to map the dust to great distances from the comet. Preliminary images are presented and interpreted in terms of dust production rate, emission mechanism, and grain properties by comparison to theoretical models of the dust distribution.

### Introduction

MSX observed eight comets during its mission lifetime; Hale-Bopp, Hyakutake, Kopff, Tabur, IRAS, Wintanen, Tempel-Tuttle, and Spacewatch. We have constructed preliminary images and derived dust production rates for the first four. The infrared telescope (SPIRIT III) aboard MSX observed in the nominal wavebands shown in Table 1, however, the thermal emission from cometary dust is extremely weak in the narrow Bands B1 and B2 and no images were obtained. Thus we present data from only Bands A, C, D, and E.

Table 1. MSX Spectral Bands in the Infrared Region (see Burdick, Chen and Morris, 1997 for detailed spectral response curves).

Band	Bandwidth ( $\mu\text{m}$ )	Isophotal Wavelengths ( $\mu\text{m}$ )
A	6.77 - 10.84	8.28
B1	4.22 - 4.36	4.29
B2	4.24 - 4.45	4.35
C	11.09 -13.20	12.13
D	13.51 - 15.92	14.65
E	18.17 - 25.07	21.41

The circumstances of the observations are given in Table 2. Comets Tabur and Hale-Bopp were observed prior to perihelion passage, while Hyakutake and Kopff were observed post perihelion.

Table 2. Circumstances of the comet observations.  $\rho$  is the heliocentric distance of the comet.  $\Delta$  is the geocentric distance of the comet.  $T_{bb}$  is the equilibrium temperature of a small black isothermal sphere at that heliocentric distance.

COMET	DATE OBSERVED	$\rho$ (AU)	$\Delta$ (AU)	PHASE	$T_{bb}$ (k)
Hale-Bopp	10/07/96	2.82	3.01	19°	165.5
Hyakutake	06/16/96	1.22	1.13	51°	251.7
P/Kopff	09/11/96	1.73	0.91	26°	211.4
Tabur	10/09/96	0.96	0.42	82°	283.7

## Results

Images were constructed in each spectral band for each scan of the comet, the individual scans examined, the sky background (and residual dark offsets) subtracted, and a selected subset of the scans spatially coadded to produce the images shown in Figures 1a through 4d. The images are composed of 18.3'' square detector pixels sampled on 9'' image centers, yielding a spatial resolution of approximately 18''. The full 1° x 3.5° scans are not shown, only that portion containing the comet and its immediate vicinity. To accommodate the large dynamic range of the comet radiance, the image color table has been adjusted to display the 1/5<sup>th</sup> root of the scene radiance.

Aperture photometry was performed on the coadded images, and these results are given in Table 3. The fluxes tabulated are inband fluxes integrated over a 54'' diameter circular aperture centered on the brightest part of the coma. The flux uncertainties,  $\sigma F(i)$ , are the measurement errors combined (in the RSS sense) with the MSX irradiance accuracy given by Howard, et al, 1997. The flux ratios,  $F(i) / F(i+1)$ , are given for the same aperture, however, they are constant for all apertures from 36'' to 72'' diameter. Dust production rates,  $dM/dt$ , were calculated using the steady-state theory of coma emission of Gehrz and Ney (1992) assuming a nominal 1  $\mu$ m particle radius, a grain density of that equal to water, and a Planck mean absorption efficiency of unity. The formal uncertainty in  $dM/dt$  ranges from 20% to 22%. This is probably small compared to the uncertainties introduced by the assumptions inherent in the theoretical simplifications.

Table 3 also shows the flux ratios expected from black grains at the equilibrium temperatures given in Table 2. It is clear from a comparison of these with the observed ratios that a simple blackbody fit will not give a good estimate of the grain temperature. This can be understood by reference to the MSX spectral bands in Table 1. The measurements in MSX Bands A, C, and E are all subject to emission in silicate features, only Band D will measure the blackbody continuum if silicates are present ( see: Gehrz and Ney, 1992; Krishna Swamy, et al, 1989). A detailed grain emission model will be necessary to estimate the grain temperature from these observations. To estimate  $dM/dt$  we have assumed a grain temperature 10% higher than  $T_{bb}$  and used the continuum flux measurement in Band D.

**Hale-Bopp** - Images of comet Hale-Bopp in the four MSX spectral bands are shown in Figures 1a, 1b, 1c, and 1d. Each image covers  $1.043^\circ \times 0.955^\circ$  (417 x 382 image pixels). This is the brightest of the comets observed. Its derived dust production rate,  $dM/dt = 4.9 \times 10^7$  g/s is unusually high for a comet at this heliocentric distance. Evidence for three dust jets is clearly seen in close examination of the coma region. The dark vertical band seen in Figure 1d is due to a saturation anomaly that occurs in the Band E detector array at high irradiance levels (no saturated pixels were used in the coadds). This effect could underestimate the Band E flux by a maximum of 6%.

**Hyakutake** - Images of comet Hyakutake are shown in Figures 2a, 2b, 2c, and 2d. Each image spans  $1.498^\circ \times 1.25^\circ$  (599 x 500 image pixels). Hyakutake has the appearance of having two dust tails, however, this is an effect of the optical thickness variation across a single dust distribution. The faint "tail" extending to the right of the coma is made of grains that were ejected from the nucleus several months prior to those that comprise the main dust tail extending downward in the image. We see a broad fan of material that is separated spatially according to its age. This broad fan has increased the difficulty of background subtraction, as can be seen in the structured residuals. A bright spike is seen extending downward from the coma. This may be due to larger fragments (mini-comets) drifting away from the nucleus. At least one and possibly two dust jets are also seen in the coma under close examination. Again, the dark vertical band seen in Figure 2d is due to a saturation anomaly that occurs in the Band E detector array at high irradiance levels (no saturated pixels were used in the coadds). This could the Band E flux to be underestimated by a maximum of 6%.

Hyakutake was an active dust producer at  $dM/dt = 3.6 \times 10^6$  g/s. This rate at this heliocentric distance is comparable to that of P/Halley and would thus classify it as an IR Type II comet (Gehrz and Ney, 1992) with large continuum superheat and strong silicate features.

**P/Kopff** - Kopff is the only comet of the set that was observed by IRAS. IRAS observed a flux density  $F(12) = 17$  Jy at  $\rho = 1.58$ ,  $\Delta = 0.95$  and  $F(12) = 4.5$  Jy at  $\rho = 1.73$ ,  $\Delta = 1.53$ . Scaling to the MSX circumstances we get  $\sim 14$  and  $12$  Jy for the two observations. The MSX flux density is  $18$  Jy in a similar aperture, comparable to the flux density measured during the IRAS apparition. Walker and Aumann (1984) estimated  $dM/dt = 8.1 \times 10^4$  g/s at  $\rho = 1.73$ . This may be compared to the MSX value of  $1.6 \times 10^5$  g/s measured at the same heliocentric distance. We may conclude that Kopff was somewhat more active (in the sense of dust production) during 1996 than during its 1983 apparition. We would classify Kopff as an IR Type I comet (Gehrz and Ney, 1992).

The Kopff images are shown in Figures 3a, 3b, 3c, and 3d, and span  $0.8975^\circ \times 0.7825^\circ$  (359 x 313 image pixels). A dark patch of sky just to the right of the coma is noticeable in Figures 3a and 3c. This is due to the background subtraction software overestimating the background due to the faint debris trail behind Kopff.

**Tabur** - Figure 4a, 4b, 4c, and 4d, are images of comet Tabur in the four MSX bands. Each image covers  $1.258^\circ \times 1.083^\circ$  (503 x 433 image pixels). No definite jet structure is observed in our images. Tabur's dust production rate of  $dM/dt = 3.7 \times 10^5$  at  $\rho = 0.96$  classifies it as an IR Type I comet (Gehrz and Ney, 1992) that has low continuum superheat and muted or absent silicate emission.

Table 3. Results of aperture photometry.  $F(i)$  is the flux in the  $i$ th MSX spectral band contained within a  $54''$  diameter circular aperture centered on the brightest part of the coma.  $F_{bb}(i) / F_{bb}(i+1)$  is the flux ratio expected for a blackbody at  $T_{bb}$  of the grains.  $dM/dt$  is the dust production rate deduced from the Band D flux and the steady-state theory of coma emission (Gehrz and Ney, 1992).

COMET	MSX BAND	$F(i)$ ( $w/cm^2$ )	$\sigma F(i)$ (%)	$F(i) / F(i+1)$	$F_{bb}(i) / F_{bb}(i+1)$	$dM/dt$ (g/sec)
Hale-Bopp						
	A	$2.92 \times 10^{-15}$	9.5	1.77	0.71	
	C	$1.65 \times 10^{-15}$	7.4	0.98	0.58	
	D	$1.68 \times 10^{-15}$	14.3	0.34	0.37	$4.9 \times 10^7$
	E	$5.00 \times 10^{-15}$	14.1			
Hyakutake						
	A	$6.45 \times 10^{-15}$	9.3	2.26	1.52	
	C	$2.85 \times 10^{-15}$	6.5	1.15	0.86	
	D	$2.49 \times 10^{-15}$	14.2	0.59	0.66	$3.6 \times 10^6$
	E	$4.22 \times 10^{-15}$	13.8			
Kopff						
	A	$1.09 \times 10^{-16}$	11.3	1.47	1.13	
	C	$6.08 \times 10^{-17}$	9.7	0.88	0.75	
	D	$6.90 \times 10^{-17}$	15.6	0.57	0.54	$1.6 \times 10^5$
	E	$1.22 \times 10^{-16}$	14.9			
Tabur						
	A	$2.64 \times 10^{-15}$	11.6	2.41	1.86	
	C	$1.02 \times 10^{-15}$	10.7	0.94	0.95	
	D	$1.09 \times 10^{-15}$	15.4	0.75	0.75	$3.7 \times 10^4$
	E	$1.44 \times 10^{-15}$	15.3			

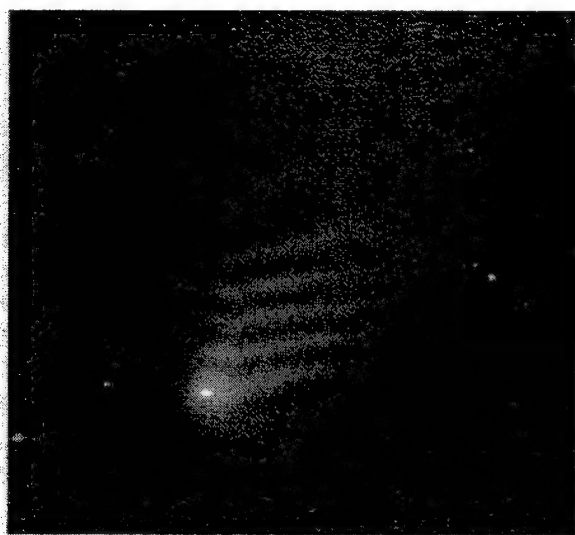


Figure 1a. Hale-Bopp in MSX Band A.



Figure 1c. Hale-Bopp in MSX Band D.

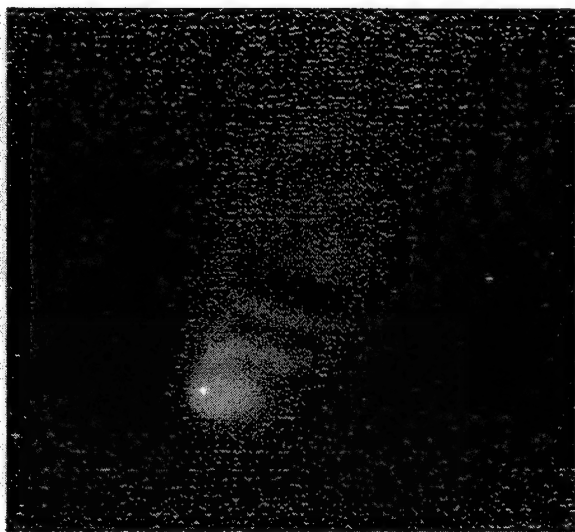


Figure 1b. Hale-Bopp in MSX Band C.

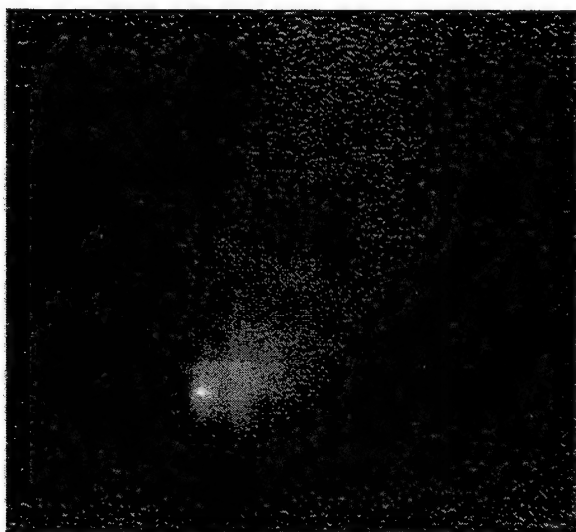


Figure 1d. Hale-Bopp in MSX Band E.



Figure 2a. Hyakutake in MSX Band A.

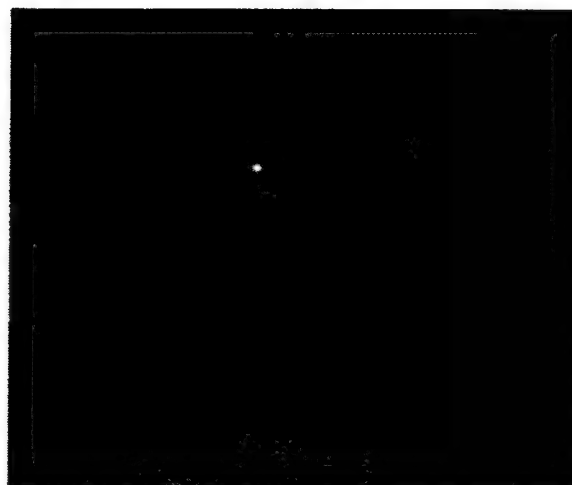


Figure 2c. Hyakutake in MSX Band D.



Figure 2b. Hyakutake in MSX Band C.



Figure 2d. Hyakutake in Band E.



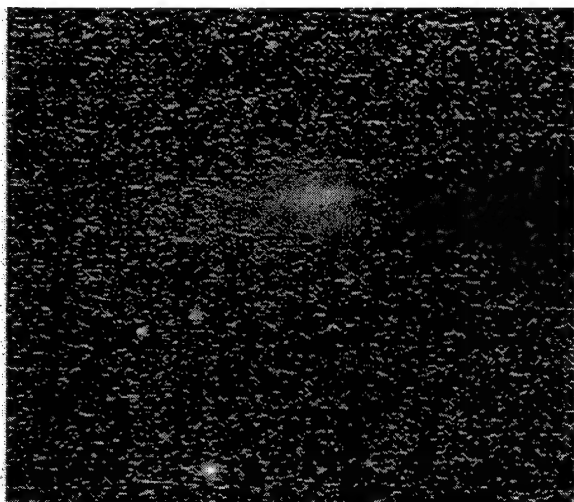


Figure 3a. P/Kopff in MSX Band A.

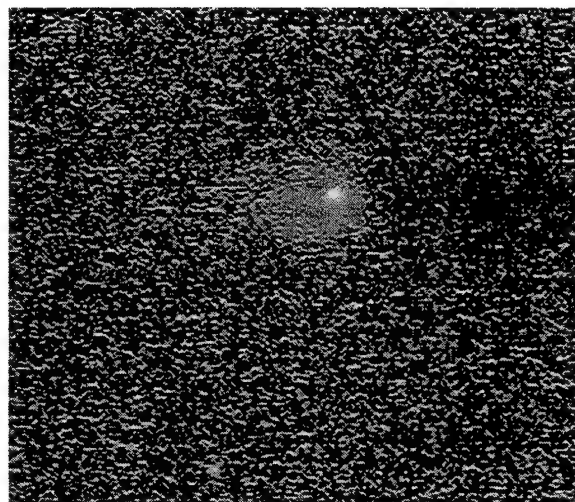


Figure 3c. P/Kopff in MSX Band D.

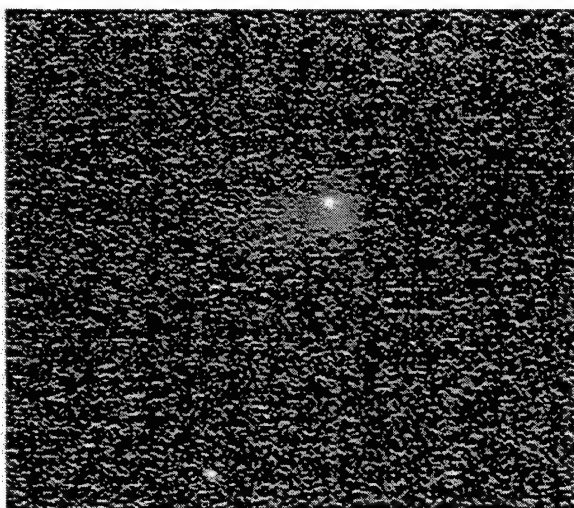


Figure 3b. P/Kopff in MSX Band C.

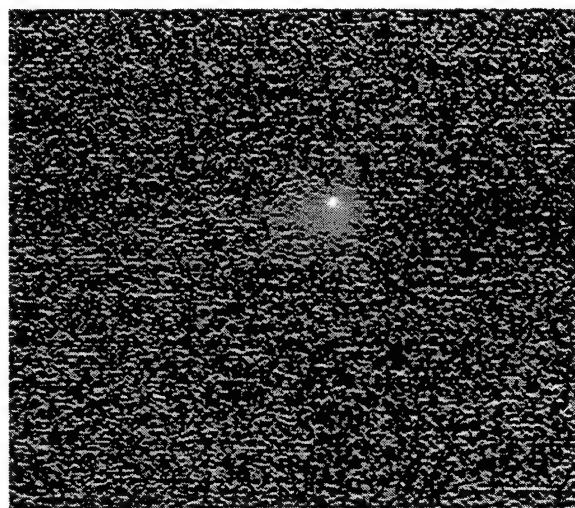


Figure 3d. P/Kopff in MSX Band E.



Figure 4a. Tabur in MSX Band A.

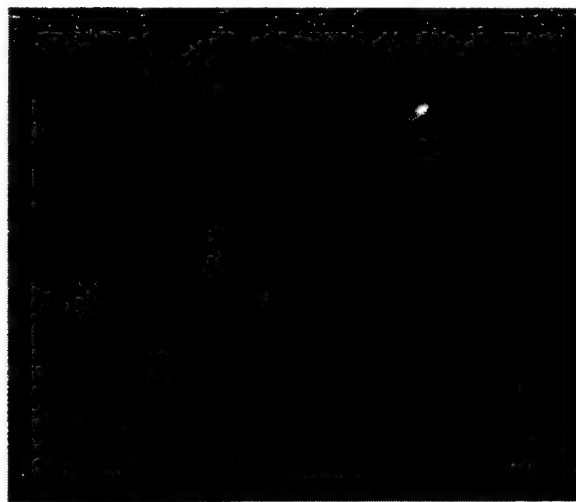


Figure 4c. Tabur in MSX Band D.

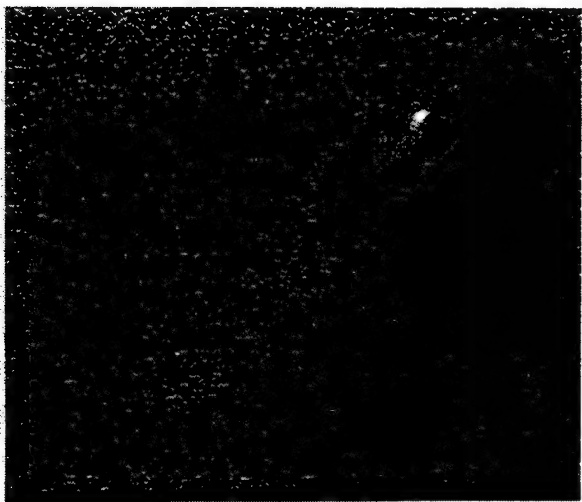


Figure 4b. Tabur in MSX Band C.

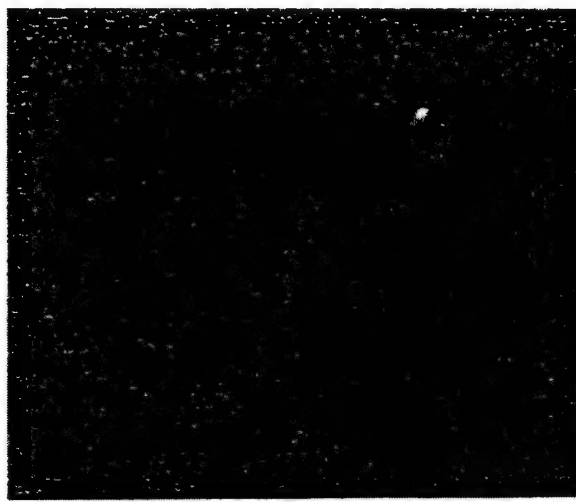


Figure 4d. Tabur in MSX Band E.

### References

- Burdick, S., Chen, G., and Morris, D., 1997, *SPIRIT III Calibration Stars: Inband Irradiance and Uncertainty*, Proc. of the Seventh SDL/USU Symposium on Infrared Radiometric Sensor Calibration (Utah State Univ., Logan, Utah)
- Gehrz, R. D. and Ney, E.P., 1992, *0.7 to 23 $\mu$ m Photometric observations of P/Halley 1986 III and Six Recent Bright Comets*, IRARUS **100**, pp 162-186
- Walker, R.G. and Aumann, H. H., 1984, *IRAS Observations of Cometary Dust*, Adv. Space Res. **4**, no. 9, pp 197,201
- Krishna Swamy, K. S., Sanford, S. A., Allamondola, L. J., Witteborn, F. C., and Bregman, J. D., 1989, *Infrared Emission from Comets*, Astrophys. J. **340**, pp 537-549
- Howard, J., Taylor, S., Morris, D., Mavrofrides, M., and Murdock, T., 1997, *Certification of the MSX SPIRIT III Radiometer Level 2A Data Products*, Proc. of the Seventh SDL/USU Symposium on Infrared Radiometric Sensor Calibration (Utah State Univ., Logan, Utah)

# MSX Observations of the Zodiacal Cloud

S. Jayaraman (VRI), R.G. Walker (VRI) and S.D.Price (AFRL)

## Abstract

Data obtained from the SPIRIT III radiometer, aboard the Midcourse Space Experiment (MSX) satellite, has provided us with new and unique observations of the Zodiacal cloud in four infrared wavebands between 6.8 to 25.1 microns. Zodiacal measurements were obtained on a total of 69 observations over the 10 month cryogen phase of the mission. The observations consist of long scans ( $\geq 135^\circ$ ) at (nearly) constant ecliptic longitude; about two-thirds of these scans include the north ecliptic pole. In aggregate, the scans cover solar elongations between  $25^\circ$  and  $170^\circ$  far larger than the IRAS plus COBE limits of  $64^\circ$  to  $124^\circ$ . Thus, the uniqueness of this data set enables us, for the first time, to systematically probe the dust distribution in the zodiacal cloud, as well as the variation in the structure of the cloud, from the sun to the asteroid belt using data from a single experiment. We present samples of the data from the as ecliptic pole-to-pole scans taken at the smaller elongations.

## References:

1. Dowling, J. M. 1984. '*Estimating the Non-Rejected-Earth-Radiance, NRER, Background for Infrared Sensors*', In Proceedings of the Tri-Service Infrared Background Symposium, (R. E. Murphy and T.D. Eds), AFGL-TR-84-0094, pp. 97-104.
2. SPIRIT III SENSOR, User's Guide, Space Dynamics Laboratory, Utah State University.
3. Burdick, S., G. Chen and D. Morris. 1997 '*SPIRIT III Calibration Stars: Inband Irradiance and Uncertainty*', In the Proceedings of the Seventh SDL/USU Symposium on Infrared Radiometric Sensor Calibration, Space Dynamics Lab. , Utah State University.

The SPIRIT III telescope aboard MSX observed in the five following infrared wavebands<sup>2</sup>.

Band	Bandwidth	Isophotal Wavelengths ( $\mu\text{m}$ )
A	6.03-10.91	8.28
B <sub>1</sub> , B <sub>2</sub>	4.22-4.36, 4.24-4.46	4.29, 4.35
C	11.1-13.24	12.13
D	13.5-15.9	14.65
E	18.3-25.0	21.41

Of the above listed wavebands, the thermal emission from the zodiacal dust in near-IR bands B<sub>1</sub> and B<sub>2</sub> is very weak. Hence, we have restricted our analyses of the zodiacal emission to bands A, C, D and E.

### **Observations near the Sun**

The near-sun observations of the zodiacal cloud consist of five scans, each extending from the north ecliptic pole to the south ecliptic pole and include observations at elongations as small as 25° from the sun. The Earth was used as an occulting disk to block the thermal loading of the cryogenic sensor by the sun. The following table provides the observational parameters for each scan. All the scans maintain nearly constant ecliptic longitude resulting in the variation of elongation with ecliptic latitude.

Scan No.	Ecliptic Longitude of Observation	Ecliptic Longitude of Sun	Range of Solar Elongation	Range of Ecliptic latitudes
1	93.3°	118.4°	25°-90°	-90° to 90°
2	108.4°	134.4°	26°-90°	-90° to 90°
3	108.3°	136.7°	27°-90°	-90° to 90°
4	110.3°	138.2°	28°-90°	-90° to 90°
5	109.0°	134.4°	29°-90°	-90° to 90°

We have performed the preliminary analysis of one of these scans (Scan 2). The variation of solar elongation along the scan is shown in Figure 1.

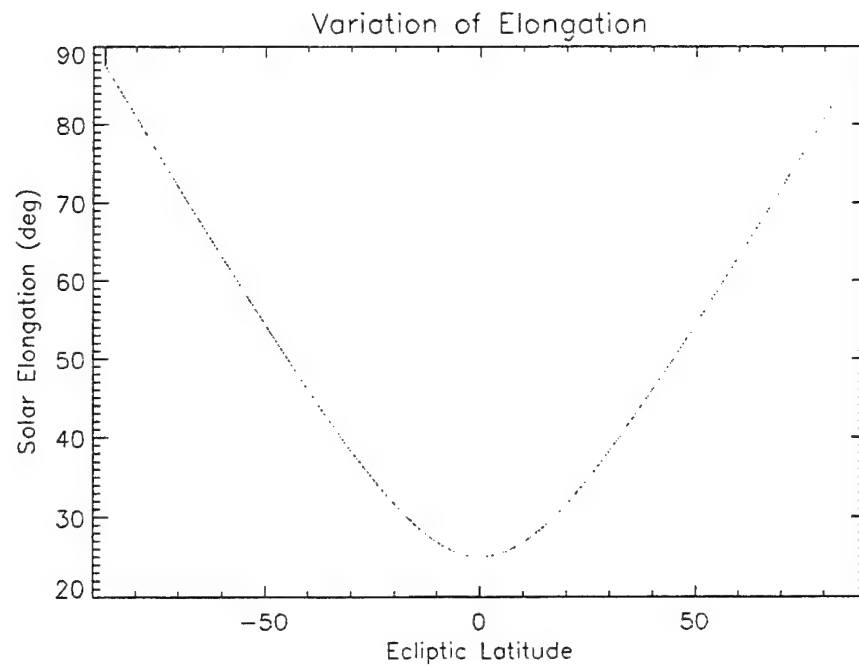


**FIGURE 1: Variation of the solar elongation along the ecliptic pole-to-pole scan.**

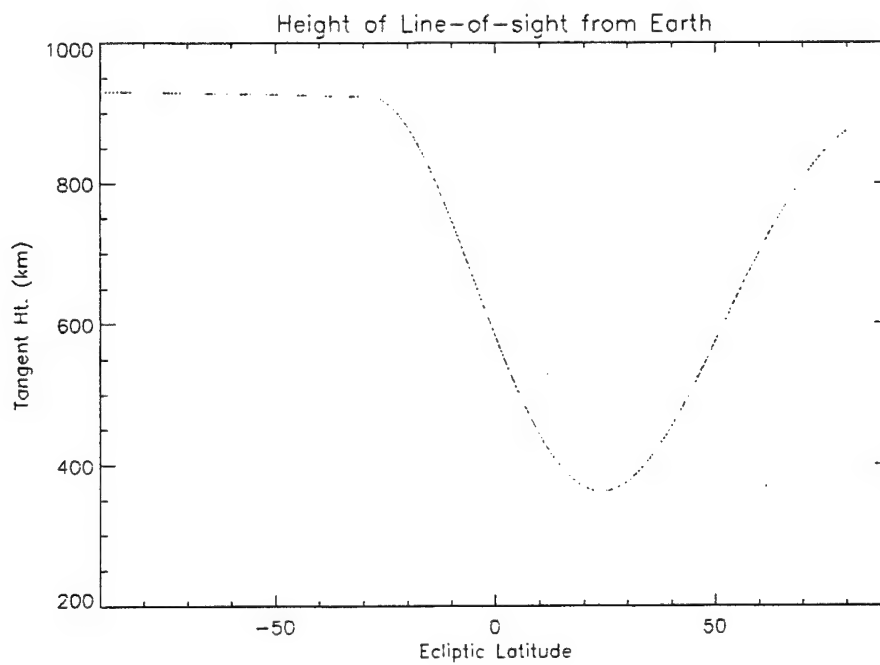


**FIGURE 2: Variation of the Tangent Height, from the Earth, of the line-of-sight with ecliptic latitude.**



The data analyses involved the following steps:

- (a) Each scan was initially represented as a set of FITS images  $\approx 4^\circ \times 1^\circ$  in the in-scan and cross-scan direction respectively with  $9''$  pixels. Thus, each scan was made up of  $\approx 45$  image arrays. The images were co-added to yield a resolution of 1 arcminute in the in-scan direction (ecliptic latitude) and  $\approx 1.0^\circ$  in the cross-scan direction (ecliptic longitude), thereby reducing the two dimensional arrays to a linear scan in latitude. The resulting scans are shown in Figure 3 (a,c,d and e) for each band. The plane of the Galaxy is at an ecliptic latitude of  $-30.5^\circ$  looking away from Galactic center (Galactic longitude of  $222.1^\circ$ ).
- (b) The expected location of the peak of the zodiacal signal is near the ecliptic while the observations show a very strong signal  $\approx 25^\circ$  above the ecliptic plane. The discrepancy is caused by the non-rejected Earth radiance (NRER) which is a consequence of using the Earth as an occulting disk during the observation. NRER is the radiation from the Earth when the line of sight of the spacecraft passes very close to the Earth's surface and varies with the tangent height of the line-of-sight from the Earth's surface. Figure 2 shows that the line of sight passes as close as 360 km from the Earth's surface leading to a dominant component of Earth radiation in the observations. We arrange the geometry of the scan to clearly separate the maxima from the NRER and the ecliptic plane crossing. From Figure 2 we deduce that the NRER contamination is maximum at an ecliptic latitude of  $25^\circ$  and decreases steeply with decreasing latitude.
- (c) We assume that, to a first order, the zodiacal cloud is symmetric about a plane close to the ecliptic. As the NRER contamination south of the ecliptic is negligible, we use the left half of the scan to estimate the right half. The residual flux is dominated by the NRER component shown by a dashed curve in Figures 3 (a, c, d, e). At the latitude of maximum zodiacal emission, the fraction of the signal attributed to NRER range from 6.5% in band A to 18% in band E, thereby confirming the assumption that the left half of the scan (below the ecliptic) is dominated by the zodiacal emission. The zodiacal scans are plotted in Figure 4 (a, c, d and e) and the location of the peak is obtained after iterating the point of symmetry such that the initial point of symmetry is equal to the latitude after subtracting the NRER component.

### **Peak Zodiacal Emission at solar elongation of 26°**

Waveband	Peak in-band Radiance ( $10^{-9}$ W/cm <sup>2</sup> /Sr)	Error (%) <sup>3</sup>	Latitude of Peak Radiance
A	3.35	8.5	-1.1°
C	1.28	11.5	-0.8°
D	1.12	15.8	-1.1°
E	1.19	36.5	-0.6°

### **Future Work**

In addition to the above near-Earth scans, MSX also observed the zodiacal cloud at ecliptic longitudes of 159-162° or 340-343°. There are a total of 65 such scans divided into short (-65° to 65° in ecliptic latitude) or long (-65° to 90° ecliptic latitude) scans which range in solar elongation from 60° to nearly 180°.

The analysis of the four remaining near-Earth scans as well as the 65 scans at larger elongations is in progress in tandem with the final calibration of the MSX data. As part of the calibration experiments, specific observations were taken to characterize the variation of the NRER with tangent height. These observations will be compared to existing models<sup>1</sup> and NRER component will be determined independently. We aim to calculate the flux densities of the zodiacal emission in MJy/Sr for solar elongations ranging from 25° to  $\approx 180^\circ$ . The observational results will be used to constrain the radial dust distribution in the models of the zodiacal cloud.

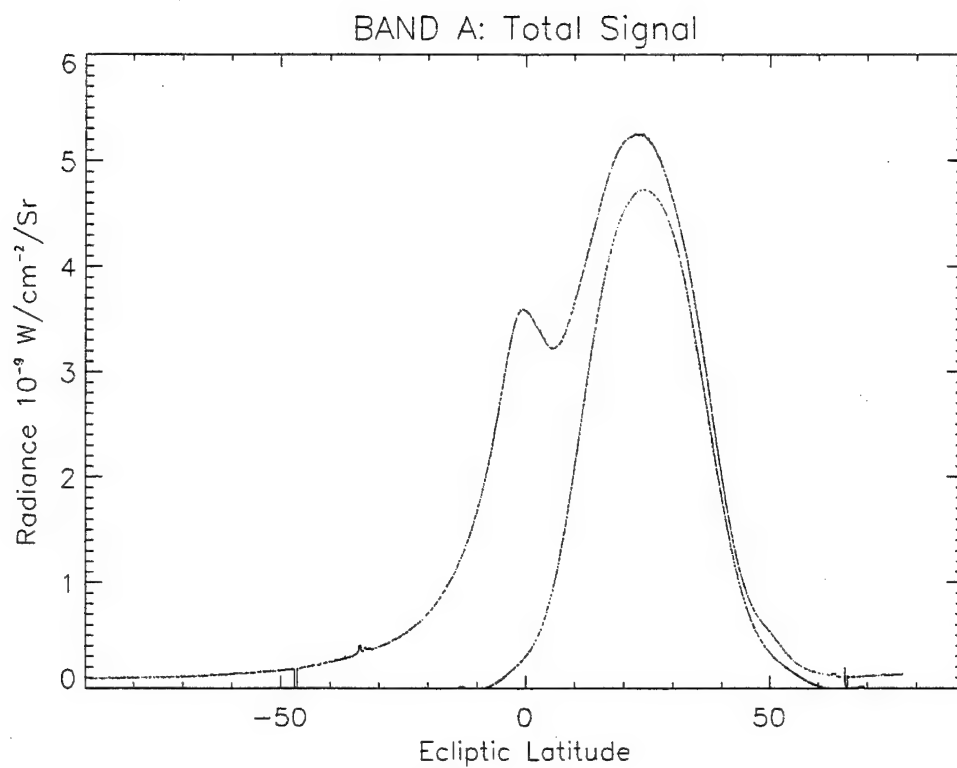


**FIGURE 3 a**

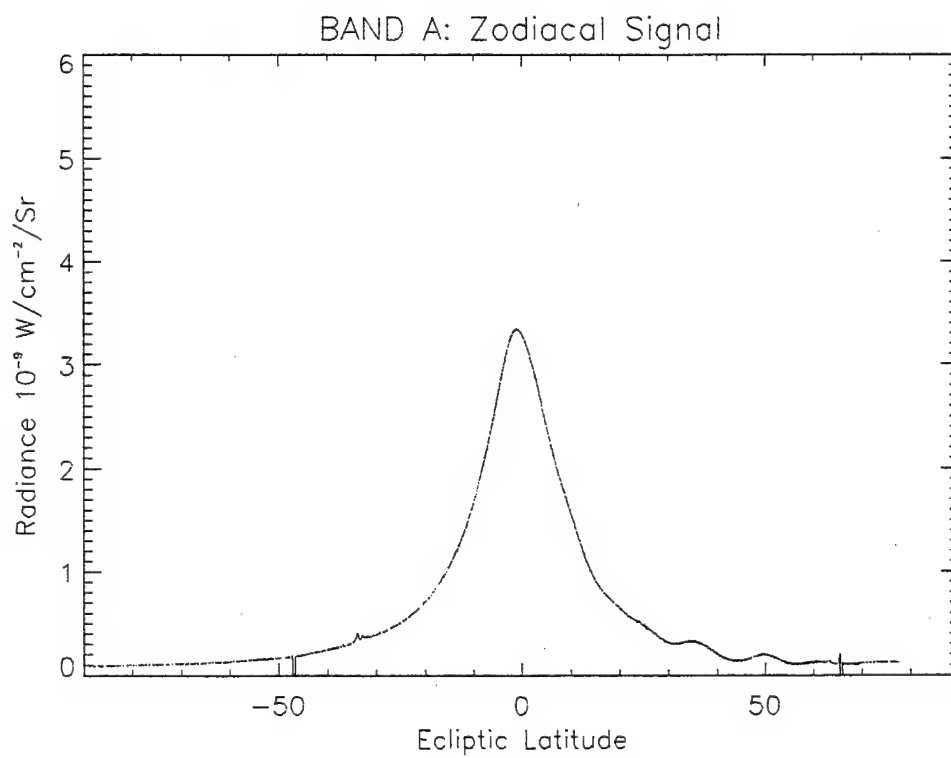


**FIGURE 4a**

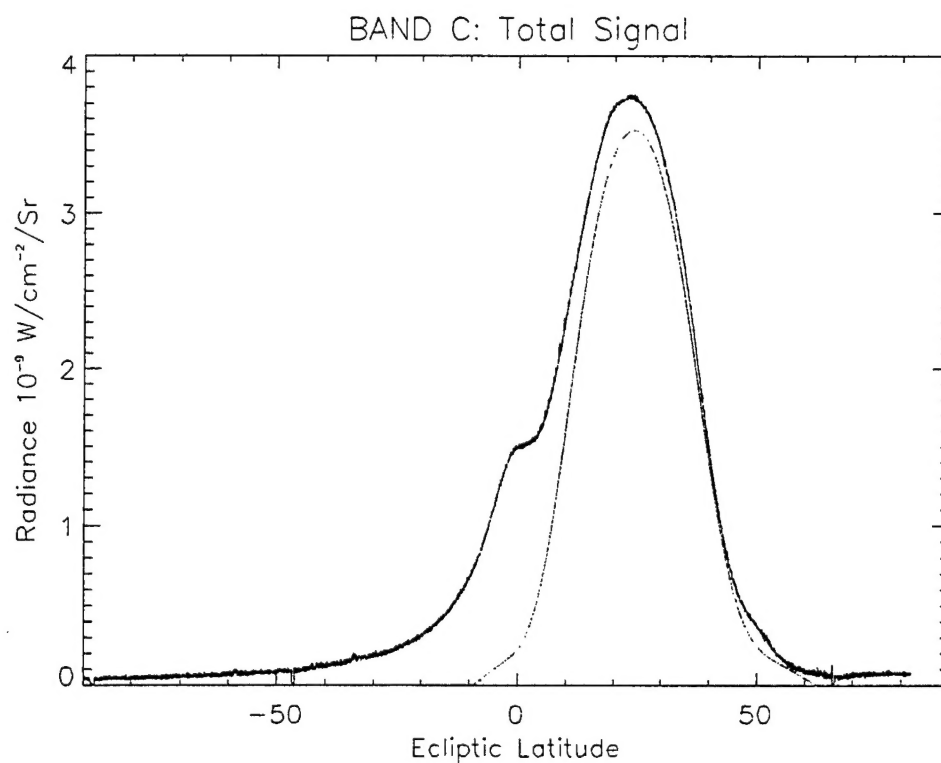


**Figure 3 c**

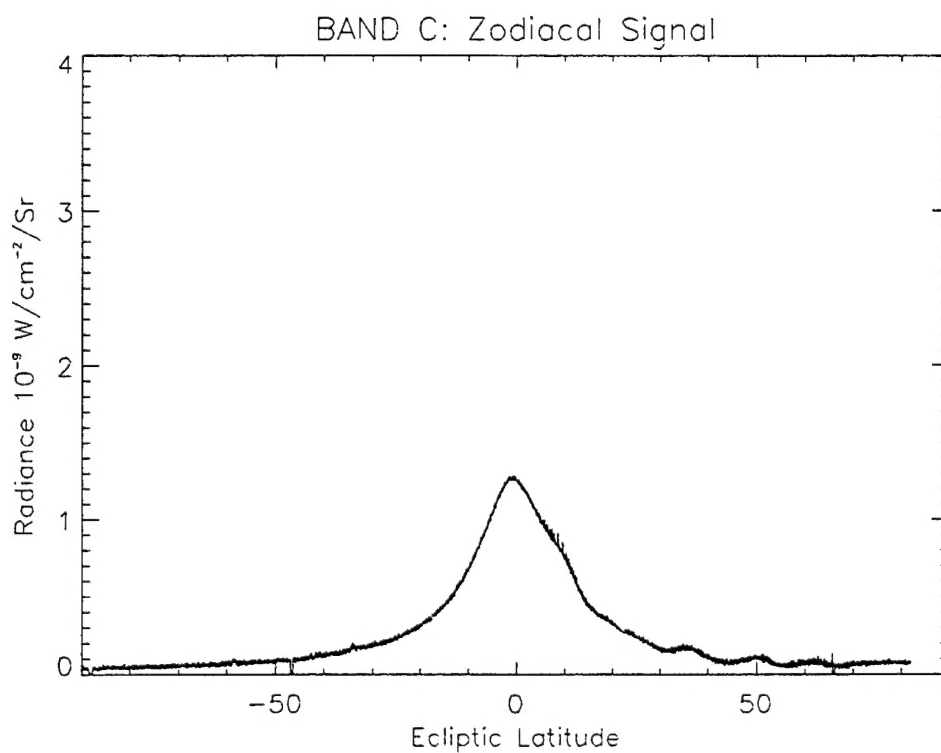


**Figure 4 c**

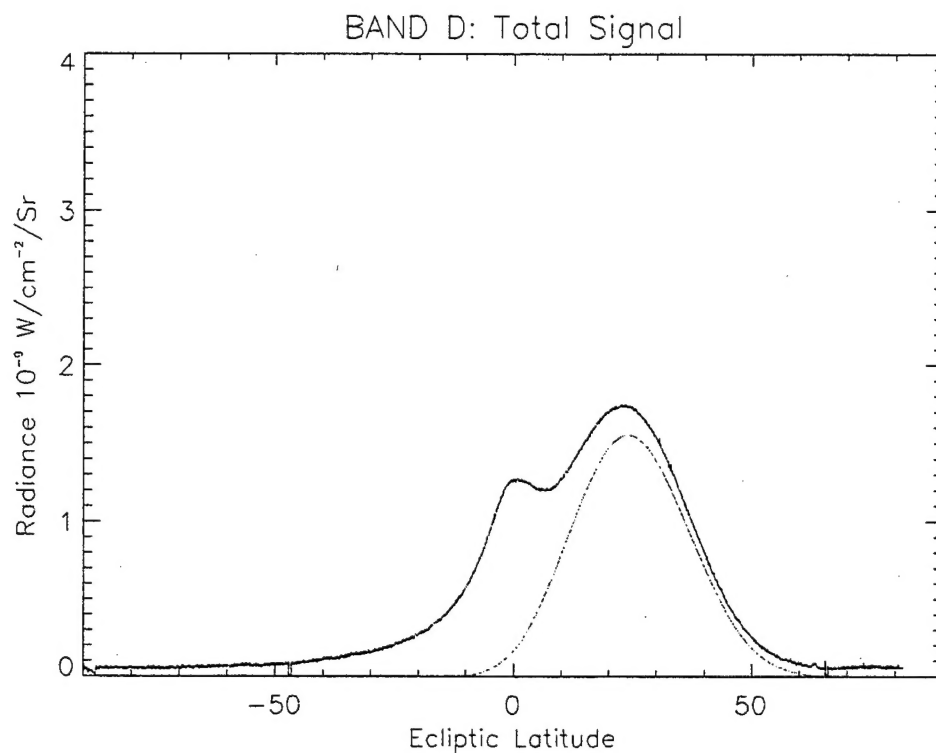


FIGURE 3 d

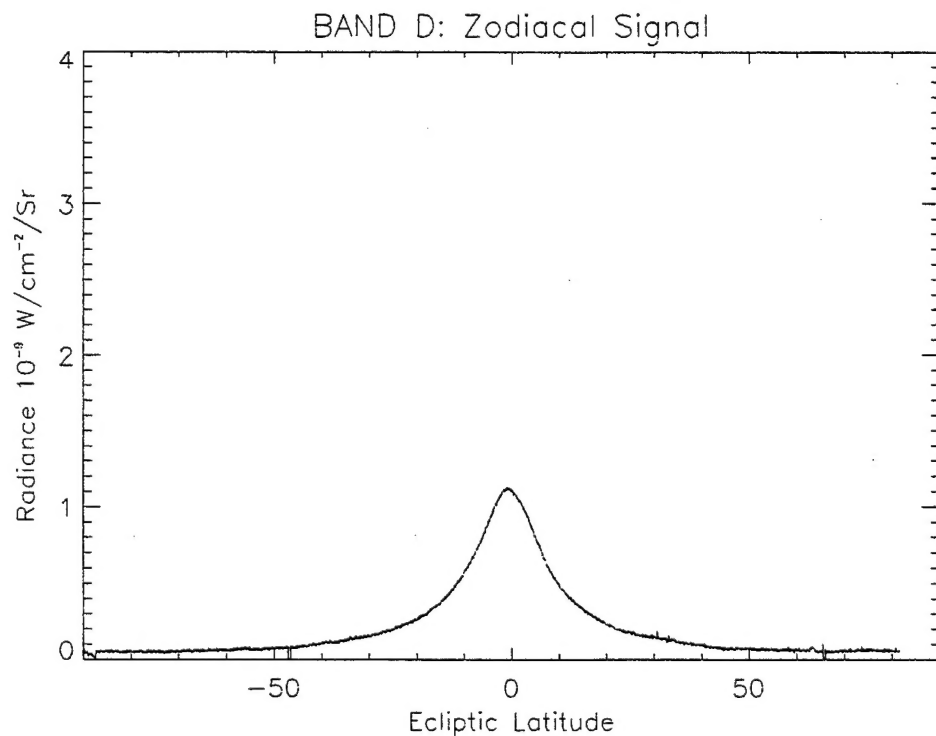


FIGURE 4 d

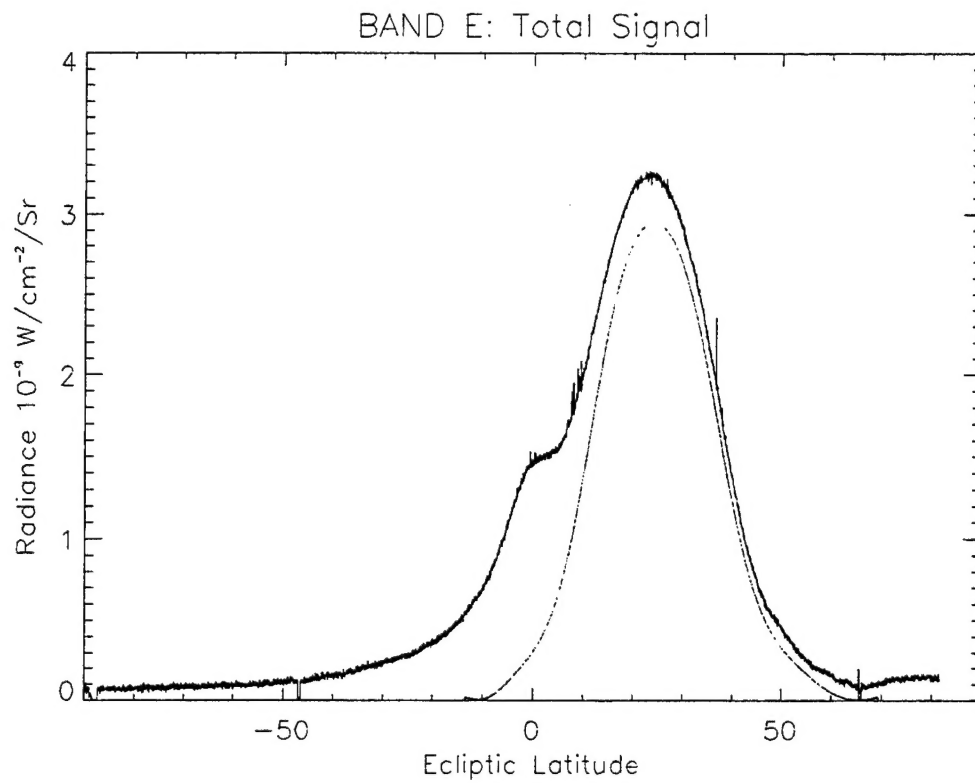


FIGURE 3 e

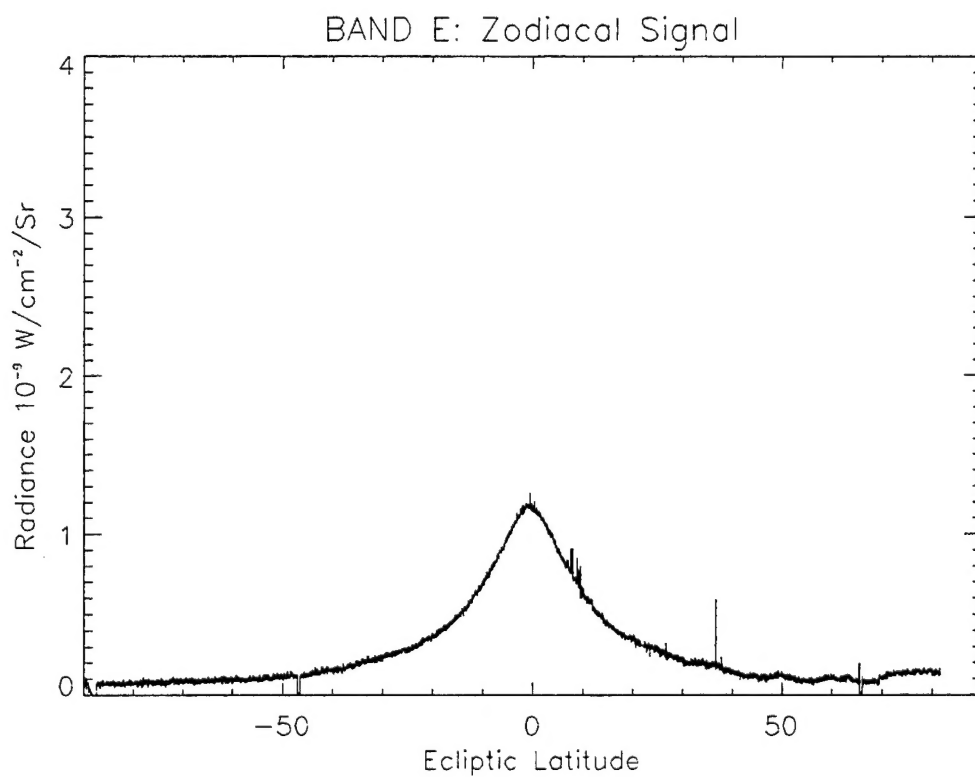


FIGURE 4 e



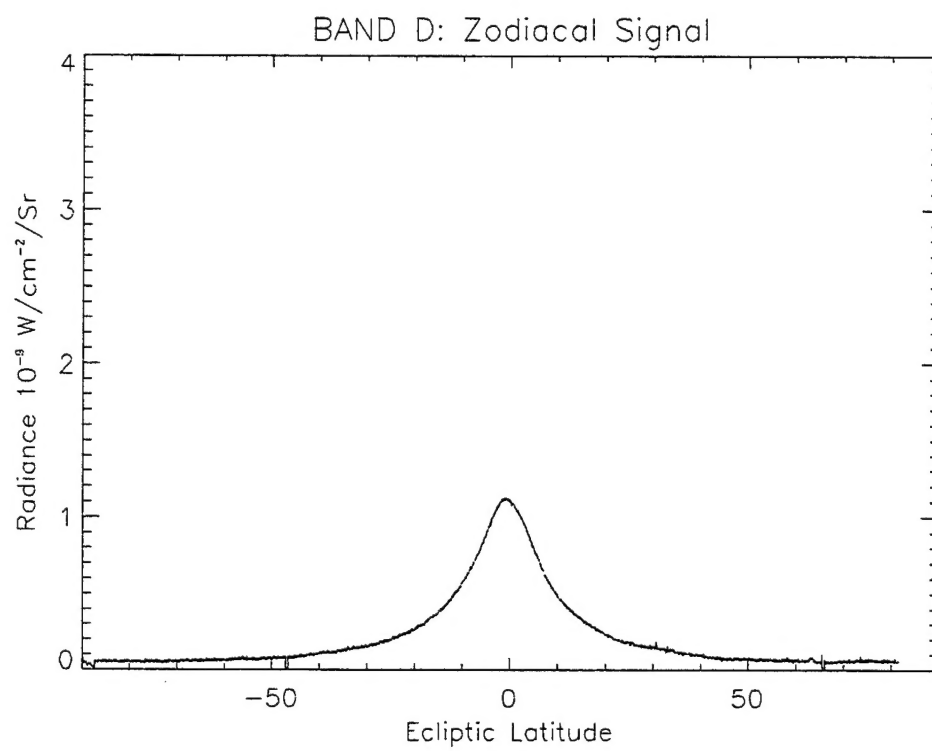


FIGURE 4d